

THE FLYING CARPET AND OTHER TALES

NOAH THOMAS JAFFERIS

A DISSERTATION

PRESENTED TO THE FACULTY

OF PRINCETON UNIVERSITY

IN CANDIDACY FOR THE DEGREE

OF DOCTOR OF PHILOSOPHY

RECOMMENDED FOR ACCEPTANCE

BY THE DEPARTMENT OF

ELECTRICAL ENGINEERING

ADVISER: JAMES C. STURM

NOVEMBER 2012

© Copyright by Noah Thomas Jafferis, 2012.
All rights reserved.

Abstract

In this work we use integrated piezoelectric actuators and sensors to demonstrate the propulsive force produced by controllable transverse traveling mechanical waves in a thin plastic sheet suspended in air above a flat surface, thus confirming the physical basis for a “flying” carpet near a horizontal surface. We discuss the fundamental and experimental conditions for realizing such a demonstration. The theory motivating our work is presented, and used to determine the range of experimental conditions most likely to produce a forward propulsive force. We then present a detailed description of the experimental approach to produce the traveling waves and demonstrate propulsion, including integrated piezoelectric actuators and sensors to provide feedback control, artifact elimination, and power considerations. Experiments are conducted to determine the dependence of the propulsive force on the height above the ground and the amplitude of the traveling wave, which qualitatively confirm previous theoretical predictions.

Theory also predicts that such forces should be able to accelerate a freely moving sheet up to a velocity of ~ 20 cm/s, sufficient for it to produce its own lift, resulting in the so-called “flying carpet” effect [3]. Currently, the sheet is not free, so the observed velocity is ~ 1 cm/s. To achieve this, work is ongoing to free the sheet from its tethers by providing on-board power using a boost-converter circuit, or by having a cart that carries the tethering wires and follows the sheet. In addition, to enable the sheet to begin moving without external lift, methods to reduce friction and static electricity are presented. Experiments with passive test samples show indications of lift beginning at ~ 20 -30 cm/s.

Two aspects related to the integration of improved functionality on the sheet are also presented. The first is preliminary work on printing silicon nanoparticles, as a means for

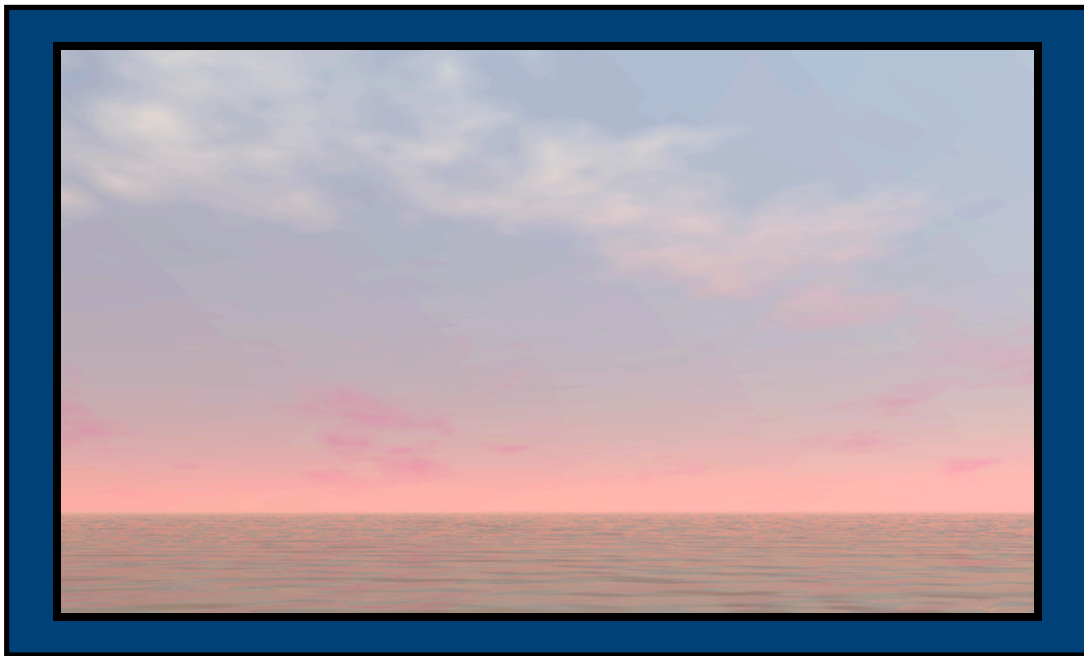
room-temperature circuit fabrication. This might be useful for integrating circuits on the piezoelectric film (PVDF) that we use for the “flying carpet”, since this material can’t be heated above 60° C. Second, we present the transfer of PZT nanoribbons to rubber as a route to more efficient piezoelectric materials.

Acknowledgements

I would like to thank everyone who has helped me, in numerous ways, both intellectually, and through moral support, towards the completion of this thesis. Thanks to my advisor Prof. Jim Sturm for providing an environment where I could pursue interesting and unusual projects, and for bringing his own ideas to the table when I was stuck. And for his belief in me even when I had doubts. Thanks to Prof. Howard Stone for many useful and enlightening discussions on fluid dynamics. I would also like to thank Prof. Michael McAlpine, Dr. Yi Qi, and Dr. Jihoon Kim for an engaging collaboration on energy harvesting. Thanks to Prof. Steven Lyon and Prof. Naveen Verma for taking the time to read this thesis and provide valuable comments and suggestions, and to Prof. Howard Stone and Dr. Nan Yao for serving on my FPO committee. We acknowledge the usage of PRISM Imaging and Analysis Center, which is supported in part by the NSF MRSEC program through the Princeton Center for Complex Materials (grant DMR-0819860). I would also like to thank Dr. Nan Yao for his help in the microscopy labs, in particular for the TEM images of silicon nanoparticles. Thanks to all of my friends and colleagues at Princeton for fun times, both in the lab and out, including hikes & swims, Formal Thursdays filled with hilarity, dinners & ice creams, and other outings: Jessica Hawthorne, Daniel Schwartz-Narbonne, Justin Brown, Natalie Kostinski, Clinton Smith, Ana&CJ BellPopper, Samuel Taylor, Jane Leisure, Seth Dorfman, David Lennington, Mariana Socal, Rodolfo Zertuche, Divjyot Sethi, Kevin Louterback, June Yeung, Elisabeth Lausecker, Yana Vaynzof, Linda Hung, Wenzhe Cao, Joseph D'Silva, Ting Liu, Yifei Huang, Bahman Hekmatsoar, Kunigunde

Cherenack, Keith Chung, Sushobhan Avasthi, Bhadrinarayana Visweswaran, Josue Sanz-Robinson, Warren Rieutort-Louis, and many others too numerous to name.

Finally, thanks to my brother, Daniel Jafferis, and mother, Dorene Jafferis, for their unwavering love, support, and encouragement, throughout my life, from the wonderful home-schooling years to the present and beyond. And a heartfelt thanks to my father, Jim Jafferis, who passed away in July 2009 – he missed most of my successful results, but he never wavered in his belief that I would work things out in the end. I would like to include the following picture, which was one of the last things we worked on together, in his memory:



To new horizons...

Table of Contents

Abstract	iii
Acknowledgements	v
Table of Contents	vii
List of Figures	x
1 Introduction	1
1.1 Background/Prior Work	1
1.2 Thesis Outline	5
2 Fundamental Mechanisms and Modeling	8
2.1 Physical Interpretation	8
2.2 Regimes of Applicability	15
3 Experimental Arrangement	20
3.1 Choosing Materials and Device Structure	20
3.2 Actuator Operation	24
3.3 Sensor Operation	27
3.4 Means of Suspension	31
3.4.1 Elastic Threads.....	31
3.4.2 Air Table.....	33
3.5 Overall Setup	34
4 Control of Traveling Wave Shape	37
4.1 Need for Sensors	37
4.2 Choice of Control Algorithm	40
4.3 Linear Control	41
4.4 Feedback Control	43
4.5 Camera Verification	44

5 Propulsion	47
5.1 Measuring the Propulsive Force	47
5.2 Results	49
5.3 Force Required for Lift	53
6 Power Considerations	55
6.1 Theoretical Power Losses	55
6.2 Measured Power Consumption	57
6.3 On-board Power	59
6.3.1 DC Amplification Simulations	60
6.3.2 AC Amplification Simulations	61
6.3.3 Experimental Circuit Implementation	63
6.3.4 IR-LED Control Signals	66
7 Practical Considerations and Experiments for Realizing Lift	68
7.1 Friction & Static Electricity	69
7.1.1 Reducing Friction	69
7.1.2 Effects of Static Electricity and Pressure-Dependence	69
7.1.3 Vibration-Induced Friction Reduction and Uphill Propulsion	73
7.1.4 Methods to Reduce Static Electricity	77
7.1.5 Methods to Address Pressure-Dependence	79
7.2 Lift Testing	80
7.3 Power on Cart	84
8 Printing of Silicon	86
8.1 Abstract	86
8.2 Introduction	87
8.2.1 Background/Prior Work	87
8.2.2 This Work	88
8.3 Experimental Methods & Results	88
8.3.1 Choice of Silicon-Nanoparticle Production Method	88

8.3.2	Porous Silicon	89
8.3.3	Silicon Nanoparticles	93
8.3.4	Silicon Thin-films	95
8.4	Summary & Future directions	102
8.4.1	Summary	102
8.4.2	Future Work	102
9	PZT Nano-Thick Ribbons / Energy Harvesting	104
9.1	Abstract	104
9.2	Introduction	105
9.2.1	Benefits for Actuation	105
9.2.2	This Work	106
9.3	Experimental Arrangement & Results	107
9.4	Summary & Future Directions	110
10	Summary & Future Directions for the “Flying Carpet”	114
10.1	Summary	114
10.2	Lift	115
10.3	2-D Propulsion	116
10.4	Overcoming Near-Ground Limitations	117
Appendix A	Publications and Presentations Resulting from this Thesis	119
A.1	Peer-reviewed Publications	119
A.2	Conference Presentations	119
Bibliography		121

List of Figures

1.1	Skate for motivation	3
1.2	Photo of actual sheet	6
2.1	Traveling-wave propulsion	9
2.2	Airflow balance schematic	12
2.3	Steady-state balance plot	14
2.4	Regimes of applicability plot	16
2.5	Illustration of two parameter restrictions	17
3.1	Comparison of bimorph and unimorph	22
3.2	Adhesive laminator	23
3.3	Device layout	24
3.4	Cross-section of actuator, sensor & multi-actuator arrangement	26
3.5	High-voltage amplifier	27
3.6	Measuring circuit	29
3.7	Artifact elimination	30
3.8	Thread suspension and air-table suspension diagrams	32
3.9	Elastic thread characterization	33
3.10	System block diagram	35
3.11	Box to protect sample	36
4.1	Low frequency	38
4.2	High frequency	39
4.3	Result of linear control	42
4.4	Feedback block diagram	43
4.5	Result of feedback	45
4.6	Camera measurement	46

5.1	Pendulum force & force vs. displacement for air table	48
5.2	Propulsion data on regimes of applicability plot	49
5.3	Propulsion versus amplitude	50
5.4	Propulsion versus height	51
5.5	Air-table propulsion versus amplitude & height	52
5.6	Image sequence of sheet moving	53
6.1	Power consumption	58
6.2	Simulation of basic boost converter	61
6.3	Simulation of boost converter with feedback	62
6.4	Boost converter circuit & oscilloscope plot	64
6.5	IR-LED detection circuit & oscilloscope plot	67
7.1	Cross-section of sheet on tiny supports	70
7.2	Friction with sheet off	71
7.3	Illustration of sliding angle	74
7.4	Uphill Propulsion and Vibration-induced friction reduction	76
7.5	Test sample lift	82
7.6	Photo of cart & sheet detection schematic	85
8.1	Etching setup & reaction	90
8.2	Lowering mechanism & Multi-wafer etching	91
8.3	Luminescence	92
8.4	Nanoparticle crystallinity & size distribution	94
8.5	Film continuity	96
8.6	Roughness	97
8.7	Presence of pores	98
8.8	Effect of compression	99
8.9	Composition	100
8.10	Demonstration of chemical/physical stability	101
8.11	TFT test structure.....	103

9.1	Actuation benefit (PZT versus PVDF)	106
9.2	Interdigitated structure	107
9.3	d31 measurement setup	108
9.4	d31 results	109
9.5	Actuation for unimorph versus interdigitated structure	111
9.6	Diagram of process for improved actuation	113
10.1	2-D propulsion illustration	117
10.2	Propulsion away from the ground.....	118

Chapter 1

Introduction

1.1 Background/Prior Work

In recent years, the development of thin-film electronics on substrates other than silicon has driven a progression from rigid substrates to flexible, and even stretchable substrates. Such substrates find applications in areas such as rollable displays, electronic skin [37], and brain sensors [19]. To date, the shapes of these substrates have been primarily passive, with any deformation produced by external means. However, it is desirable to move to substrates with truly active shape control, as the next step beyond bendable/stretchable substrates. Such substrate deformation is typically achieved by applying voltages across a piezoelectric element, dielectric elastomer [27], or muscular thin film [12]. For accurate control of the shape, the ability to monitor the shape in real time with integrated deformation sensors is desirable. This is especially true for rapidly changing shapes, due to the effects of mechanical resonances and non-linearities. There are many potential applications for such local deformation control, such as solar cells that bend to follow the sun, speaker arrays, adaptive optics, mechanical grippers [40], and self-propelled devices (see further discussion below). The last item will be the subject of this thesis, and the techniques used to produce traveling waves, as discussed in this work, provide high-speed local control of the shape of a thin substrate, which could also be

particularly useful for adaptive optics for telescope mirrors. Such systems currently use arrays of separate actuators, with a flexible, but passive, reflective sheet over the actuator array [45]. In addition, these systems typically do not have built-in sensors for shape detection and feedback, but rather rely on external means, such as shining light on the mirror surface, to determine the actual time-varying shape for a given set of voltage signals applied to the actuators. Hence, the ability to use a single sheet for the actuator array, reflective surface, and sensor array, would be of great interest.

In this work [16], we present a device that experimentally confirms the theoretical prediction that a thin sheet vibrated in a traveling wave shape will produce a force in the direction opposite that of the wave propagation [38], [30]. The resulting forward motion of the sheet near the ground has also been predicted to produce a lift force [39], leading to a so-called “flying” carpet [3]. This device demonstrated a form of propulsion that operates without separate moving parts, since all actuation elements are formed from the same thin sheet of material. Potential advantages of this include low manufacturing costs and long lifetime. In addition, sensor arrays, for example chemical or biological, could be integrated onto the sheet. Some biological organisms, such as skates (Figure 1.1), use traveling wave-like deformations for propulsion in water [38], [30]; hence this device could be used to model biological organisms, for example, for fluid dynamics studies. The device is easily scalable to different sizes, provided that the operation remains in a regime of low Reynolds number.

Much research has been undertaken on mechanisms for small-scale (micro to mm) propulsion, which typically takes place at relatively low Reynolds number (less than a few thousand), in three general regimes – “swimming”, “crawling”, and “flying”. For

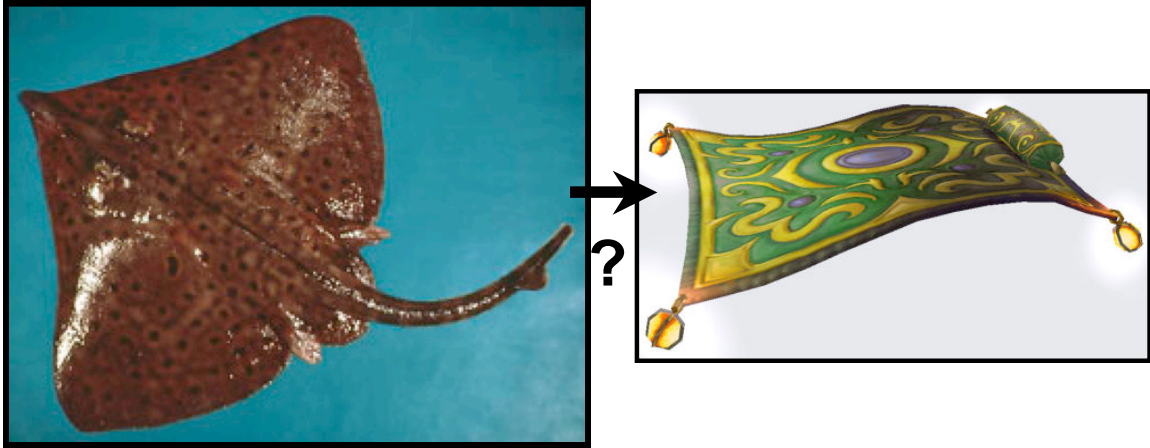


Figure 1.1 Photo of a skate – motivates development of a “flying carpet”. Manta rays and skates propel themselves under water by undulating motions similar to traveling waves.

“swimming”, examples include using magnetic fields to oscillate microscopic filaments of magnetic particles in a water-based salt solution [10] (resulting in swimming velocities of $\sim 10 \mu\text{m/s}$), affixing bacteria flagella to $10 \mu\text{m}$ polystyrene beads [4] (swims at $\sim 15 \mu\text{m/s}$), and even approaches aimed at propulsion inside blood vessels, for example using a clinical MRI to guide a 1.5 mm magnetic bead (up to $\sim 10 \text{ cm/s}$) in a living swine artery [21] (see [22] for an overview). In another work [31], tiny rods $5\text{-}10 \text{ mm}$ long by $250 \mu\text{m}$ – 1.5 mm wide were propelled underwater by an oscillating air bubble (propulsive forces $\sim 2\text{-}20 \mu\text{N}$). On the cm-scale, propulsion has been induced by periodic contraction of a “muscular thin-film” in water [12], although the exact shape was not clear (velocities were still only $\sim 200 \mu\text{m/sec}$).

Another mechanism for small-scale propulsion is “crawling”, which is typically motivated by the motion of earthworms, such as using external magnetic fields to periodically contract and expand a string of magnetic-fluid-containing capsules in a 12 mm tube (speed $\sim 5 \text{ mm/s}$) [32], using shape-memory alloys to periodically contract and extend (longitudinally) a $\sim 1 \text{ cm} \times 5 \text{ cm}$ bellows with angled ‘legs’ to provide anisotropic

friction (speed $\sim 170 \mu\text{m/s}$) [18], and a folded origami robot with a similar method of propulsion ($\sim 300 \mu\text{m/s}$) [25].

Finally, small-scale propulsion in air has been an active area of research lately, from early work using an external magnetic field to rotate a $\sim 5 \text{ mm}$ magnetized propeller [23], to the development of $\sim 50\text{-}150 \text{ mg}$ flapping-wing microrobotic flies [42], [43], which use a single piezoelectric actuator to drive the wings ($\sim 3 \text{ cm}$ span) at around 100 Hz , resulting in lift forces of $\sim 1\text{-}3 \text{ mN}$, and a power consumption of $\sim 50 \text{ mW}$. The Reynolds numbers for these devices are $\sim 1000\text{-}3000$. For a more complete overview of miniature ($<1 \text{ cm}$ to $\sim 15 \text{ cm}$) flying devices, see Section 2.3 in [8]. These flying devices are split into three categories based on lift mechanism – fixed-wing, rotating-wing, and flapping-wing. Our work is related to the fixed-wing category because the lift is predicted to result from the forward motion of the device. However, the mechanism of propulsion is more closely related to that of flapping devices.

Works in small-scale propulsion can be further categorized into self-propelled (i.e. propulsion mechanism is part of the device) [4], [31], [12], [18], [25], [42], [43] and externally propelled (e.g. through use of external magnetic field) [10], [21], [32], [23] devices. Self-propelled devices can be more challenging due to their small size constraints, but are advantageous for reasons of autonomy and overall system-size reduction.

Our work, which is self-propelled, takes an approach that employs an internally generated transverse traveling wave deformation, which is more akin to methods for under-water propulsion than to typical approaches to flight, but designed to operate in air near a boundary. This enables it to operate at Reynolds numbers less than around 10,

despite its size of ~ 4 cm x 10 cm and moving in air at speeds up to 10 cm/s (in the current work, ~ 1 cm/s speeds have been achieved). Due to the much lower viscosity of air compared to water (~ 50 times), the propulsive force would be much smaller in air for the same wave parameters, as we will see in Chapter 2. However, by operating the device sufficiently close to a boundary, this can be overcome. In addition, the air boundary layer greatly reduces friction compared to “crawling”, allowing higher speeds for the same propulsive force (assuming that the propulsion mechanism is still a traveling wave).

1.2 Thesis Outline

Chapter 2 discusses the physical interpretation of traveling wave propulsion, including steady-state airflow balance and force balance. The fundamental and experimental conditions under which we expect to see traveling-wave induced propulsion in air are investigated to determine attractive regions in parameter space to begin experiments.

Chapter 3 discusses the details of the experimental arrangement, including choice of material and structure, actuator and sensor operation, removal of artifacts from the sensor signals, and means of suspension. A photo of the actual sheet is shown in Figure 1.2.

Chapter 4 describes the methods used to produce traveling-wave vibration in the sheet, from linear control to feedback.

Chapter 5 describes the experimental demonstration that a thin sheet, deformed in a traveling wave shape by integrated piezoelectric actuators, generates a propulsive force that propels the sheet forward in air. The propulsive forces expected to be necessary for lift are also discussed.

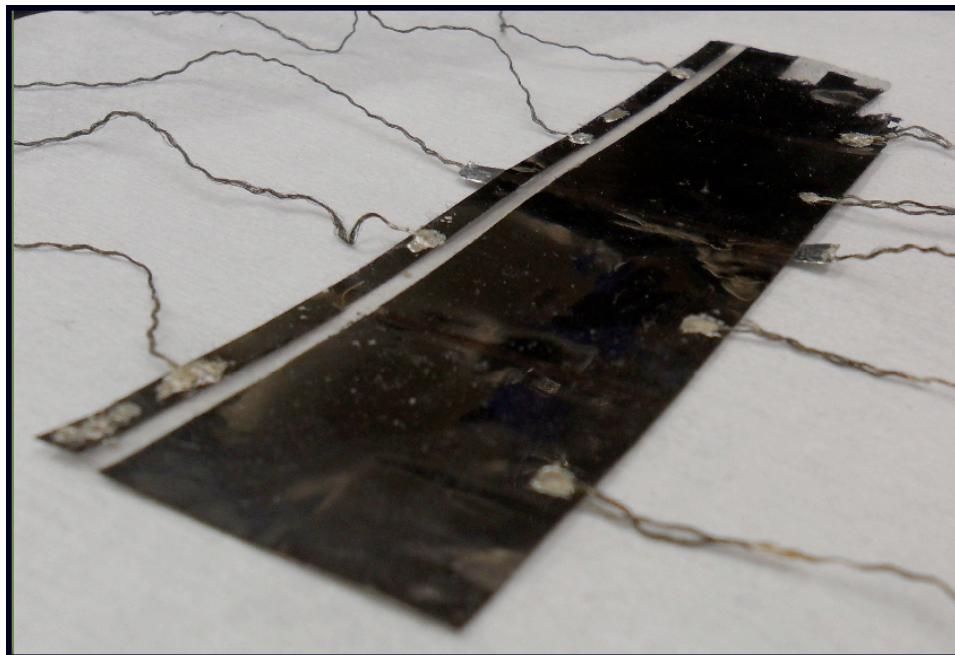


Figure 1.2 Photo of experimental realization of a “flying carpet”. The details are described in Chapter 3.

Chapter 6 discusses power considerations, from theoretical losses to the measured power consumption. Preliminary work on an on-board power supply is described.

Chapter 7 discusses lift, from the theoretical prediction to practical considerations such as friction and static electricity, as well as a demonstration of uphill propulsion. Using a cart to follow the sheet is presented as a method that allows the sheet to move faster (for the purposes of lift demonstration) without requiring on-board power.

Chapter 8 is preliminary work on room-temperature “printed” silicon, which would be useful for thin-film electronics on PVDF, due to the low temperature ($\sim 60^\circ\text{C}$) at which PVDF begins to lose its piezoelectric properties.

Chapter 9 is preliminary work in another future direction – lowering the power requirements, particularly the voltage, by developing PZT nanoribbons that can be transferred onto flexible substrates.

Chapter 10 summarizes our results and presents possible future directions – what needs to be done to demonstrate lift, 2-D propulsion, and overcoming near-ground limitations.

Chapter 2

Fundamental Mechanisms and Modeling

In this chapter we discuss underlying mechanisms for traveling-wave propulsion. Section 2.1 explains the physical interpretation, and in Section 2.2, we explore limitations that guide our choice of parameters.

2.1 Physical Interpretation

The basic mechanism of traveling wave-induced propulsion can be understood as follows [16]: Imagine that the sheet begins at a height h_0 above the ground, is stationary, and has no tilt. Then, when the sheet begins to bend in the shape of a traveling wave, a pocket of the encompassing fluid (air in our case) is pulled in from the front end, and carried along with the wave until it reaches the back end of the sheet, where it is released (Figure 2.1). Thus the traveling wave acts as a pump (such pumping has been demonstrated in glycerol and water [33]). Note that we consider only pumping between the sheet and the ground because there is no boundary above the top surface, which means that the air above the sheet is free to move perpendicularly away from the sheet as well. Since the wave acts to push fluid in the direction of the wave, there must be a corresponding force that the fluid exerts on the sheet in the direction opposite to the

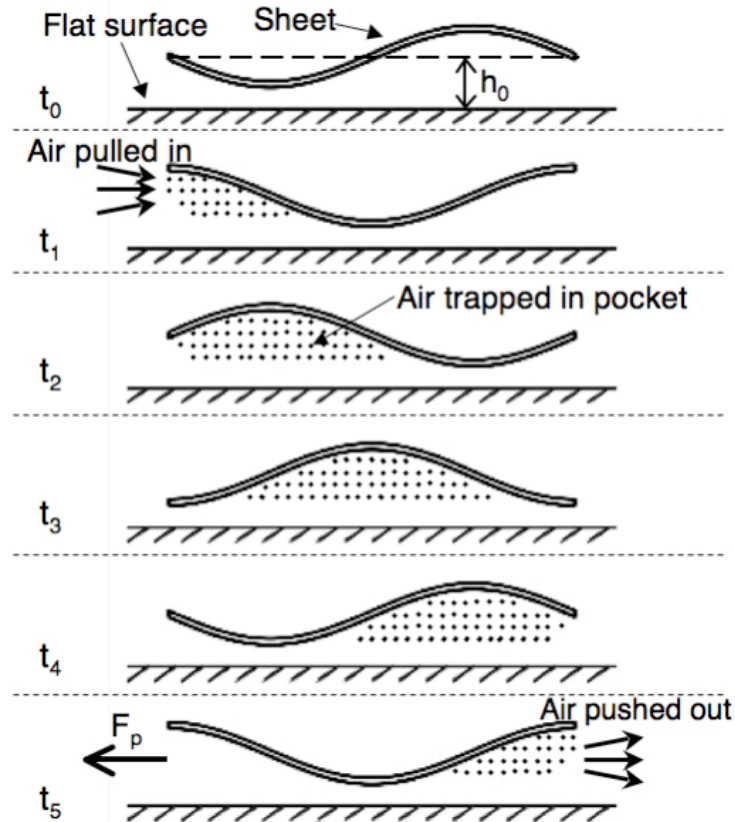


Figure 2.1 Schematic diagram of a traveling-wave pump, showing the shape of the sheet at a sequence of times (t_0 to t_5) over one and a half periods of oscillation. This time-varying shape pulls air in from the left, and pushes it out to the right, resulting in a propulsive force, F_p , to the left.

wave. This propulsive force is expected to increase as the gap between the sheet and the ground is decreased, due to reduced leakage on the side of the sheet that faces the ground.

Reference [3] was a numerical simulation that predicted the velocity of such a sheet, under certain external conditions (i.e. an ideal unconstrained sheet), and did not explicitly calculate the propulsive force. They also presented several equations that approximate the simulation results, relating the steady-state velocity and height above the ground to the sheet parameters – we use these expressions throughout the text. We desire to separate out the theoretical propulsive force because it is the intrinsic physical property of the

propulsion mechanism, and can therefore tell us how the system will behave if the external forces are changed (i.e. not just drag). Although the propulsion and the drag are both generated from the same piece of material (as opposed to a plane, for example, in which the propulsion is generated by an engine, and the drag by the wings and body), we can separate them by assuming that the drag on the sheet when bent in a fixed sine wave shape of small amplitude (both the amplitude, which is up to a few hundred microns, and the sheet's thickness of $\sim 100 \mu\text{m}$, are 100-1000 times smaller than the length of the sheet, so skin friction will dominate) is approximately equal to that of a flat sheet. Then, when the sheet's shape is changing in time, we still consider this to be the drag force, and the remaining force (in the horizontal direction) is defined to be the propulsive force. Note that we have extracted this propulsive force under the assumption that it will be unchanged by a change in the external environment (e.g. an additional restraining force). However, this would break down if the speed of the sheet were to approach the speed of the traveling wave. Since our experiments are all conducted far below this limit, we have ignored this effect in our analysis. In addition, time variations of velocity, lift height, and angle of attack are seen in the numerical simulations of [3], on the time-scale of the vibration period. However, for this work we consider much longer time-scales over which we can deal with time-averaged trends, since that is what we can most easily measure in our experiments.

To determine the theoretical propulsive force, we first note that for an ideal flat sheet (i.e. no thickness) moving freely close to a boundary, under low Reynolds number (Re) conditions, the drag force is given by: $F_{drag} = v\mu_{air}WL/h$, where v is the velocity of the sheet, W and L are its width and length, h is the height above the ground, and μ_{air} is the

air viscosity. The Reynolds number is given by $\rho_{air} v \ell / \mu_{air}$, where ρ_{air} is the density of the surrounding fluid (air in this case), v is the velocity of the sheet, μ_{air} is the viscosity of air, and ℓ is a characteristic length. The characteristic length is given by h (the height above the ground) in this scenario, provided that h is small when compared with W and L . For a sheet moving at 1 cm/s at 1 mm above the ground, this gives a Reynolds number of ~ 0.7 . For a sheet moving freely and in steady-state, the air flow per width W pushed backwards by the traveling wave ($\sim Af\lambda$) must equal the air flow per width W pushed forward by the sheet's forward motion ($\sim v h$): $Af\lambda \approx v h$ [3], where A , f , and λ are, respectively, the amplitude, frequency, and wavelength of the traveling wave (valid for $A < h$). This result follows since, when a sheet moves laterally close to a boundary, it pulls along approximately half the volume of air under it (Figure 2.2). The factor of 2 is ignored, as this analysis gives only an approximate expression. By comparing with the drag force F_{drag} , one finds that the theoretical propulsive force produced by the wave is:

$$F_p \approx \frac{Af\lambda\mu_{air}WL}{h^2}, \quad (1)$$

where A is the amplitude of the traveling wave, f is the frequency, λ is the wavelength, μ_{air} is the air viscosity, W is the width of the sheet, L is the length of the sheet, and h is the sheet's height above the ground.

From equation (1) above, our experimental challenge is to create a thin film traveling wave such that an observable force F_p results. However, in choosing the frequency f and amplitude A , there are several considerations and tradeoffs to be evaluated. First, we consider the physical interpretation of the sheet's 'free' operation by breaking it down into several steps A-D. In our experiments, the sheet is tethered (see Chapter 3 for more details) but the end goal motivating our choices is a freely moving sheet. The equations

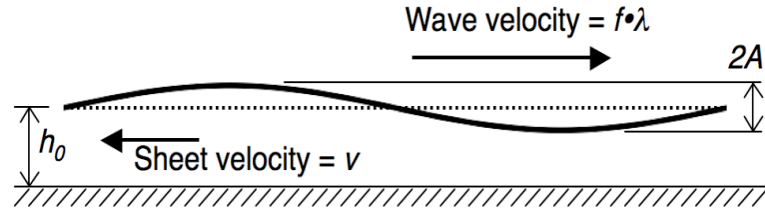


Figure 2.2 Airflow balance schematic. In steady-state, air pushed backwards by the wave ($\sim A f \lambda$) must balance air pushed forward by the sheet ($\sim v h_0$).

presented are derived from those in reference [3]; note that we want to maximize λ to increase the propulsive force, so we choose $\lambda = L$.

(A) A traveling wave in the sheet pushes air backwards, resulting in a propulsive force, F_p . Equation 1 is a reasonable approximation for this force provided that h is not too small (clearly, F_p can not actually diverge as h goes to zero, as suggested by (1)) or too big (h is replaced by W or L once it become comparable to them) and that the vertical inertia of the sheet (due to its vibration) can be ignored. In addition, the amplitude is always limited to be less than h .

(B) The sheet then accelerates laterally, and, as it does so, it encounters two velocity-dependent forces: drag ($F_{drag} = v \mu_{air} W L / h$) and lift ($F_{lift} = v \mu_{air} W L^2 / h^2$). The expression for lift is derived from Reference [3]. These expressions assume low Reynolds number flow near a boundary, and are thus valid for small v and h . In addition, the angle of attack of the sheet is assumed to be $\sim h/L$, an approximation which arises from the numerical simulations of [3]. Unlike a standard airplane, in which the wings are attached to the body at a fixed angle, in our device, the angle of attack results from a balance between the tendency for a flat sheet to rotate perpendicular to its direction of motion, and increasing viscous forces at the back end of the sheet (due to its proximity to the ground) which prevent it from rotating further. To understand why the tilt arises, in more

detail, consider the situation from the reference frame of the sheet, and suppose that the sheet begins with a slight tilt (higher on the end facing the air flow). As the air begins to enter the region under the sheet, it is deflected downward by the angle of the sheet. This means that the sheet has exerted a downward force on the air, and hence, the air exerts an upward force on the leading end of the sheet. Similarly, as the air exits the back end of the sheet, it is deflected upward (i.e. back to horizontal); hence there is a downward force on the back end of the sheet. In addition, due to the viscous forces under the sheet, the velocity of the air versus distance from the sheet varies from zero at the sheet to v at the ground (recall that we are speaking in the reference frame of the sheet). Viscous forces above the sheet are much smaller, because the sheet is not near a boundary on that side. While the sheet is still close to level, this variation of air speed with height is approximately linear and the same over the length of the sheet. However, as the back end is pulled closer to the ground, the viscous forces, which are proportional to dv_{air}/dy (where y is measured vertically away from the sheet), become considerably greater at the back end than at the front, due to both the decrease in the gap size, and the increase in the average air velocity resulting from the initial pressure gradient. Thus, the pressure begins to increase at the back end, counteracting the initially tendency pulling the back end down, resulting in a steady-state tilt, and the corresponding lift, as given above.

(C) As the sheet's lateral speed increases, the lift force increases until, in theory, it is sufficient to overcome gravity, and the sheet begins to lift. The drag force increases as well, slowing the sheet's acceleration.

(D) Since h is now increasing, the lift force decreases, as does F_p (faster than F_{drag}). Eventually, steady-state is reached in which the lift force balances gravity (given by

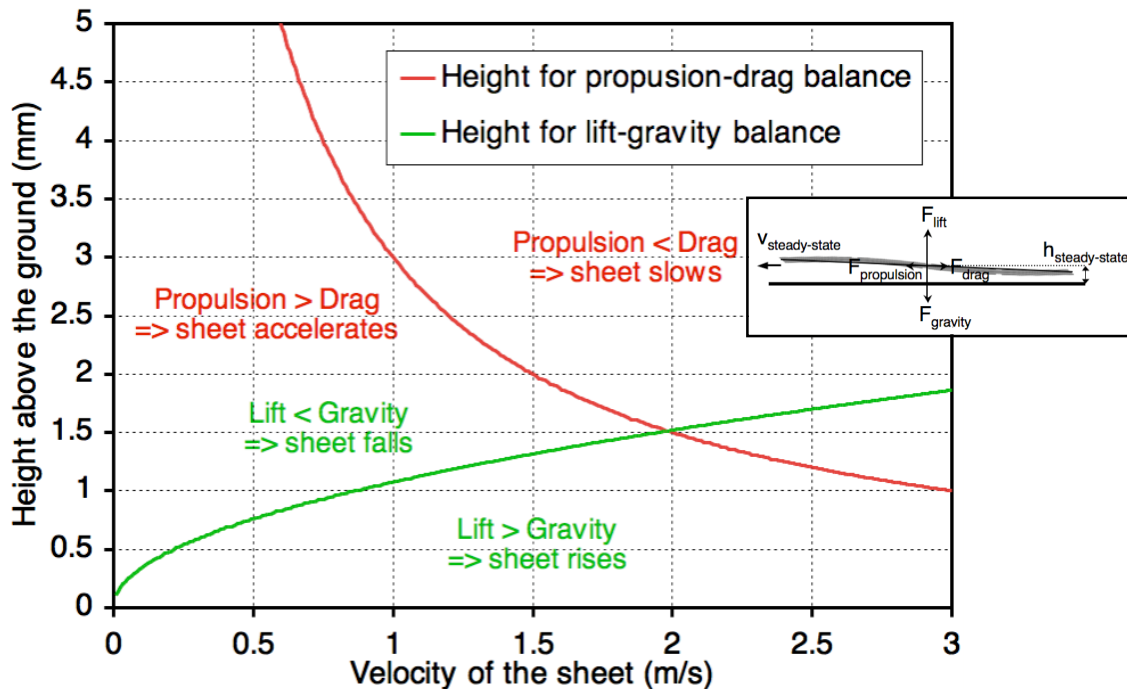


Figure 2.3 Steady-state balance plot. The plot for propulsion-drag balance is determined by setting $F_p = F_{drag}$, and the plot for lift-gravity balance is determined by setting $F_{lift} = mg$.

$\nu \mu_{air} W L^2 / h^2 = m g$, where m is the mass of the sheet and g is the acceleration due to gravity), and the propulsive force balances the drag ($A f \lambda \mu_{air} W L / h^2 = \nu \mu_{air} W L / h$) (Figure 2.3). Note that the steady-state velocity and height in Figure 2.3 (~ 2 m/s and 1.5 mm, respectively) would result in a Reynolds number of ~ 200 , and thus are not quite accurate. For example, we would expect the drag to be larger (at a given velocity) in this regime than for Re less than 1; hence if the propulsive force is unchanged we expect a lower steady-state velocity than that shown in Figure 2.3. At high Reynolds number, the drag will scale with the velocity squared, but the transition is typically gradual, and may not occur exactly at $Re = 1$. For example, for a flat sheet in mid-air the drag coefficient for the inertial forces term (i.e. $\propto v^2$) is quite small (typically less than $1/100$) because the reference area is parallel to the flow. For the case of a flat sheet near a boundary, this

inertial term essentially results from the average slowing of the air under the sheet, and is thus proportional to h , resulting in a drag coefficient of $\sim h/L$, which is $\sim 0.01-0.02$ for our experiments. Hence, we might expect to see a total drag force of $F_{drag} = 0.5 C_{drag} \rho_{air} W L v^2$, where $C_{drag} \sim (2/Re + b/Re^{0.5} + h/L)$ and b is a fitting parameter. Hence, for Re between about 1 and 100, the drag may not yet scale with velocity squared, but will likely begin to increase more gradually, depending on the value of b .

2.2 Regimes of Applicability

To identify promising experimental regimes in which to experimentally probe the phenomena (in air), we now look in detail at several physical regimes of operation (Figure 2.4), as a function of the amplitude A and frequency f of the traveling wave. Some of these are relevant only for a freely moving sheet, while others are applicable in general. The physical parameters of the sheet used in this plot were length $L = 10$ cm, thickness $D = 86$ μm , and density $\rho = 1.77$ g/cm^3 . Five conditions were used to restrict the regimes as shown in Figure 2.4:

{1} *Wave amplitude versus lift height*: In steady-state, the lift height is predicted [3] to be

$$h_{steady-state} \sim (A f)^{1/3} \cdot (\mu_{air} L^2 / \Delta\rho g D)^{1/3} \quad (2)$$

(where $\Delta\rho$ is the difference in density between the sheet and the air, g is the acceleration due to gravity, and D is the thickness of the sheet) When the traveling wave amplitude is greater than the predicted steady-state lift height, the sheet would intersect the ground on part of its oscillation, which is not a physical situation (Figure 2.5a). This occurs when $A > h_{steady-state}$, which from (2) (just above) implies

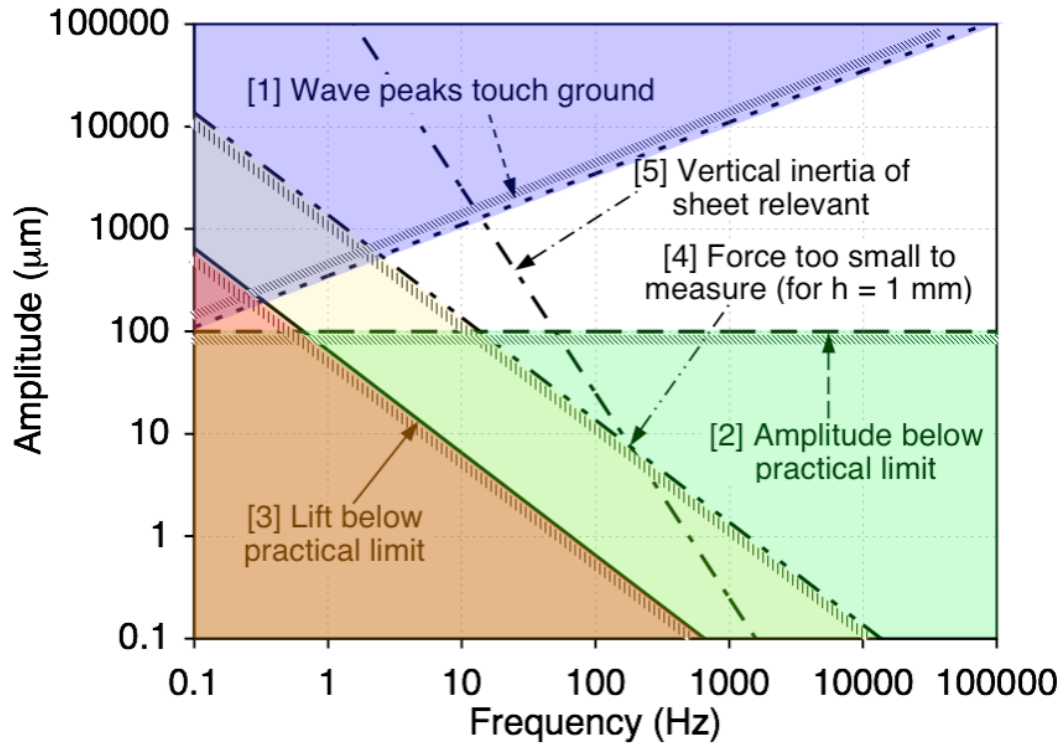


Figure 2.4 Diagram depicting different physical situations as a function of amplitude and frequency of the traveling wave. Colored regions indicate undesirable conditions. Condition 5 only weakly excludes the region to the right of the line shown.

$$A > (f \mu_{air} L^2 / \Delta\rho g D)^{1/2} \quad (3)$$

(This condition is only relevant for a freely moving sheet, where the lift is due to aerodynamics; in our experiments, the lift is provided by external means). Equation 3 is shown as a line in Figure 2.4, and the “undesirable” side of the line in amplitude-frequency space is indicated by shading.

{2} *Average non-planarity of sheet:* In practice, sheets made in experiments are not perfectly flat. Thus, the amplitude of vibration must be large enough to overcome any initial deviations from a perfectly flat sheet in order for the vibration shape to actually be close to that of a traveling wave (Figure 2.5b). Hence, we have a lower bound on the

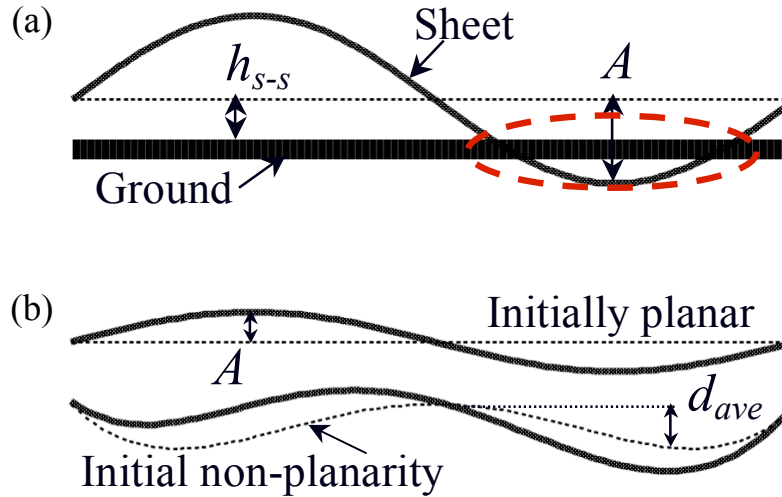


Figure 2.5 (a) When the traveling wave amplitude, A , is greater than the predicted steady-state lift height, h_{s-s} , the sheet would intersect the ground on part of its oscillation, which is nonphysical. **(b)** The amplitude of vibration, A , must be large enough to overcome any initial deviations, d_{ave} , from a perfectly flat sheet.

amplitude we can use: $A < d_{ave}$, where d_{ave} is the average non-planarity of the sheet. In our experiments, $d_{ave} \approx 100 \mu m$, hence in Figure 2.4 we plot:

$$A < 100 \mu m \quad (4)$$

{3} *Maximum non-planarity of sheet or ground:* When the sheet's forward velocity is too low, the predicted steady-state height will be less than some practical limit, determined by the maximum non-planarity of the sheet or the ground: $h_{steady-state} < d_{max}$, where d_{max} is the maximum non-planarity of the sheet or ground. This would result in some parts of the sheet dragging against the ground, and friction would dominate. Using (2) to substitute for $h_{steady-state}$, we obtain $(A f)^{1/3} \cdot (\mu_{air} L^2 / \Delta \rho g D)^{1/3} < d_{max}$. Experimentally, $d_{max} \approx 200 \mu m$, hence in Figure 2.4 we plot:

$$A \cdot f < (200 \mu m)^3 \cdot (\Delta \rho g D / \mu_{air} L^2) \quad (5)$$

{4} *Measurement limit*: For our initial experiments with tethered sheets, we seek only to detect a propulsive force, so we need to ensure that this force is greater than our lower measurement limit. For our experiments, this is $\sim 10 \mu\text{N}$ (see Section 5.1 and 3.4). Hence, by comparing this to the expression for propulsive force, $F_p \sim A f \mu_{air} W L^2 / h^2$, we can plot:

$$A \cdot f < (10 \mu\text{N}) \cdot (h^2 / \mu_{air} W L^2) \quad (6)$$

Note that, in this case, we have used a lift height of $h = 1 \text{ mm}$ (corresponding to our experiments), rather than the steady-state lift height, $h_{steady-state}$.

{5} *Vertical inertia*: For sufficiently high frequency and amplitude of the sheet's vibration, vertical inertia of sheet becomes relevant, and the actual propulsive force would be expected to be less than that predicted by (1). The onset of this effect begins essentially when the sheet's vertical acceleration is greater than gravity, or

$$A \cdot f^2 > g / 4\pi^2 \quad (7)$$

Note that this does not strongly mean that successful propulsion will not be observed, only that it might be weaker than predicted.

This analysis guides our choices for the parameters (such as A and f) used in our experiments by telling us where in parameter space we should expect the results to match the theory, and what we need to do to produce propulsive forces sufficiently large to enable accurate measurement. The region outside of all of the above regions (Figure 2.4; described by (3) to (7)) is the 'window of operation', in which we expect to see measurable forces similar to theoretical predictions, with forces maximized at the high frequency side. This region has a range of amplitudes from $\sim 100 - 1000 \mu\text{m}$, and a range of frequencies from $\sim 10 - 100 \text{ Hz}$. In summary, if the height h above the ground is fixed,

we want to make A as large as possible, but it can't exceed h . Reducing h is beneficial, but we can only go so far before running into practical issues (non-planarity) as described above. Finally, we need sufficiently high f and A to ensure a measurable force is produced, but going too high may not bring much benefit, due to vertical inertia.

The theoretical model presented in [3] and discussed above assumes that we can specify the exact time-varying shape of the sheet, and predicts what will occur if that shape is a traveling wave. If actuators alone are used to drive this deformation, we would actually be providing an internal bending force, not a direct deformation, and the actual deformation would depend on the interactions with the surrounding fluid and any other external constraints. It turns out that these interactions are minor at low vibration frequencies (<10 Hz) (see Chapter 4), but at the higher frequencies we need to operate at (~ 100 - 600 Hz), interactions between the sheet and its surroundings, and between different regions of the sheet, become significant. To alleviate this issue, we use integrated sensors to measure the deformation, and feedback to adjust the applied voltages as needed (Chapter 4). There are only four of these sensors, so we still do not know the exact shape, but rather an approximation. In future versions of this work, more sensors and actuators could be added to decrease the controllable vibration wavelength.

Chapter 3

Experimental Arrangement

In this chapter we describe the experimental arrangements used to create a thin sheet that can be deformed in time. Section 3.1 explains our choice of materials and device structure. In Section 3.2 we describe the operation of the piezoelectric actuators, and Section 3.3 describes the sensors. Section 3.4 discusses two methods for providing external lift. Finally, in Section 3.5, we bring together all of these pieces with a system overview.

3.1 Choosing Materials and Device Structure

Now that we have an understanding of the physics involved, and the relevant regimes of operation, we proceed to the experimental implementation. Our goal is a thin sheet that can be induced to vibrate in a traveling-wave shape. We need a material that is capable of vibrating at frequencies of 10s to 100s of Hz, at amplitudes of hundreds of microns; hence piezoelectrics are an attractive option. We chose Polyvinylidene Flouride (PVDF) because, although its piezoelectric coefficient, d_{31} , is not that big (23 pC/N), it is readily available in thin, flexible sheets. Piezoelectrics with higher piezoelectric coefficient, such as PZT, typically need to be grown on rigid substrates, such as MgO. This limits their usefulness for ‘large’ ($\sim 40 \text{ cm}^2$ for our samples), free-standing actuator sheets, unless

they can be transferred onto a flexible substrate [28]. A standard bimorph structure (two active layers glued together with an inactive adhesive; see Figure 3.1a, Figure 3.4a, and Section 3.2) is chosen to maximize bending for a given applied voltage, without making the film too flexible. Figure 3.1c shows a comparison of the curvature, $1/R$, of a bimorph and a unimorph (a single active layer on an inactive substrate; Figure 3.1b), versus thickness of the inactive layer (adhesive for the bimorph and substrate for the unimorph). We assume that the Young's Modulus, Y , of the inactive layer is the same as the active layers, the active layers are $28 \mu\text{m}$ thick (t_{PVDF}), and the applied voltage, V , is 100 V. For the unimorph, we see that the maximum curvature occurs for a substrate of half the thickness of the active layer. The expression for the curvature of the unimorph is $1/R = 6 d_{31} t_s V / (t_{PVDF} + t_s)^3$, where t_s is the substrate thickness [11]. For the bimorph, the curvature is maximized when the adhesive's thickness goes to zero (see Section 3.2). Besides a practical limitation on how thin the adhesive can be made, we also see that the stiffness of the sheet drops as the inactive layer is thinned. This can be seen in the plot of blocking force (the external force that would be required to prevent the bimorph from bending), F_{block} , in Figure 3.1d. The expressions for the blocking force of the bimorph and unimorph are, respectively, $F_{block} = 1.5 (W/L) (t_{PVDF} + t_a) d_{31} Y V$ and $0.75 (W/L) t_s d_{31} Y V$, where W and L are the width and length of the actuator (for the plots shown in Figure 3.1, $W = 4 \text{ cm}$ and $L = 2.5 \text{ cm}$), and t_a is the thickness of the adhesive layer [11]. A more flexible sheet results in greater deviations from flatness when no voltage is applied to the sheet, and less force available for pumping the air when the voltages are applied. Hence, we need to balance these two metrics to find an optimal structure. The adhesive we used came in $15 \mu\text{m}$ layers (see discussion below and Figure 3.2), and one such layer resulted

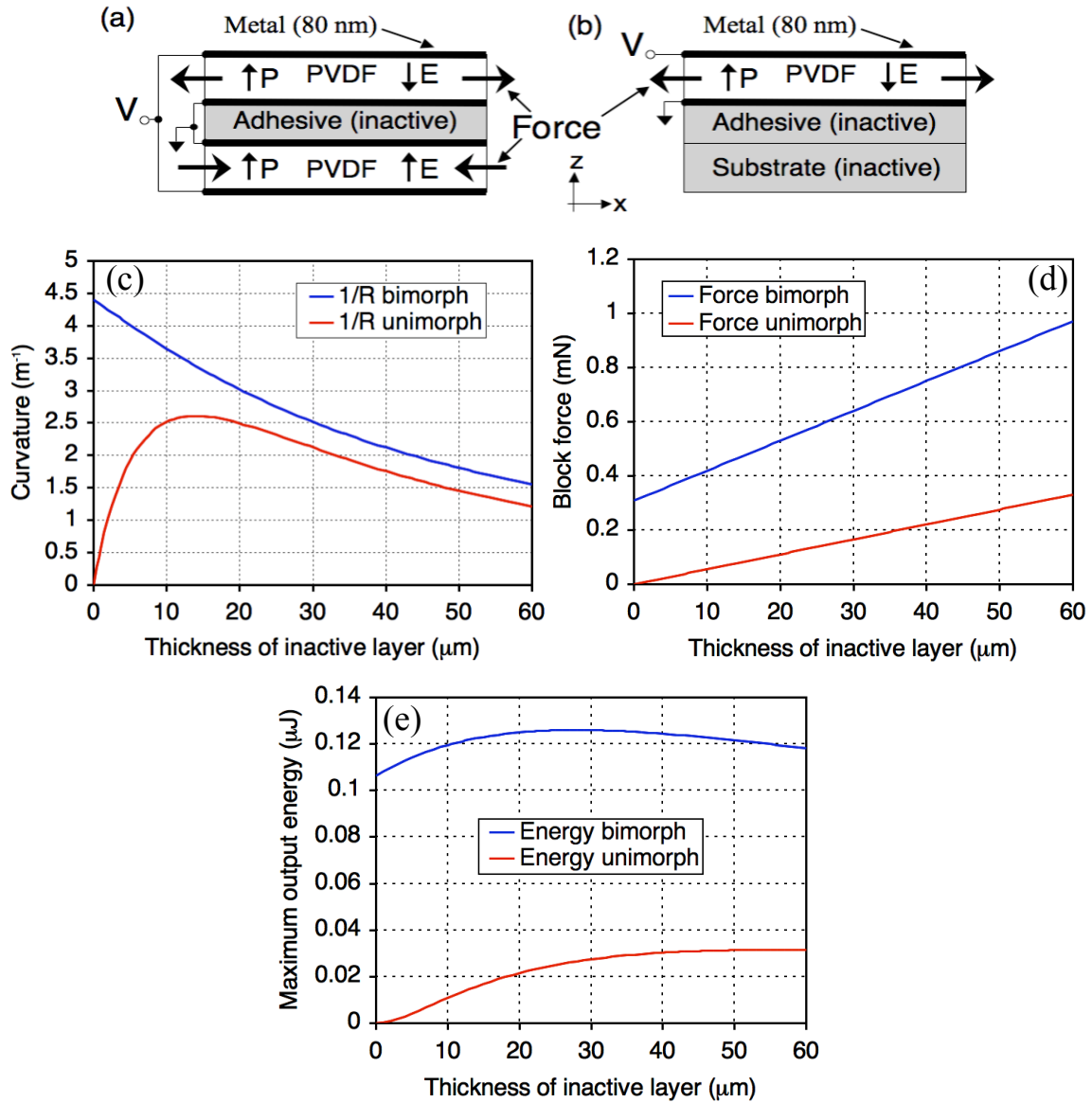


Figure 3.1 (a) Bimorph structure. E is the electric field and P is the polarization (see Section 3.2). (b) Unimorph structure. (c) Bending radius of bimorph and unimorph. (d) Blocking force of bimorph and unimorph. (e) Maximum work output of bimorph and unimorph. The “inactive” layer is adhesive for the bimorph and adhesive plus inactive substrate for the unimorph. The thickness of the electrodes (~ 80 nm) is ignored.

in a sheet that was a bit too flexible, so two layers were used. As it turns out, this is close to the thickness for maximum output energy of the actuator (maximized over an external load perpendicular to the deflection), shown in Figure 3.1e. The maximum energy output

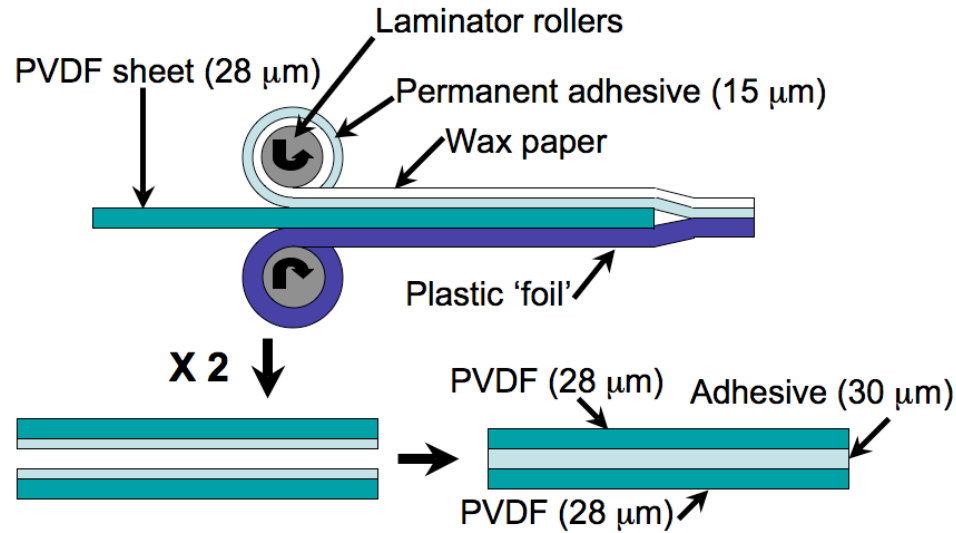


Figure 3.2 This laminator schematic shows how the piezoelectric bimorph structure is formed.

occurs at a load equal to half of the blocking force, and a deflection equal to half of the free deflection (i.e. the deflection when no external force is applied), thus in Figure 3.1e, we plot $0.25F_{block}\delta_{free}$, where $\delta_{free} = L^2/2R$.

To form the bimorph structure, two sheets of metal-coated Polyvinylidene Flouride, or PVDF (Measurement-Specialties, Inc.; 1-1003702-7), are glued together with a thin layer of adhesive. The adhesive is first applied to each sheet using a small laminator (Figure 3.2), and then the two adhesive-coated sheets are pressed carefully together, resulting in the final structure consisting of two PVDF sheets with $\sim 30 \mu\text{m}$ of adhesive ($t_{adhesive}$) between them. Each PVDF sheet is $28 \mu\text{m}$ thick (t_{PVDF}) and coated with 70 nm of copper and 10 nm of nickel. The metal coating on both sides of each PVDF sheet is patterned into eight regions – four of which are used as actuators (25 mm by 35 mm), and four of which are used as sensors (25 mm by 3 mm) (Figure 3.3). We achieve this patterning by using Scotch tape to cover the regions where we want the metal to remain, and using

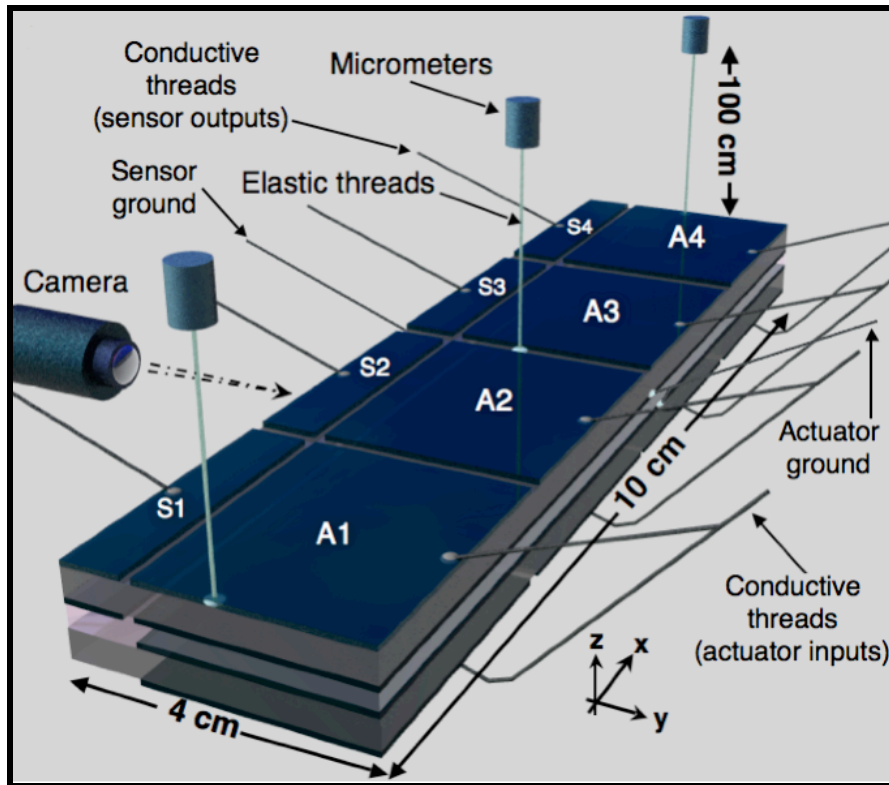


Figure 3.3 Model of the experimental arrangement, showing PVDF bilayer with electrodes, suspension from elastic threads, and microscope for imaging. The metal layers are patterned to form actuators (A1-A4) and sensors (S1-S4), and electrical connections are made using conductive threads.

Ferric Chloride (a typical copper etchant) to etch the exposed metal. Loose conducting threads (diameter $\sim 50 \mu\text{m}$) are attached, using conductive silver-based epoxy, to each electrode and to the common plane between the sheets to apply and sense voltages. The threads come coated with silver to make them conductive.

3.2 Actuator Operation

The actuators operate when electric fields of opposite polarity, relative to the polarization direction, are applied across the two PVDF layers, which causes one layer to expand and the other to contract, resulting in bending (Figure 3.4a). The PVDF was

oriented so that the coefficient of expansion was much larger in the x -direction (Figure 3.4c, $d_{31} = 23 \text{ pC/N}$) than in the y -direction ($d_{32} = 2.3 \text{ pC/N}$), allowing the bending to be considered unilateral. The manufacturer achieved this by stretching the film in the x -direction during poling (applying a high voltage across the film). Note that this still restricts our choice of the width of each actuator to be, at most, similar to its length. The normal stress in the x -direction, σ , induced in each PVDF layer (with Young's Modulus, $Y \approx 2 \text{ GN/m}^2$) by an applied voltage V_A is then: $\sigma = d_{31} Y V_A / t_{PVDF}$. For the structure depicted in Figure 3.4a (and assuming that the adhesive's Young's Modulus is equal to that of the PVDF), it has been shown [11] that for constant applied voltage, the resulting curvature, $1/R$, produced by this stress is:

$$\frac{1}{R} \approx \frac{12d_{31}(t_{Epoxy} + t_{PVDF})}{(t_{Epoxy} + 2t_{PVDF})^3} \cdot V_A \quad (8)$$

To test this equation, a single such actuator was constructed (i.e. a cantilever), and the tip deflection (equal to $0.5 L^2 * 1/R$, where L is the length of the cantilever) was measured with a camera. The values obtained were ~ 3 times smaller than Equation (8) would indicate. One possible explanation is that the adhesive layer has a higher Young's Modulus, however this was not fully explored. We then construct a sheet with four of these actuators along its length, and control the dynamic shape of the sheet by applying different time-varying voltages to each of the four actuators (Figure 3.4b). In order to produce the time-varying voltages, which potentially need to have several-hundred-volt amplitudes at several-hundred-hertz frequencies, four basic op-amp (APEX Precision Power PA94) gain circuits are used (Figure 3.5) to amplify signals generated from a data acquisition board (DAQ) controlled by LabView (see Section 3.5). Several additional

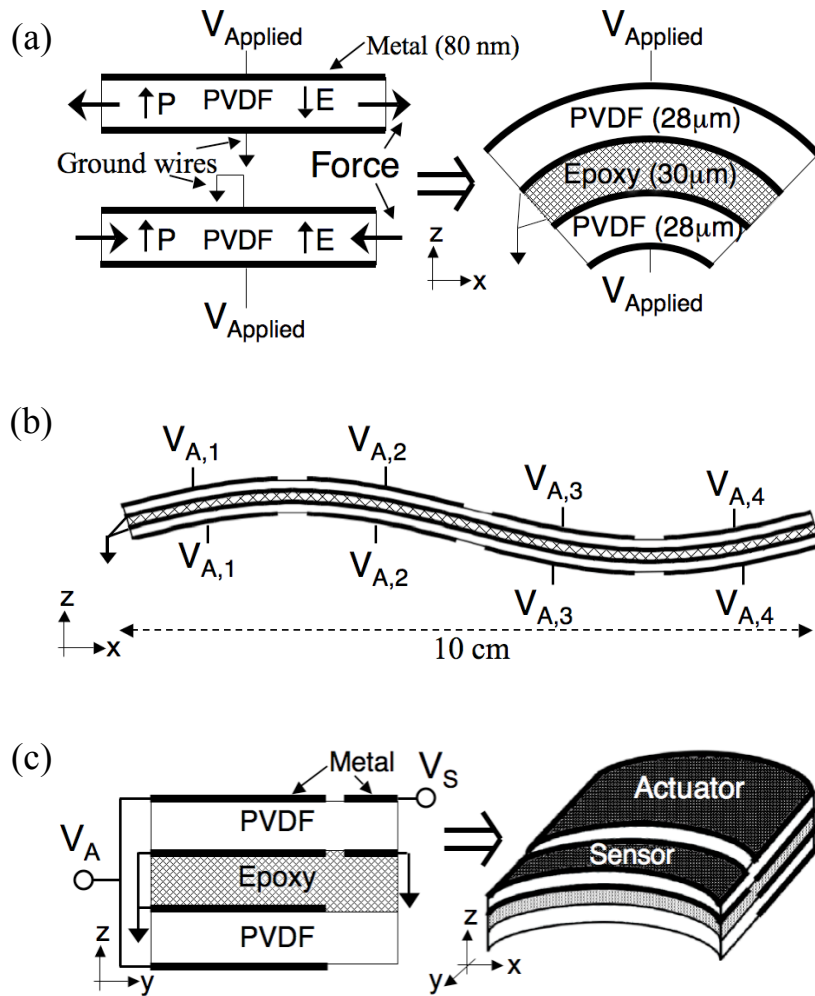


Figure 3.4 Details of actuator and sensor operation. **(a)** Actuator cross-section: the applied electric field (E) has opposite polarity with respect to the polarization (P) in the top and bottom PVDF layers, leading to opposing expansion/contraction forces, and thus bending. **(b)** Four actuators patterned along the length of the sheet allow control of its dynamic shape. **(c)** Cross-section showing a sensor integrated next to its corresponding actuator. Note: the sensors and actuators have separate ground terminals to minimize capacitive pickup. Since the sensor regions are relatively small, they bend along with the actuators.

components are also used, as suggested by the op-amp manufacturer: Zener diodes are connected between ground and the DC power supplies for the op-amps (± 400 V) to prevent overloading of the op-amp - if the power supplies reach 40 V beyond their rated

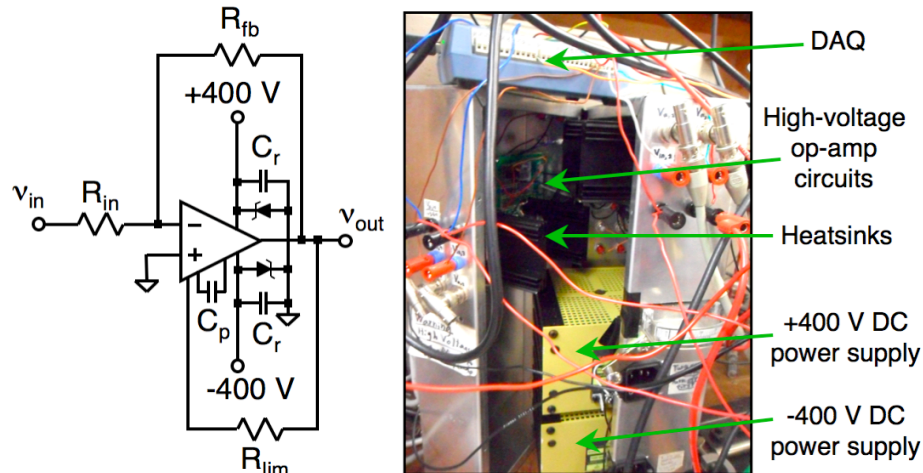


Figure 3.5 A high-voltage amplifier for PVDF actuation. The zener diodes and capacitors C_r protect against power supply transients, C_p is for phase compensation (different values used depending on gain range), R_{lim} is for current limiting, and the gain (v_{out} / v_{in}) is given by R_{fb} / R_{in} . The values used were: $C_r = 10$ nF, $C_p \sim 3$ pF, $R_{lim} = 7.2$ Ω , $R_{fb} = 300$ k Ω , $R_{in} = 2.2$ k Ω , and the zener diodes breakdown at 440V.

value (note that the power supplies are unregulated), the zener diodes would reach breakdown. C_p is a compensation capacitor used to ensure that the feedback is stable (i.e. the phase shift is not too big). The manufacturer recommends a value of at least 2.2 pF when the gain is around 100 or more (gain is ~ 136 in our circuit). The capacitors C_r protect against power supply transients, and R_{lim} is an external resistor used to limit the current to 0.7 V / R_{lim} (the maximum current that the op-amp can handle is 200 mA).

3.3 Sensor Operation

Piezoelectric sensors are used to measure the actual time-varying shape of the sheet, which allows the actuator control signals to be adjusted to produce a traveling wave. This step is necessary because at higher frequencies (>10 Hz), dynamic effects and nonlinearities cause the deformations to differ from that expected from the applied

actuator voltages. The sensors are created with the same structure as the actuators, but only in one of the PVDF layers to minimize the number of connections required. Because the sensors are small in width compared to the actuators, we assume that the curvature of each sensor is the same as the curvature of its corresponding actuator (Figure 3.4c). Each sensor measures the average curvature over its area by producing an internal charge in the PVDF, Q_{int} , when subjected to a strain ε , given by: $Q_{int} / Area = -d_{31} Y \varepsilon$. Since the PVDF is essentially a capacitor, this expression can be rewritten as $V_{int} = -d_{31} Y (t_{PVDF} / \varepsilon_0 \varepsilon_r) \varepsilon$, where $\varepsilon_r \approx 13$ is the dielectric constant of PVDF. From a simple geometric analysis we see that, for a given curvature $1/R$, the average strain, ε , in the PVDF is given by: $\varepsilon = (t_{PVDF} + t_{Epoxy}) / 2 R$. Thus, we have:

$$V_{int} \approx -\frac{d_{31} Y (t_{PVDF} + t_{Epoxy}) t_{PVDF}}{2 \varepsilon_0 \varepsilon_r} \cdot \frac{1}{R} \quad (9)$$

We use a charge integrator and amplifier circuit (Figure 3.6) to measure this internal voltage, resulting in a signal $V_s = V_{int} (C_{PVDF}/C_I) (R_2/R_I)$. A high-pass filter after the charge integrator ensures that drifting of the op amp output is not seen in the final measurement. This is valid until the op amp saturates, but could be avoided by adding a several-M Ω resistor in parallel with C_I . When V_s is multiplied by an appropriately chosen software gain $G = -\frac{2}{d_{31} Y (t_{PVDF} + t_{Epoxy}) A_{sensor}} \cdot \frac{R_I C_I}{R_2} \approx 8 \text{ V}^{-1} \text{ m}^{-1}$ (for our measurement circuit, $C_I = 50 \text{ nF}$, $R_I = 10 \text{ k}\Omega$, and $R_2 = 660 \text{ k}\Omega$, and the typical sensor area is $\sim 0.7 \text{ cm}^2$), the result, $\kappa = V_s \cdot G$, is numerically equal to the local curvature $1/R$. This measured curvature was found to be ~ 4.5 times smaller than expected from Equations (8) and (9) for a given applied voltage (see Figure 4.1). Most of this difference can be explained the factor of 3 discrepancy in the actual curvature (Section 3.2), leaving a factor of 1.5 error in the

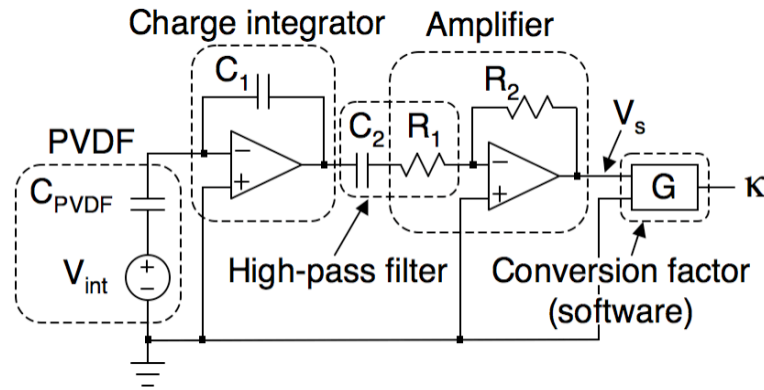


Figure 3.6 Circuit diagram for measurement of sensor voltages (V_s) using charge integrator, high-pass filter, and amplifier. Curvature (κ) is calculated using software gain, G .

sensor measurement. This was not investigated further. We can then construct the cross sectional shape of the sheet as a function of time by assuming that each region has a constant curvature over its area, corresponding to the sensor measurement, and fitting together the four regions (assuming that the average height and tilt of the sheet are fixed).

Before proceeding further, we must ensure that the sensor signals result solely from the deformation-induced charge, as described above. This is particularly crucial, given the close proximity of the actuators (applied voltages up to a few hundred volts) to the sensors (measured sensor voltages are <1 V). To minimize capacitive pickup between the actuators and sensors, separate ground terminals are used (Figure 3.4c). That is, the metal electrodes between the sheets that act as ground are patterned to isolate the region under the sensors from that under the actuators. However, this is not sufficient, as can be seen in Figure 3.7a: a 200 V sine wave is applied to actuator 2, the resulting signals from all four sensors are measured. Note that, from equations (8) and (9), if a voltage is applied to one actuator, the signal on the corresponding sensor should have the opposite sign. Since this is not the case in Figure 3.7a, capacitive pickup from the actuator is likely still

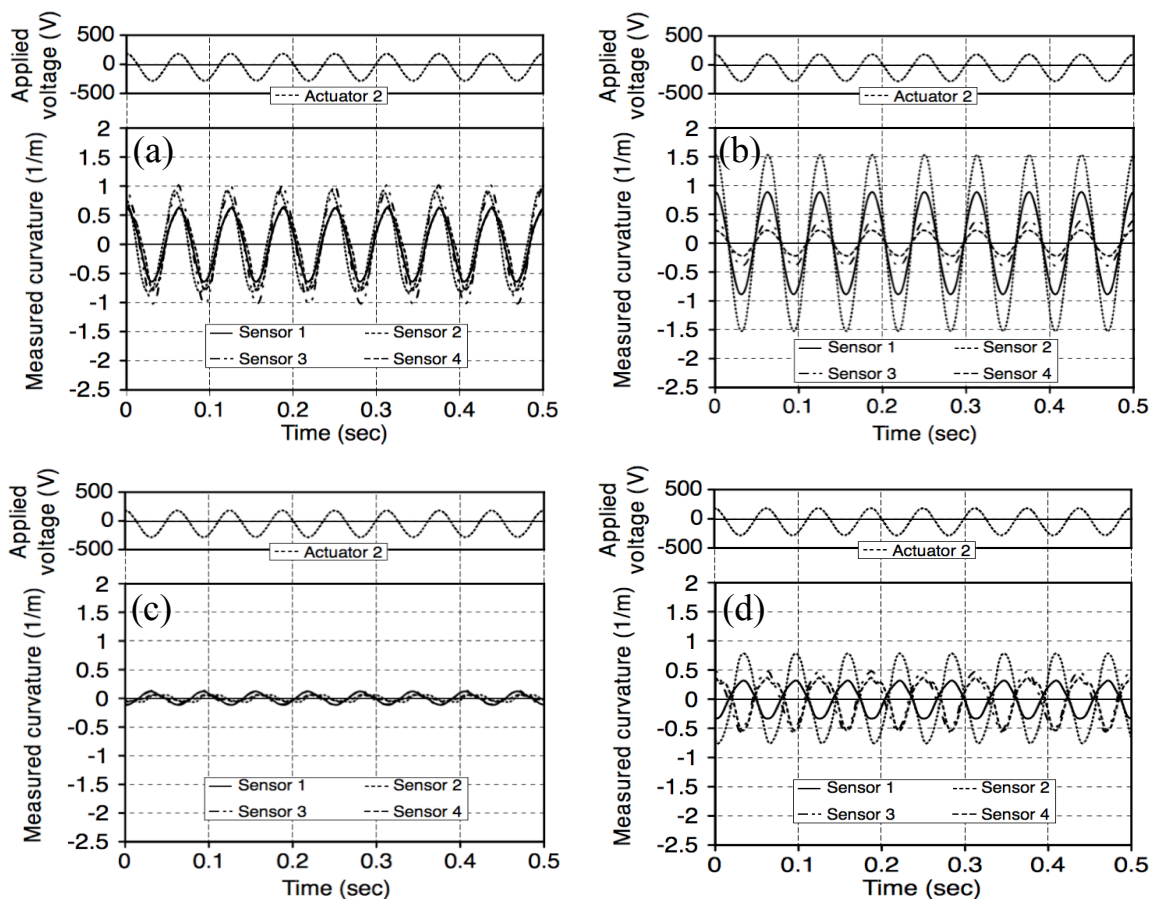


Figure 3.7 Elimination of capacitive coupling – measured sensor signals are shown for a 200 V amplitude, 16 Hz sine wave applied to actuator 2. **(a)** Uncorrected sensor measurements. **(b)** Sensor measurements with a weight on the sheet to physically prevent it from vibrating, showing significant signals due to capacitive coupling. **(c)** Sensor signals after software has subtracted off this artifact. **(d)** With the weight removed, the full true sensor signals are now observed.

resulting in a significant artifact. To test this, the sheet is physically prevented from vibrating (Figure 3.7b) by placing weights on the sheet, resulting in signals that are purely artifacts due to capacitive pickup from the applied actuator voltage. Now that we know the magnitude of the artifacts (proportional to the applied voltage), we proceed to Figure 3.7c, in which these artifacts have been subtracted from the measured signals, resulting in sensors signal close to zero. The small residual signal could be the result of a

slight phase mismatch (i.e. if the coupling between the applied voltage contacts and the sensor contacts is not purely capacitive). However, it could just as well be due to some small real vibration that was not completely suppressed by the weights, so we treat this residual signal as background noise. When the weight is removed, allowing the sheet to vibrate again, the true sensor signals due to deformations can be seen (Figure 3.7d).

3.4 Means of Suspension

Due to external connections for power and control circuitry, the sheet was not entirely free, so it would not be able to reach the speeds necessary to generate its own lift (as predicted by theory [3]). Hence, two experimental arrangements were used to provide external lift. This is necessary since the propulsive force that we wish to study depends on the elevation h of the sheet above the ground (Section 2.1).

3.4.1 Elastic Threads

In one arrangement, the sheet is suspended from three 1 m-long threads (distinct from the conductive threads mentioned above), which are elastic to allow the sheet the freedom to bend as desired (Figure 3.8a and Figure 3.3). That is, the force required to stretch the elastic threads by the desired displacement (several hundred microns) must be small compared to the force that the PVDF can exert. For constant applied voltage, this force is given by $F_{max} = 1.5 (W/L) (t_{PVDF} + t_{adhesive}) d_{31} Y V_A \approx 0.64 \text{ mN}$ for 100 volts. Thus, we desire elastic threads with spring constant, k_t , less than $\sim 0.06 \text{ mN} / 300 \text{ } \mu\text{m} \approx 0.2 \text{ N/m}$. Figure 3.9 shows displacement versus force for several elastic threads. These threads all show non-linear behavior, so the relevant effective spring constant is the slope of the

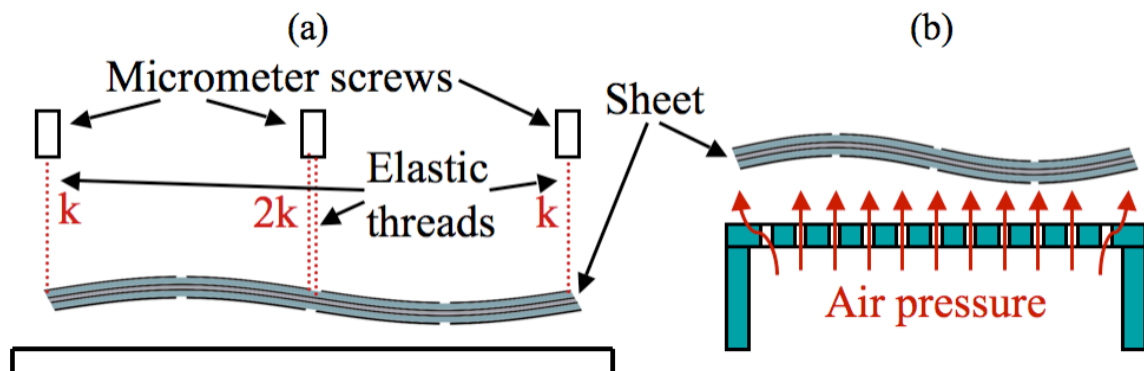


Figure 3.8 (a) Suspension using elastic threads. (b) Suspension using miniature “air table”.

force-displacement curve at the force resulting from $\frac{1}{4}$ of the weight of the sheet (which is the fraction carried by each thread – see below), or ~ 1.6 mN for a sheet weighing ~ 0.64 mg. Thread #1, which is new (from a sock), does not have a low enough spring constant at this load ($k_t \approx 0.45$ N/m). However, thread #2 has $k_t \approx 0.15$ N/m, which is sufficiently small to have minimal effect on the sheet’s vibration. This thread was ‘old’, i.e. the elastic was worn out, resulting in a lower spring constant at low loads. However, as the elastic was degrading, it did not last, and had to be replaced. Luckily a new thread was obtained which had a lower spring constant when new ($k_t \approx 0.19$ N/m; thread #3 plot in Figure 3.9) – not quite as good as the aged thread, but still within our requirements. No significant difference in experimental results was observed between thread #2 and #3.

To ensure that the sheet is balanced at all times, three elastic threads are needed, one at each end and one in the center with twice the spring constant (this is achieved by using two threads in the center). To see why, first note that to prevent the sheet from tipping, any forces from suspension threads must be symmetrical about the center at all times. For a traveling wave shape, this means that any supports not at the center must be one wavelength apart, i.e. at the two ends of the sheet in our case. In addition, the average

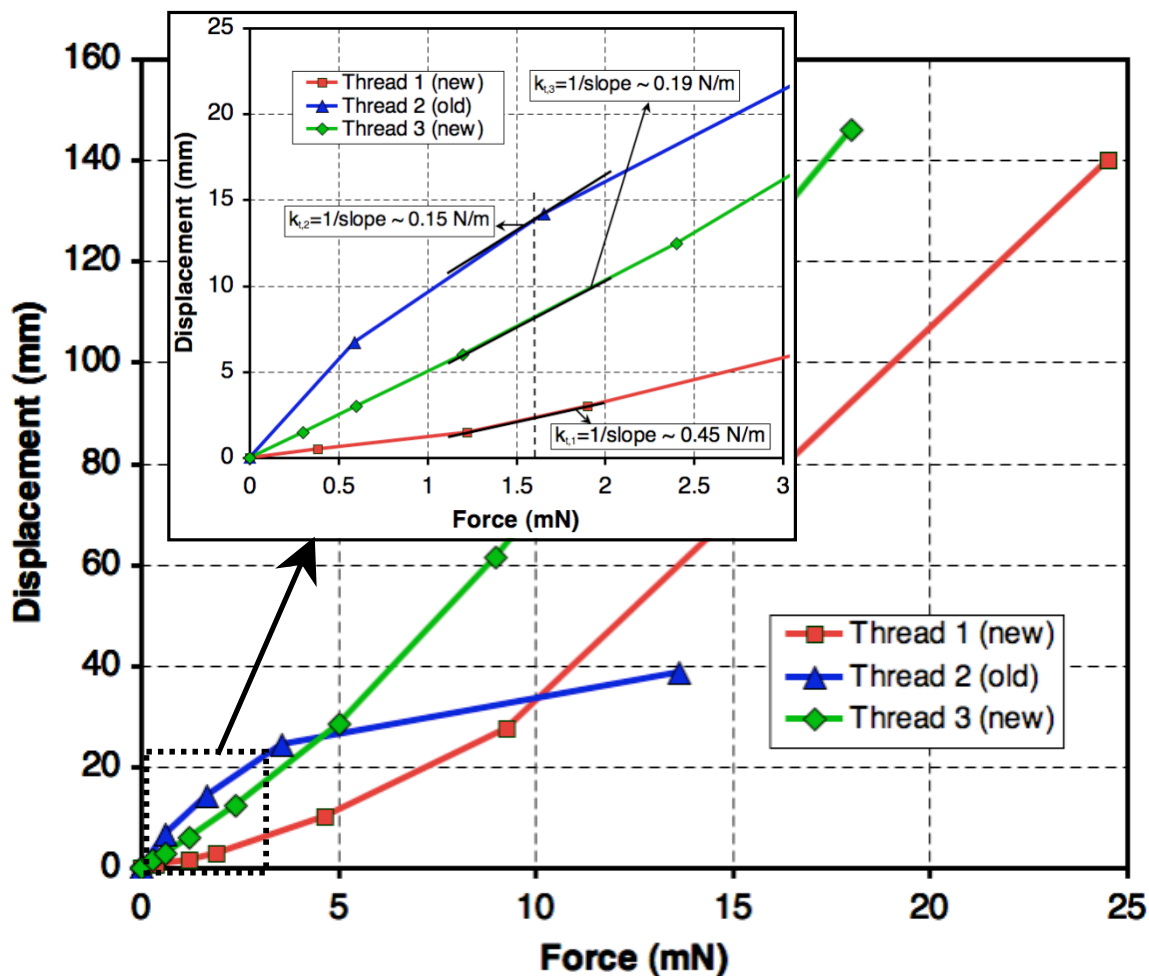


Figure 3.9 Characterization of elastic threads.

height of the sheet must be fixed in time, so a thread of twice the spring constant is needed in the center of the sheet to compensate for the ones at the ends (the center thread supports twice the mass as the end threads).

3.4.2 Air Table

In the second arrangement, the sheet is elevated above a miniature “air table” (Figure 3.8b) using pressurized N_2 , so no threads are needed for suspension. This “air table” is ~ 15 cm long and ~ 10 cm wide, and has an array of holes 1 cm apart over its surface. As

purchased, the airflow was a bit higher in the center of the table, so an additional plastic plate with fewer holes in the center was placed between the N₂ source and the top surface. This experimental arrangement is “cleaner”, due to the absence of vibrating suspension threads. However, the height between the sheet and the table can only be adjusted by varying the air pressure, so there is not the fine-tuned control that the suspension-thread arrangement provides. We will see in Section 5.1 that the airtable’s airflow does not have a significant effect on sheet’s propulsion.

3.5 Overall Setup

A block diagram of the system is shown in Figure 3.10. A LabView program sends signals to a data acquisition board (DAQ; USB-1208HS-4AO from Measurement Computing), which outputs four analog time-varying voltages. Since the DAQ can only output voltages up to ± 10 V, high-voltage amplifiers used to amplify the signals up to the necessary ± 400 V range. These signals are then sent to the actuators (connection made via conductive threads) to vibrate the sheet. The connection to the sensor is also made via conductive threads, but to minimize capacitive coupling, these are then connected to coaxial cables for most of the distance to the measurement circuits (Figure 3.11). These charge integrators produce voltages signals that can be read by the DAQ, and sent back to the LabView program. To allow for easy synchronization of the applied actuator voltages and the measured sensor voltages, the actual applied voltages (i.e. after the amplifier) are measured with a voltage divider, and connected to the same DAQ as the measured sensor signals (Figure 3.10). This way, the relative phase of the applied voltages and the

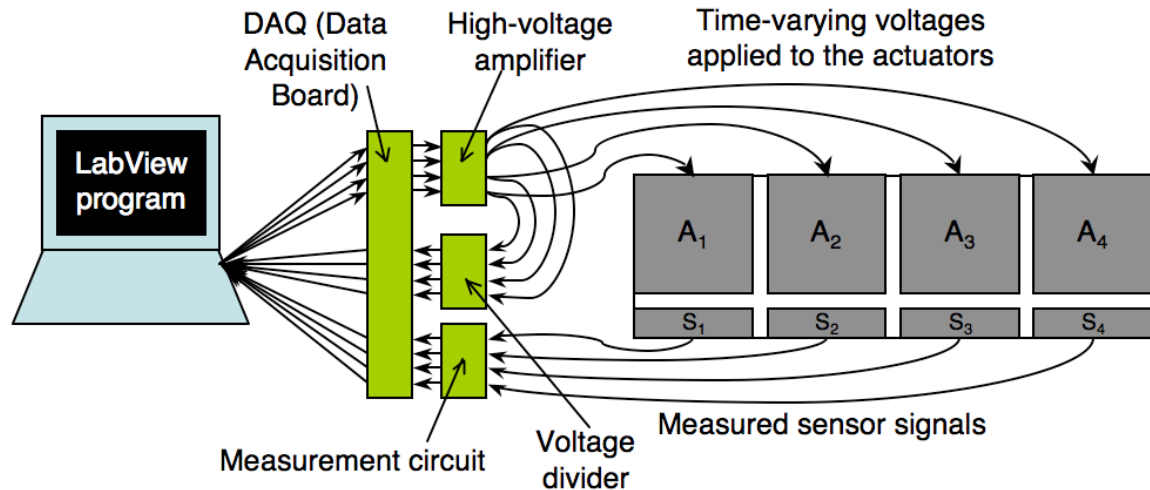


Figure 3.10 Block diagram of system. A_1 to A_4 are the actuators and S_1 to S_4 are the sensors.

measured voltages is known, even if delays occur in the transmission of information from the computer, through the DAQ, and through the amplifier.

Since the sheet is quite light (~ 0.63 g), and the expected propulsive forces quite small (~ 10 - 100 μN), it is important that the sheet is protected from air currents in the lab (due to air conditioning, etc.), especially for the elastic threads arrangement. Thus the sheet is operated inside a Plexiglas box (Figure 3.11), which is mounted on an optics breadboard. The box also provides safety from the exposed high voltages (up to 400 V) on the actuator electrodes and the conductive threads connecting to the actuators. Holes were drilled in the top to accommodate the 1 m long suspension threads (in the artificial rendering shown in Figure 3.11a, which illustrates the suspension thread arrangement, the threads are shorter, and so are shown affixed to the top cover of the box). Micrometer screws on top are used to adjust the elastic suspension threads to obtain a level sheet. A micrometer stage under the surface on which the sheet moves allows fine-tuned control of the gap between the sheet and the ground. The use of the high-speed camera is

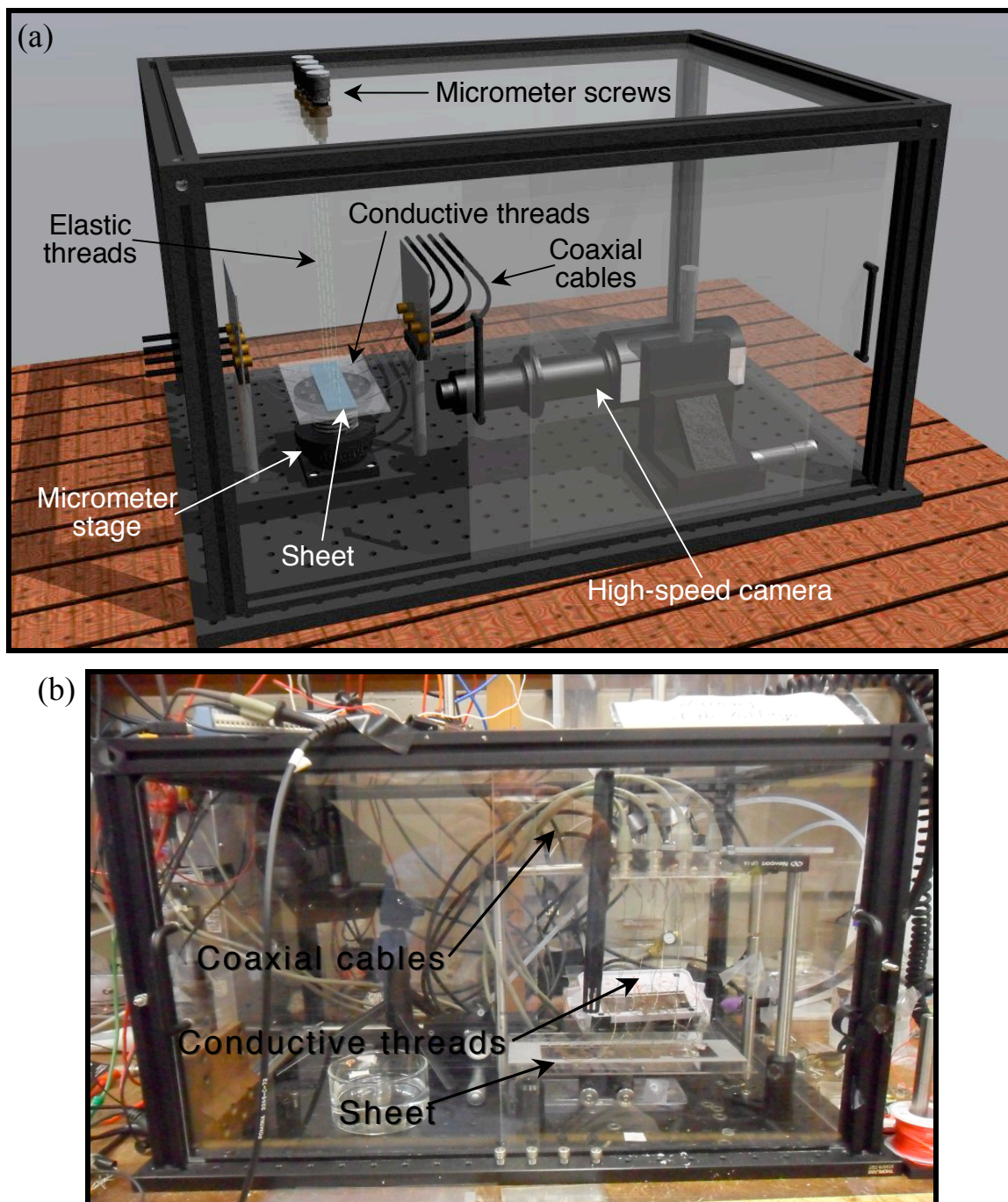


Figure 3.11 Enclosed box to protect sheet and camera – concept (a) and realization (b).

described in Section 4.5. In Figure 3.11b, we show a photo of a later version of the arrangement, in which the sheet is resting on a small platform with adjustable angle (see Chapter 7).

Chapter 4

Control of Traveling Wave Shape

In this chapter we describe why active control of the sheet's deformations is needed, and discuss several approaches towards implementing such control. Section 4.1 describes the need for active control, and thus real-time sensing, of the shape of the sheet. In Section 4.2 we describe general considerations about the control algorithm we choose. Section 4.3 describes a linear control approach, and Section 4.4 describes feedback for correction of non-linearities. Finally, in Section 4.5, we verify the actual shape of the sheet versus time using a high-speed camera, after all of the control algorithms are implemented.

4.1 Need for Sensors

We began our experiments by initially applying low frequency (<10 Hz) traveling waves of voltages to the actuators, and observed through the sensors that deformations were close to the desired traveling waves (Figure 4.1). An example of such a low frequency (2 Hz) traveling wave can be seen in Video 4.1 of the online supplemental material. However, as seen in Figure 2.4, these frequencies are expected to be too low to give an observable propulsive force. At higher frequencies, nonlinearities and interactions between different regions of the sheet caused the deformations to be far from a traveling wave for traveling waves of voltages applied to the actuators. Figure 4.2 shows an

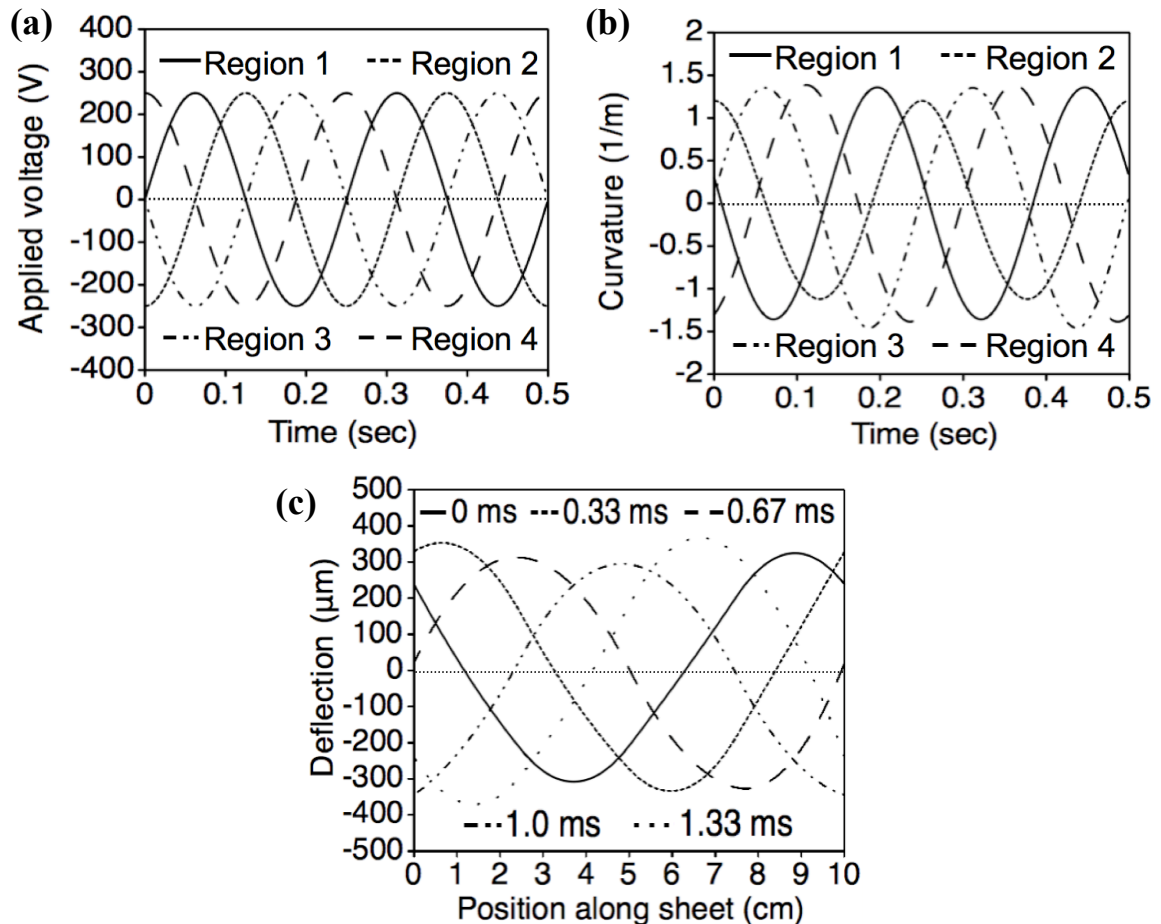


Figure 4.1 At low frequencies (4 Hz in this example), applying a traveling wave of voltages is sufficient to bend the sheet in a shape close to a traveling wave. **(a)** The voltages applied to each region of the sheet. **(b)** The average curvatures as determined from the sensor readouts. **(c)** The reconstructed shape of the sheet at various times.

example of these measurements, and demonstrates the need for integrated sensors and feedback. Parts (a), (b), and (c), show, respectively, the applied voltages, curvatures determined from the sensor voltages, and cross-section of the sheet constructed from the sensor readouts. This reconstruction is formed by assuming a constant curvature in each of the four sections of the sheet, as measured by the four sensors, and piecing together these sections. It is assumed that there are no kinks in the sheet (i.e. dy/dx is continuous, where y is the vertical deflection of the sheet, and x is the position along its length), and

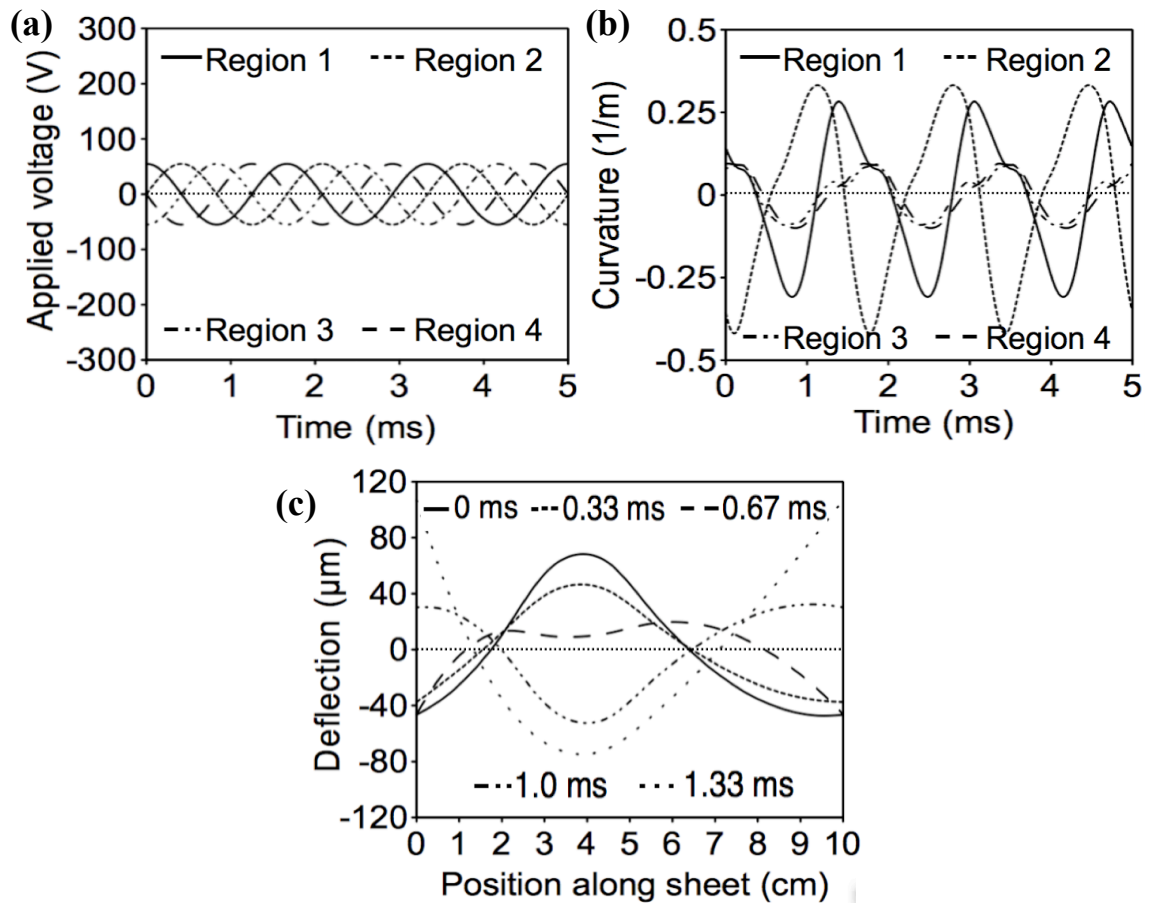


Figure 4.2 Applying a traveling wave of voltages at high frequencies (600 Hz in this example) results in a shape that is nearly a standing wave, rather than the desired traveling wave. **(a)** The voltages applied to each region of the sheet. **(b)** The average curvatures as determined from the sensor readouts. **(c)** The reconstructed shape of the sheet at various times.

that the average height and tilt of the sheet are constant in time. We show the result of applying high frequency ($f_0 = 600 \text{ Hz}$) traveling waves of voltages (Figure 4.2a) to the actuators – the sensor signals (Figure 4.2b) indicate that the sheet's vibration (Figure 4.2c) is closer to a standing wave than a traveling wave. In general, standing waves are easier to produce than traveling waves, as shown in Video 4.2 of the online supplemental material for a resonance at 16 Hz (the applied voltages are the same for each actuator in

this example) – a large amplitude of ~ 1 cm results. However, standing waves are not useful for our application.

4.2 Choice of Control Algorithm

Some prior works have investigated mechanisms for damping vibration using arrays of piezoelectric elements, which has even been accomplished using passive electrical networks [9], [7], but for our objectives, we need more – we need to actually produce a particular desired vibration. As we will see later, we will need to dampen unwanted vibrations at other frequencies, which could be approached with a passive network, however since we need the ability to change the desired vibration frequency, and the control system for producing these vibrations is already setup, it is convenient to use the same system for canceling unwanted vibrations. The first step in attempting to control the vibration of the sheet is to determine the vibration that results from a known applied voltage waveform to each of the four actuators. Since our objective is a traveling wave deformation, it makes sense to analyze the system in Fourier space. We proceed by first measuring a linear approximation of the system at the desired driving frequency, as described in Section 4.3 below. We will see that this is often not sufficient, so in Section 4.4, we move on to a solution using feedback to adjust the applied voltages, which allows us to proceed without needing to fully characterize the non-linear behavior of the system. Research has been conducted on analytical and numerical simulations of wave propagation generated by a piezoelectric actuator bonded to an elastic substrate [15], however the conditions are somewhat different. For example, [15] considers a single actuator on an infinite (in length and thickness) substrate, in contrast to our device, in

which the actuators comprise most of the substrate, and there are four different interacting actuators to deal with. In addition, the external environment surrounding the sheet can involve more complicated boundary conditions (e.g. elastic thread suspension), and is often different from experiment to experiment. Together, these features make the use of integrated sensors and feedback an attractive solution.

4.3 Linear Control

A linear approximation to the relation between applied voltages and measured curvatures at a given frequency, f_0 , is determined by applying a sine wave of frequency f_0 to one actuator at a time, and measuring the response at each of the four sensors. Converting to Fourier space, this results in a 4x4 complex matrix

$$\mathbf{S}_{f_0} \equiv \begin{bmatrix} S_{1,1} & S_{2,1} & S_{3,1} & S_{4,1} \\ S_{1,2} & S_{2,2} & S_{3,2} & S_{4,2} \\ S_{1,3} & S_{2,3} & S_{3,3} & S_{4,3} \\ S_{1,4} & S_{2,4} & S_{3,4} & S_{4,4} \end{bmatrix}, \quad (10)$$

where each coefficient $s_{j,k} = \frac{m_k}{a_j} e^{-i(\varphi_k - \phi_j)}$ corresponds to a measured signal of $m_k \cos(2\pi f_0 t + \varphi_k)$ on sensor k when a voltage $a_j \cos(2\pi f_0 t + \phi_j)$ is applied to actuator j. If the system were linear and time invariant, it would be sufficient to adjust the amplitudes and phases of the applied voltage signals, which were still sine waves of 600 Hz, according to

$$\vec{V}_{Applied} = \mathbf{S}_{f_0}^{-1} \vec{V}_{Desired}, \quad (11)$$

where $\vec{V}_{Applied} \equiv [a_1 e^{-i\phi_1} \quad a_2 e^{-i\phi_2} \quad a_3 e^{-i\phi_3} \quad a_4 e^{-i\phi_4}]$ & $\vec{V}_{Desired} \equiv [d_1 e^{-i\varphi_1} \quad d_2 e^{-i\varphi_2} \quad d_3 e^{-i\varphi_3} \quad d_4 e^{-i\varphi_4}]$ are vectors consisting of the f_0 component of the Fourier Transforms of each of the four applied voltage signals and desired sensor signals, respectively (Figure 4.3a). Note that,

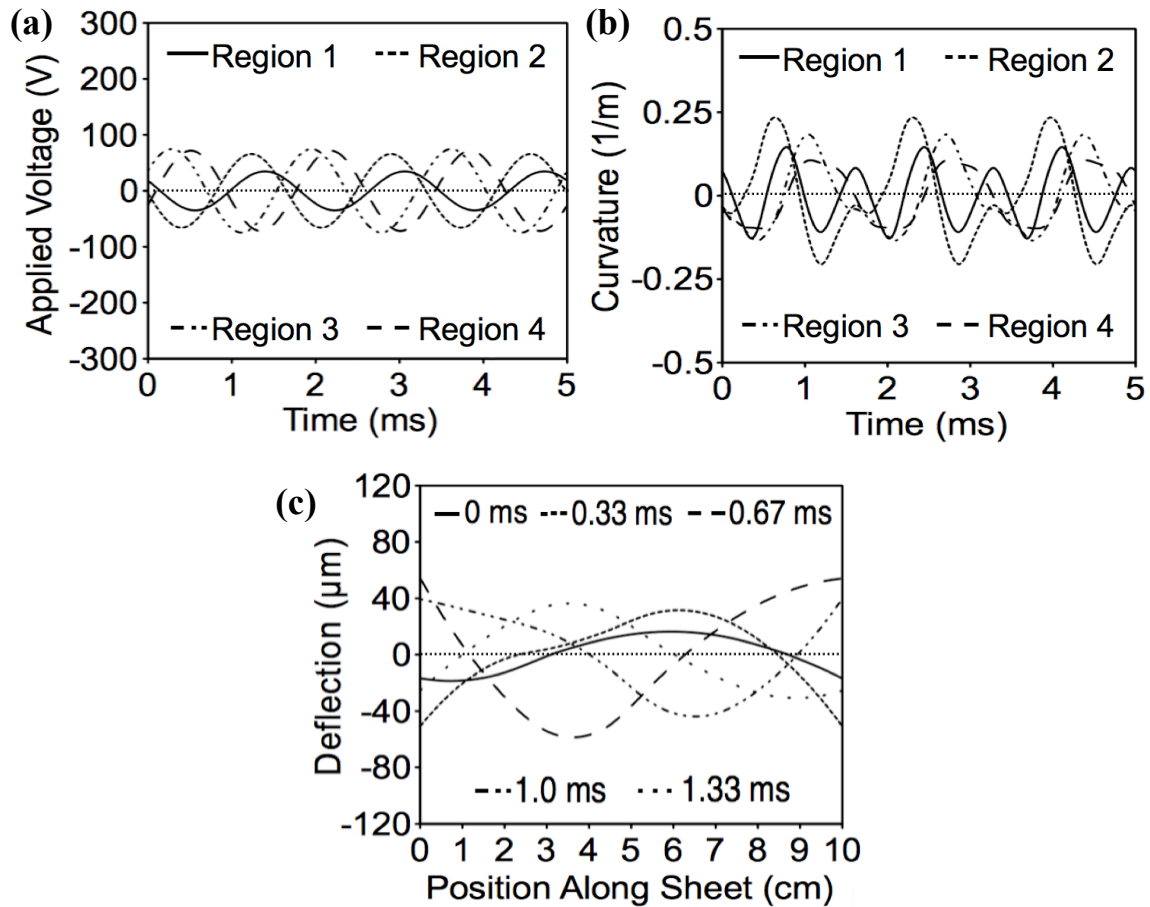


Figure 4.3 The applied voltage signals are adjusted (in amplitude and phase) using a linear control matrix (data shown is at 600 Hz). The reconstructed shape of the sheet is closer to a traveling wave, but still not ideal, and higher order harmonics are seen in the curvature signals. **(a)** The voltages applied to each region of the sheet. **(b)** The average curvatures as determined from the sensor readouts. **(c)** The reconstructed shape of the sheet at various times.

for a traveling wave, $\vec{V}_{Desired} = V_0[1 \quad \pm i \quad -1 \quad \mp i]$, where V_0 is the amplitude of the sensor signal corresponding to the desired traveling wave amplitude. With this adjustment, some improvement is seen, but the resultant vibration (Figure 4.3c) is still not close enough to a traveling wave – in particular, higher order vibrations can now be seen in the sensor signals (Figure 4.3b).

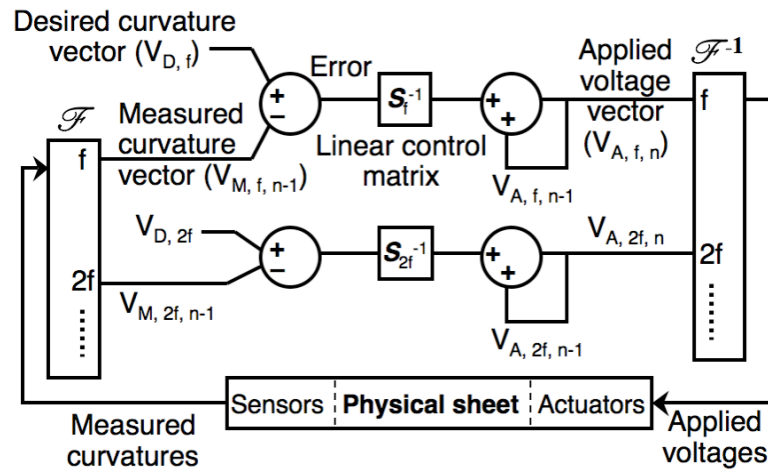


Figure 4.4 Feedback block diagram. The four measured curvatures are each Fourier Transformed, resulting in a curvature ‘vector’ for each frequency component. In each feedback cycle, the applied voltage vector is updated by adding the error from the previous cycle, while using the linear control matrix to ensure negative feedback. The feedback process is applied to several frequency components.

4.4 Feedback Control

Our next step is to remove these higher order frequency modes, as well as to correct for other nonlinearities, by using feedback. We apply feedback separately for each harmonic with a “significant” undesired component present (Figure 4.4). This involves first measuring the matrix S_f for each frequency of interest (i.e. $f = f_0, 2f_0, 3f_0, \dots$), by the procedure described above. These matrices then remain fixed for the rest of the experiment, unless we change the external environment (e.g. switching from the elastic-thread suspension to the air-table) or use a new sheet, in which the matrices are measured again. One reason that we use this computer-controlled approach, rather than an analog circuit, is that each of these matrices requires 32 parameters that would need to be set. The matrix itself is needed to ensure that negative feedback is occurring.

To begin the actual feedback process, we apply voltages to the four actuators (beginning with zero) for ~ 1 second, while measuring the response at each sensor. We then update the applied voltages (every second) according to:

$$\vec{V}_{Applied,f,n} = \vec{V}_{Applied,f,n-1} + \mathbf{S}_f^{-1} (\vec{V}_{Desired,f} - \vec{V}_{Measured,f,n-1}). \quad (12)$$

Note that, for $f = f_0$, $\vec{V}_{Desired,f_0} = V_0[1 \ \pm i \ -1 \ \mp i]$, while for all other harmonics, $\vec{V}_{Desired,f} = 0$ for $f \neq f_0$. This feedback thus results in applied voltage waveforms (Figure 4.5a), which now include higher frequency components, of the form:

$$V_{Applied,i}(t) = a_{f,i} \cos(2\pi(f)t + \phi_{f,i}) + a_{2f,i} \cos(2\pi(2f)t + \phi_{2f,i}) + \dots \quad (13)$$

With this method, we are able to cancel out all but the desired fundamental frequency of the traveling wave, as can be seen in both the sensor signals (Figure 4.5b) and calculated cross-section (Figure 4.5c), resulting in near-ideal traveling wave.

4.5 Camera Verification

We have also verified the traveling wave shapes independently using a high-speed microscope camera (FC13 FastVision, LLC, with microscope zoom lens: final resolution of $2 \mu\text{m}/\text{pixel}$, operated at 2,000 fps) to take synchronized sequences of images (Figure 4.6). This comparison is for a 100 Hz traveling wave, due to limitations on the camera's frame rate. To achieve $2 \mu\text{m}$ resolution, the field of view was limited to ~ 1 mm, hence, it was necessary to take separate videos at various points along the length of the sheet (8 in this case), and synchronize the videos to the applied voltage signals, in order to recreate the entire time-varying cross-section of the sheet. Simple edge-detection software was created to determine the deflection of the sheet at a given time at each location, with a precision of ~ 2 pixels, or $4 \mu\text{m}$. Reasonably good agreement is seen between the shape

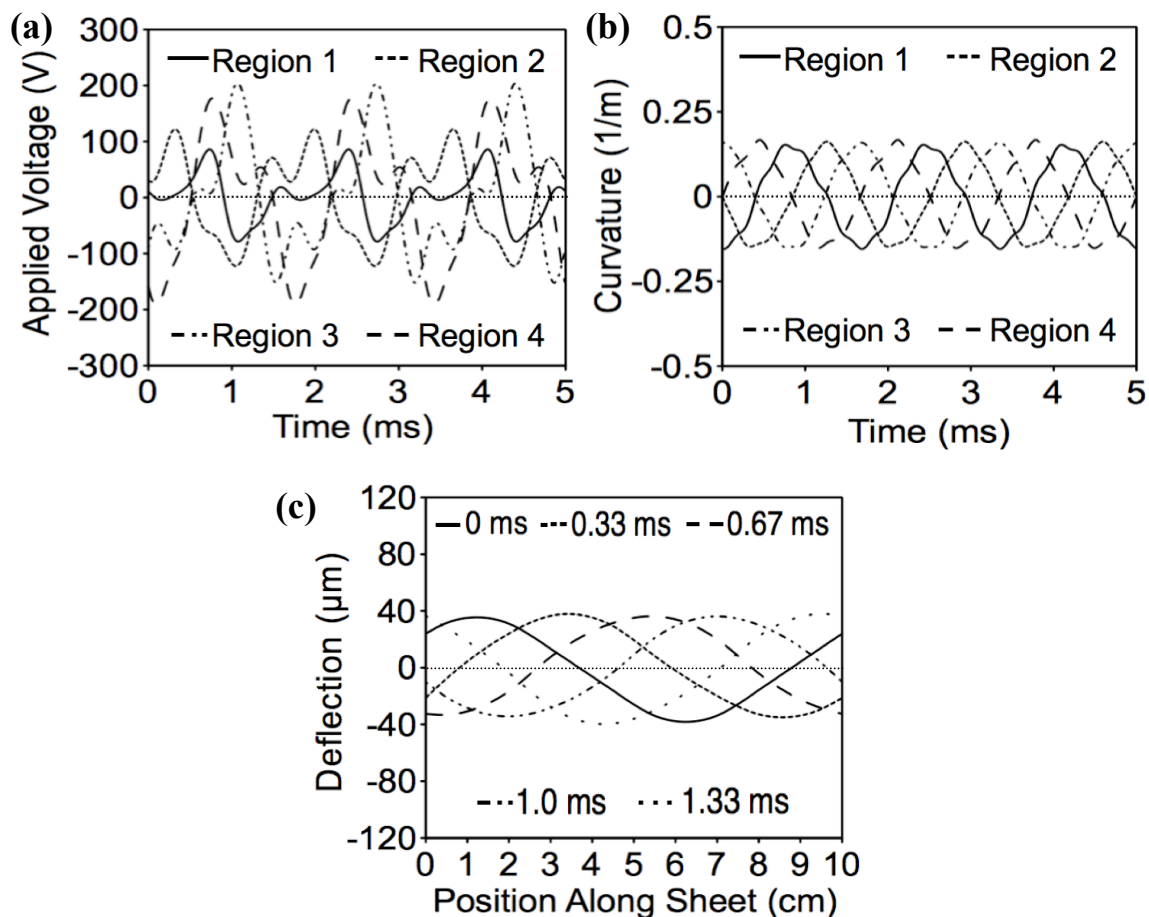


Figure 4.5 Demonstration of a traveling wave, showing the significance of sensors and feedback for achieving an ideal traveling wave shape. The applied voltage signals are adjusted using feedback on higher order harmonics up to 5 times the fundamental (600 Hz in this example), resulting in a near ideal traveling wave shape. **(a)** The voltages applied to each region of the sheet. **(b)** The average curvatures as determined from the sensor readouts. **(c)** The reconstructed shape of the sheet at various times.

seen by the camera and the shape reconstructed from the sensor signal, considering that only four sensors are used. The discrepancy can likely be attributed to the fact that the sensors are averaging the curvature over both the width of the sheet, and the length of each sensor ($1/4$ the length of the sheet). The camera, on the other hand, sees the deflection of only the edge of the sheet facing the camera.

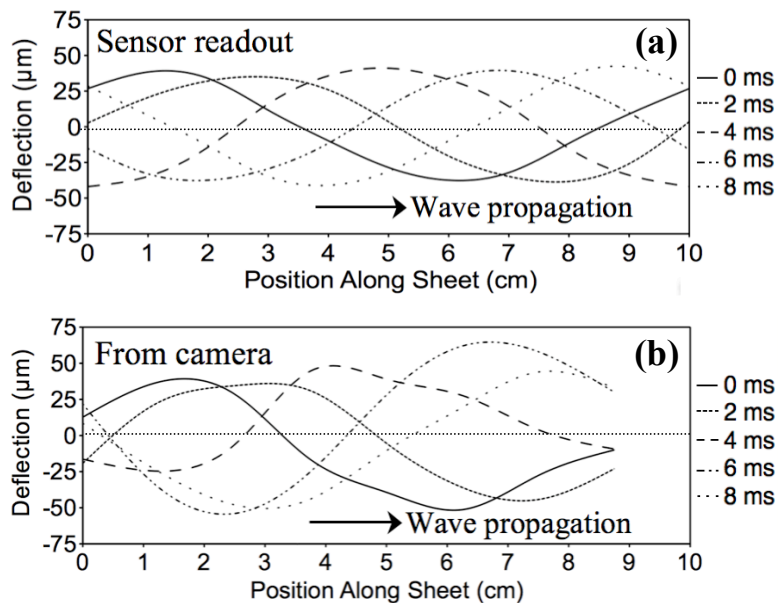


Figure 4.6 Verification of the sensor readout by using synchronized sequences of images from a high-speed camera. **(a)** Deflection as calculated from the sensor measurements. **(b)** The deflection as seen in the camera images (each image taken showed a small section of the sheet at a particular time and position along its length). Image timing is synchronized to the sheet's vibration. For these measurements, the frequency of the traveling wave is 100Hz.

Chapter 5

Propulsion

In this chapter we discuss propulsion of the sheet, using the traveling wave deformations demonstrated in the previous chapter. Section 5.1 describes how we measure the propulsive force, and Section 5.2 presents our results. In Section 5.3, we discuss what propulsive forces are theoretically expected to produce lift.

5.1 Measuring the Propulsive Force

Returning to the two arrangements used to support the sheet (Section 3.4), we see that both of them enable us to measure the intrinsic propulsive force produced by the traveling wave. This is because they provide a known external restoring force that acts against displacement of the sheet rather than velocity, so the measurement of propulsive force can be performed at zero velocity, and hence, zero drag, by measuring the steady-state displacement. In addition, we estimate the velocity by measuring the amount of time it takes for the sheet to reach the steady-state displacement.

For the first arrangement (in which the sheet hangs from three elastic threads) the setup fortuitously acts as a simple pendulum, in which the restoring force F_r due to gravity when the sheet is displaced horizontally by a distance Δx is given by $F_r \approx mg\theta \approx mg\Delta x/l$, where l is the length of the pendulum (Figure 5.1a). Thus, measurement of the

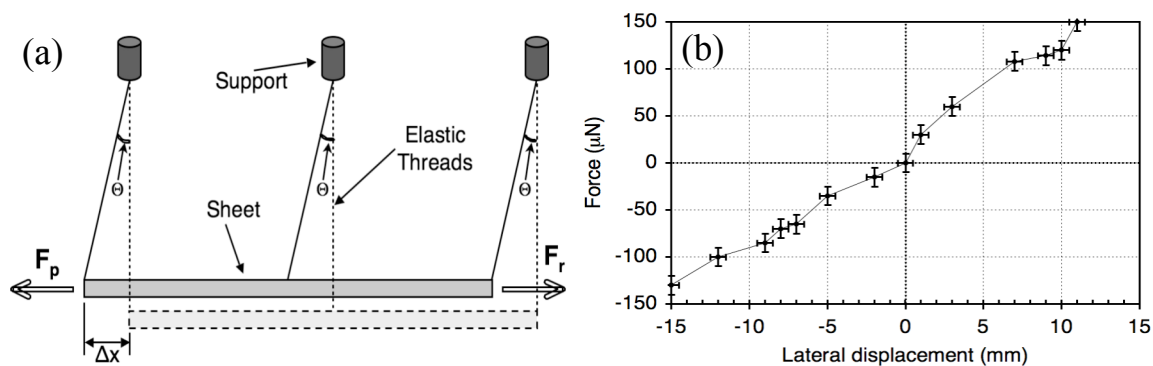


FIGURE 5.1 Restoring forces for the two experimental arrangements. **(a)** Pendulum restoring force diagram. Dashed lines indicate position of the sheet when off; solid lines when on, with wave traveling left to right. The angle, Θ , is greatly exaggerated for illustrative purposes. **(b)** Air-table restoring force as a function of sheet displacement.

displacement allows calculation of the propulsive force. Given the ~ 0.63 g mass of the sheet, 1 m suspension threads result in a restoring force constant, k , of ~ 6 $\mu\text{N}/\text{mm}$.

For the second arrangement (in which the sheet is suspended on an “air-table”) the force required to move the sheet laterally a given distance is measured directly using a force sensor (an approximately linear restoring force – k is ~ 11 $\mu\text{N}/\text{mm}$ – exists due to a combination of the electrical connections and the airflow of the air table; see Figure 5.1b). The force sensor, a thin plastic “whisker”, was calibrated by using weights to measure the force required to deflect the “whisker” by a given amount. This lateral deflection was observed visually. For both arrangements, we can measure the displacement of the sheet to within ~ 1 mm.

Experiments indicated that the first arrangement (suspension by elastic threads) resulted in the expected propulsive forces [16]. However, to alleviate any concerns that vibrations of the elastic threads could have an undesired impact on the results, the second arrangement (suspension by “air-table”) was implemented. In this arrangement, the

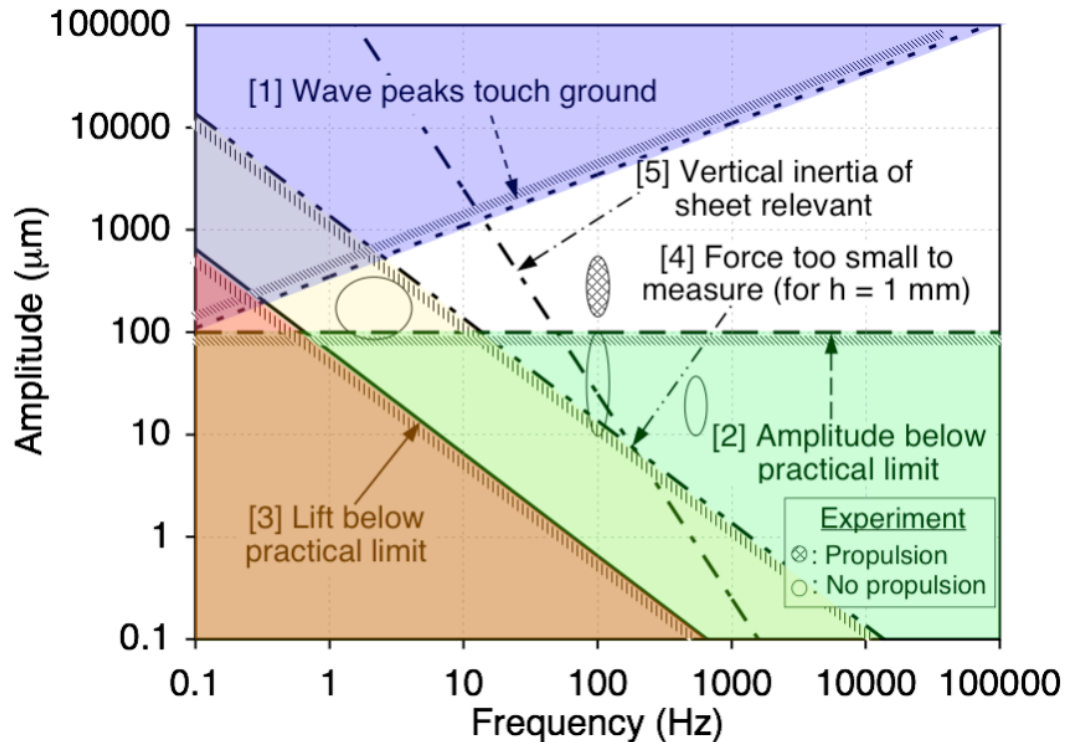


Figure 5.2 Experimental data is shown on the plot depicting different physical situations as a function of amplitude and frequency of the traveling wave, indicating the presence or absence of observed propulsive force in several amplitude & frequency regions. The shaded regions indicate the undesirable conditions. Condition 5 only weakly excludes the region to the right of the line shown.

airflow of the “air table” could have had an effect on the propulsion, however, as similar results were observed in the two arrangements, we conclude that neither the suspension threads nor the airflow produced a significant effect.

5.2 Results

With the deformations of the sheet now approximating the desired traveling waves to act as an air pump, we were able to experimentally demonstrate propulsive forces and show that they are indeed in reasonably good agreement with Equation (1) in Section 2.1

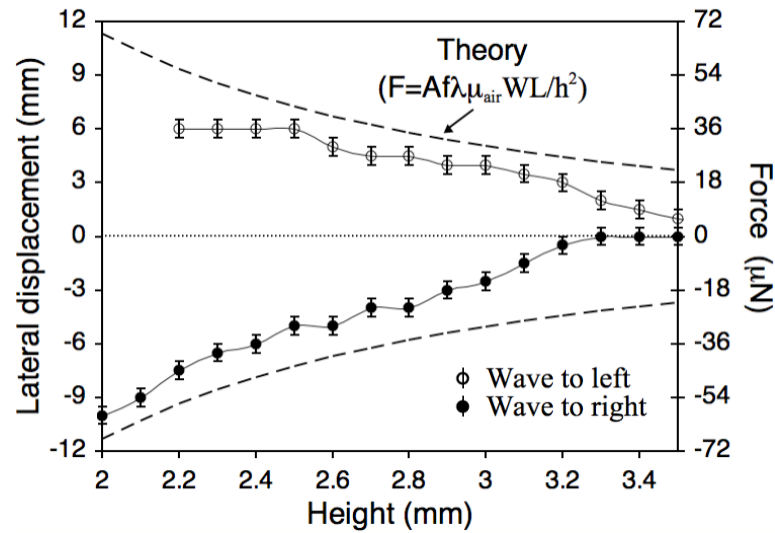


Figure 5.3 Propulsive force measurements from the pendulum arrangement, plotted versus height above the ground. The measured displacements, and calculated and predicted ($F_p = Af\lambda\mu_{air}WL/h^2$) propulsive forces, drop rapidly as the sheet is raised. Data shown is for waves at $\sim 400 \mu\text{m}$ amplitude and 100 Hz. Positive displacements correspond to motion of the sheet to the right. Note: error bars represent measurement precision.

(see Figures 5.3 – 5.5). The propulsive force reverses direction when the traveling wave direction is reversed, drops rapidly as the sheet is raised, and increases with increasing wave amplitude. The measured propulsive forces exceed $100 \mu\text{N}$ when the sheet is suspended $\sim 1 \text{ mm}$ above the ground and the deflection amplitude is above $\sim 500 \mu\text{m}$ (Figure 5.5). The sheet reached velocities of only $\sim 1 \text{ cm/s}$ due to the external restoring forces described in section 5.1. The propulsive forces were observed for traveling waves with a frequency of $f_0 = 100 \text{ Hz}$ and amplitudes of $A \approx 150 - 800 \mu\text{m}$, which falls into the expected parameter-space window (Figure 5.2). Also, as expected from Figure 5.2, for experiments conducted at $f_0 \approx 1 - 6 \text{ Hz}$ and $A \approx 100 - 400 \mu\text{m}$, $f_0 = 100 \text{ Hz}$ and $A \approx 10 - 100 \mu\text{m}$, and $f_0 = 600 \text{ Hz}$ and $A \approx 10 - 40 \mu\text{m}$, no propulsive force was observed.

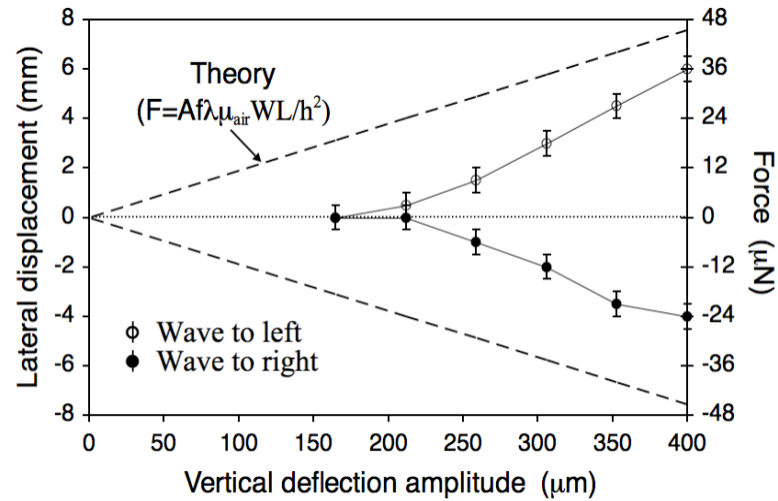


Figure 5.4 Propulsive force measurements from the pendulum arrangement, plotted versus deflection amplitude. Above some threshold, the observed displacement, and hence the propulsive force, increases linearly with deflection amplitude. Data and theory ($F_p = Af\lambda\mu_{air}WL/h^2$) are for the sheet ~ 3 mm above the ground, and vibrating at 100 Hz.

The second (right) y-axis of Figure 5.3 shows the propulsive force calculated from the displacement data, and the theory (Equation (1): $F_p \approx Af\lambda\mu_{air}WL/h^2$) is then also plotted versus the suspension height. For simplicity, we assume equality in Equation (1), which is reasonable based on the detailed simulation from Reference [3]. The sheet used is $W = 4$ cm wide and $L = 10$ cm long. The wavelength, λ , is equal to L . We observe qualitatively good agreement with this theory. The expected surface effect is quite strong, with the force dropping rapidly as the sheet is raised. Figures 5.4 and 5.5 show the displacement and propulsive force (experimental and theoretical) versus wave amplitude for both the suspension and air table experiments (for the air table, height is adjusted by varying the air pressure). Propulsive forces in excess of 100 μN are created. Both arrangements give similar results, and qualitative agreement of magnitudes and trends are again observed. Theoretically, we expect a linear dependence of force on wave amplitude

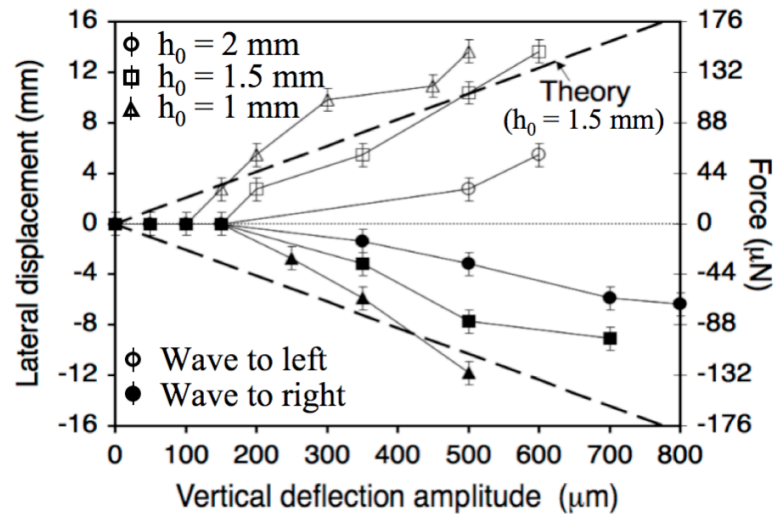


Figure 5.5 Propulsive force measurements from the “air-table” arrangement, plotted versus deflection amplitude for several heights above the ground. The displacement and propulsive force increase with amplitude and decrease with height above the ground. Data shown is for waves at 100 Hz. For this sample, the width was $W = 3$ cm. The theory plot is $F_p = Af\lambda\mu_{air}WL/h^2$.

($F_p = Af\lambda\mu_{air}WL/h^2$), but instead we observe a linear increase only after some threshold, which may be due to the fact that the sheet is not perfectly flat. Figure 5.6 is a sequence of images showing the sheet’s propulsion when on, and return to equilibrium when off, for the air-table arrangement. The entire video can be seen in Video 5.1 of the online supplemental material.

As a further proof of the aerodynamic nature of the propulsive force, we measured the velocity of the air beneath the sheet by injecting smoke at one end of the sheet, and measuring the time until it exits the other end (without a traveling wave, the smoke simply rises). With the sheet bending in a traveling wave, the smoke flows under the sheet at a speed of at least 5 cm/sec (at conditions corresponding to the maximum displacement shown in Figure 5.3), in the same direction as the wave, as expected. A video of this experiment can be seen in Video 5.2 of the online supplemental material.

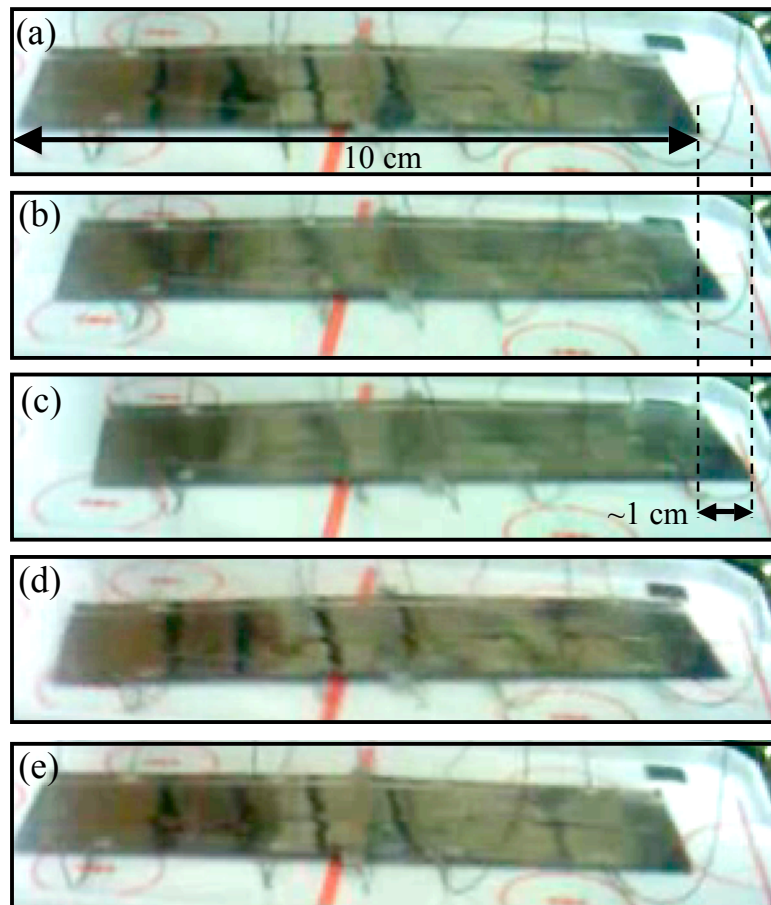


Figure 5.6 Time sequence of actual sheet propulsion. **(a)** The sheet is off and in equilibrium. **(b)** After the sheet has been on, with the wave traveling to the left, for 0.6 sec. Note that while the sheet is on, reflections off of its surface are blurred due to the 100Hz vibration. **(c)** After the sheet has been on for 1.2 sec. Total distance traveled is about 1.2 cm. **(d)** After the sheet has been off again for 0.6sec. The sheet begins to return to its equilibrium position due to the restoring forces provided by the electrical connections and the air table's airflow. **(e)** After 1.2 sec, the sheet has returned to near its equilibrium position.

5.3 Force Required for Lift

To determine whether the forces we have measured are in the range needed, theoretically, to produce lift if the sheet were free to accelerate, recall that the theoretical lift force (assuming low Reynolds number) is given by $F_{lift} = \nu \mu_{air} W L^2 / h^2$ (derived

from reference [3]). Therefore, in order for lift to occur (i.e. $h >$ wave amplitude, A , when $F_{lift} = mg$), we need:

$$v > mgA^2/\mu_{air} WL^2. \quad (14)$$

This is ~ 23 cm/s for a $500 \mu\text{m}$ wave amplitude (and $W = 4$ cm, $L = 10$ cm, and $m = 0.63$ g). To achieve this velocity, we need a propulsive force large enough to equal the drag force ($v \mu_{air} WL / h$) at that speed (and we assume h is still equal to A). Plugging in the expression from Equation (14) gives:

$$F_p > mgA/L, \quad (15)$$

or $\sim 30 \mu\text{N}$ for a $500 \mu\text{m}$ wave amplitude. Our measurements are considerably above this value ($\sim 150 \mu\text{N}$ for a $500 \mu\text{m}$ wave amplitude, even when 1 mm above the ground), hence the theory indicates that lift would result, provided that the sheet can be freed from its tethers so it can reach the necessary speeds.

Chapter 6

Power Considerations

In this chapter we discuss power usage, which is important for considering on-board power. Section 6.1 explains expected power losses, and Section 6.2 presents the sheet's measured power consumption. In Section 6.3, we describe preliminary work on providing on-board power using a boost-converter circuit.

6.1 Theoretical Power Losses

The aerodynamic propulsive force that we have demonstrated is theoretically sufficient to achieve “flying” of the sheet, provided that it can be freed from its tethers, allowing it reach high enough speeds to produce lift (see Section 5.3). To achieve a truly free sheet, it will be necessary to supply on-board power (discussed further in Section 6.3; an alternative method for demonstrating lift is discussed in Section 7.3). Therefore in this section we discuss the electrical power fundamentally required for this system.

We break down the power consumption of the device as follows:

(1) Given the propulsive forces we have measured, the intrinsic power needed to propel the sheet at the steady-state velocity of ~ 20 cm/s predicted for such a propulsive force is $P_I \sim F_p * v \sim 100 \mu\text{N} * 20 \text{ cm/s} = 2 * 10^{-5} \text{ W}$ (note, however, that our current experiments

only reach ~ 1 cm/s due to the external connections, so only ~ 1 μ W is needed in that case).

(2) The electrical power consumed by the actuators has been directly measured to be less than 10 mW (see Section 6.2), when vibrated using the same voltage amplitude and frequency as under an actuation condition predicted to produce such a velocity, but with the same voltages applied to all four actuators for ease of measurement (see Section 6.2).

(3) The efficiency of PVDF at converting electrical to mechanical energy can be calculated from its material properties (piezoelectric coefficient, dielectric constant, and Young's modulus) using the following equation for the maximum energy transmission coefficient, λ_{max} , for a bilayer structure [41]:

$$\lambda_{max} = \frac{32}{9k_{31}^2} \left(\sqrt{1 - k_{31}^2/4} - \sqrt{1 - 13k_{31}^2/16} \right)^2, \quad (14)$$

where k_{31} is the electro-mechanical coupling coefficient. This is given by $k_{31}^2 = d_{31}^2 Y / \epsilon_{33}^X$, where ϵ_{33}^X is dielectric permittivity. For PVDF ($k_{31} \approx 0.1$), this gives $\lambda_{max} \approx 0.3\%$ (note that other piezoelectrics can be considerably more efficient, for example $k_{31} \approx 0.4$ for PZT, which results in $\lambda_{max} \approx 5\%$). For an input electrical power of 10 mW, this implies that at most $\sim 3 \cdot 10^{-5}$ W are available for mechanical motion, which, to first order, agrees with the intrinsic power needed to propel the sheet at full speed.

(4) The discrepancy is likely due to the energy that is lost in the interaction between the vibrating sheet and the surrounding air. The efficiency of this process has not been determined for our experiment. Note that the discrepancy could be larger – i.e. a smaller percent of power transmitted, and thus a lower efficiency for the mechanical energy to fluid energy process – if the power consumed during propulsion is greater than in the test setup.

6.2 Measured Power Consumption

Although the required voltages and currents for our system are rather high (up to 400 V and 4 mA), the average power consumption is quite low (less than 10 mW; Figure 6.1) due to the capacitive nature of the piezoelectric. The power used is determined by averaging the product of the applied voltage and current, measured as a function of time. For this measurement, the amplitude of the applied voltage was 200 V, and the same signal (at 100 Hz) was applied to each of the four actuators to allow easier measurement of the current: The current is determined by measuring the voltage across a small resistor ($\sim 100 \Omega$) placed between the electrical ground and the sheet's ground plane. Since all four actuators share this ground plane, only the total current is measured. Future work is needed to measure the power when the applied voltage signals are those needed for actual propulsion – this will require either making separate ground connections for each actuator or measuring the instantaneous current between each applied voltage signal and actuator (using inductive current probes, for example, provided that they can detect the current at frequencies down to 100 Hz and below 1 mA).

The majority of the consumed power (“Total Power” in Figure 6.1) is actually consumed in the resistive contacts to the sheet (note that the power consumed in the external resistor used for current measurement has already been accounted for), i.e. the conductive threads and glue (“Resistor Power” in Figure 6.1) – once this effect is removed, it can be seen that the power consumption of the sheet alone (“Sheet Power” in Figure 6.1) is less than 10 mW for frequencies less than a few hundred Hz. Note that we are neglecting here the power lost in the driving circuit, as it is yet to be optimized. For the op-amp circuit used in these experiments (described in Section 3.2), the sheet, which

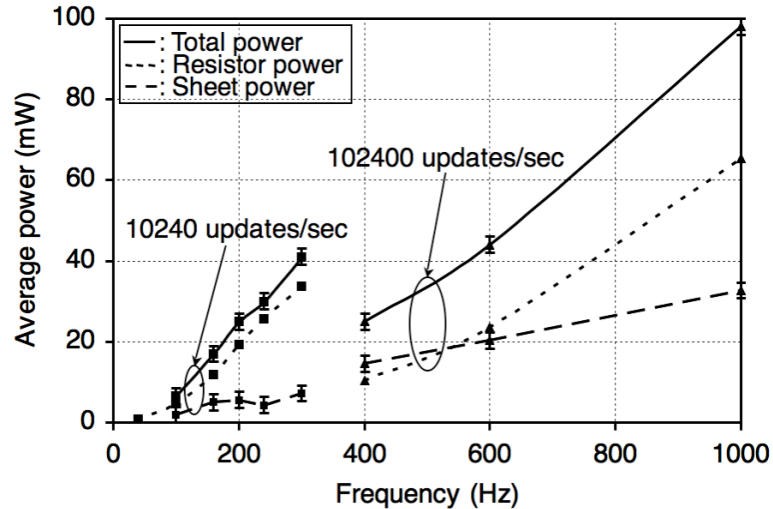


Figure 6.1 Average power consumption of the sheet. Two sets of measurements are shown – one with the applied voltage updated at 10240 times/sec, and one with 102400 times/sec. After the power lost in the resistive contacts ($\sim 250 \Omega$ in this case) is removed, both measurements give similar average power consumption by the sheet itself.

acts as a capacitor, must be charged twice every cycle (i.e. from zero to V , and then from zero to $-V$, where V is the applied voltage amplitude), leading to a power loss of $\sim 0.5 C V^2 * 2f \approx 80 \text{ mW}$ for a 200 V amplitude, 100 Hz signal ($C \approx 20 \text{ nF}$ for all four actuators together). Using resonant driving circuits that store the energy (from discharging the capacitor) in an inductor could reduce this power loss, provided that we are only interested in a fixed frequency. Two sets of measurements are shown – one with the applied voltage updated at 10240 updates/s, and one with 102400 updates/s. Since a higher number of updates/s implies that each step in applied voltage must be smaller (for a given attempted voltage waveform), and the current is actually a series of spikes at each voltage step (since the RC time constant, which is a few μs , is small compared to the update period of 10 or 100 μs), the power consumed in each step in the resistive connections (which are in series with the capacitive PVDF sheet) would be expected to

be ~ 100 times smaller when the update rate is 10 times greater, so the average power consumed in the resistor would be ~ 10 times smaller. Of course, this assumes that the current decays completely before the next voltage step, which is not exactly valid for the 102400 updates/s case. Hence, while we do in fact see a smaller “resistor power” for the 102400 updates/s case, it is ~ 5 to 8 times smaller than the 10240 updates/s case, rather than 10 times. This does tell us, though, that we can reduce the actual power consumption by decreasing the update period towards the RC time constant.

In summary, the minimum fundamental electrical power that has to be supplied to the current system is on the order of 10-20 mW for vibrations up to 600 Hz. This would determine the absolute minimum requirement for an on-board power supply (e.g. battery or supercapacitor). Resistor losses and driving circuit inefficiencies in powering a largely capacitive load increase this requirement.

6.3 On-board Power

To provide onboard power, a circuit must be designed that can produce an output of at least 400 V p-p and 100 Hz, with a capacitive load of up to ~ 35 nF. In addition, we need to be able to vary the amplitude, phase, and frequency of the signal. This needs to be done using components as light as possible, considering that the weight of the sheet is only ~ 1.1 g (for this section, the size of the sheet has been increased to 4 cm x 16 cm to accommodate $\sim 50\%$ greater weight for the power supply).

6.3.1 DC Amplification Simulations

For simplicity, and as a proof-of-principle demonstration, a basic boost-converter circuit was used. To understand how such a circuit operates, consider the simulation shown in Figure 6.2. Part (a) shows the basic circuit: A pulse-width-modulated (PWM) signal, V_{sl} , is used to switch an inductor from being shorted to ground to being connected to a capacitive load. A diode is placed between the inductor and the capacitor to prevent discharging when the inductor is shorted to ground. The component values used are typical of those used in the actual circuit, as described below. Note that an “ideal” switch, with fixed on and off resistances, is used in the simulation, whereas a MOSFET is used in the actual circuit (Section 6.3.3). However, the switching time of the actual MOSFET is rated at ~ 5 ns, which is small enough for this to be a reasonable approximation given the response times of this circuit (~ 2 μ s to ~ 40 μ s in Figure 6.2b). In Figure 6.2b, we show an example of a few charging cycles – most of the time, the switch is closed, shorting the inductor to ground and allowing the current through to build up. Once the current has reached a maximum (equal to the DC input voltage divided by the series resistances in the circuit – 15 V / 95 Ω in this case), the switch is closed briefly, which increases the charge stored on the load capacitor as the current quickly drops to zero. The diode prevents the current from swinging negative. As this cycle is repeated, the voltage on the capacitor steadily increases, reaching hundreds of volts after a few ms (Figure 6.2c). Somewhat higher voltages (~ 500 V instead of ~ 400 V in 4 ms) can be achieved if the switch is kept closed for a slightly shorter time, as the current is already close to maximum before the switch is opened in the simulation shown in Figure 6.2.

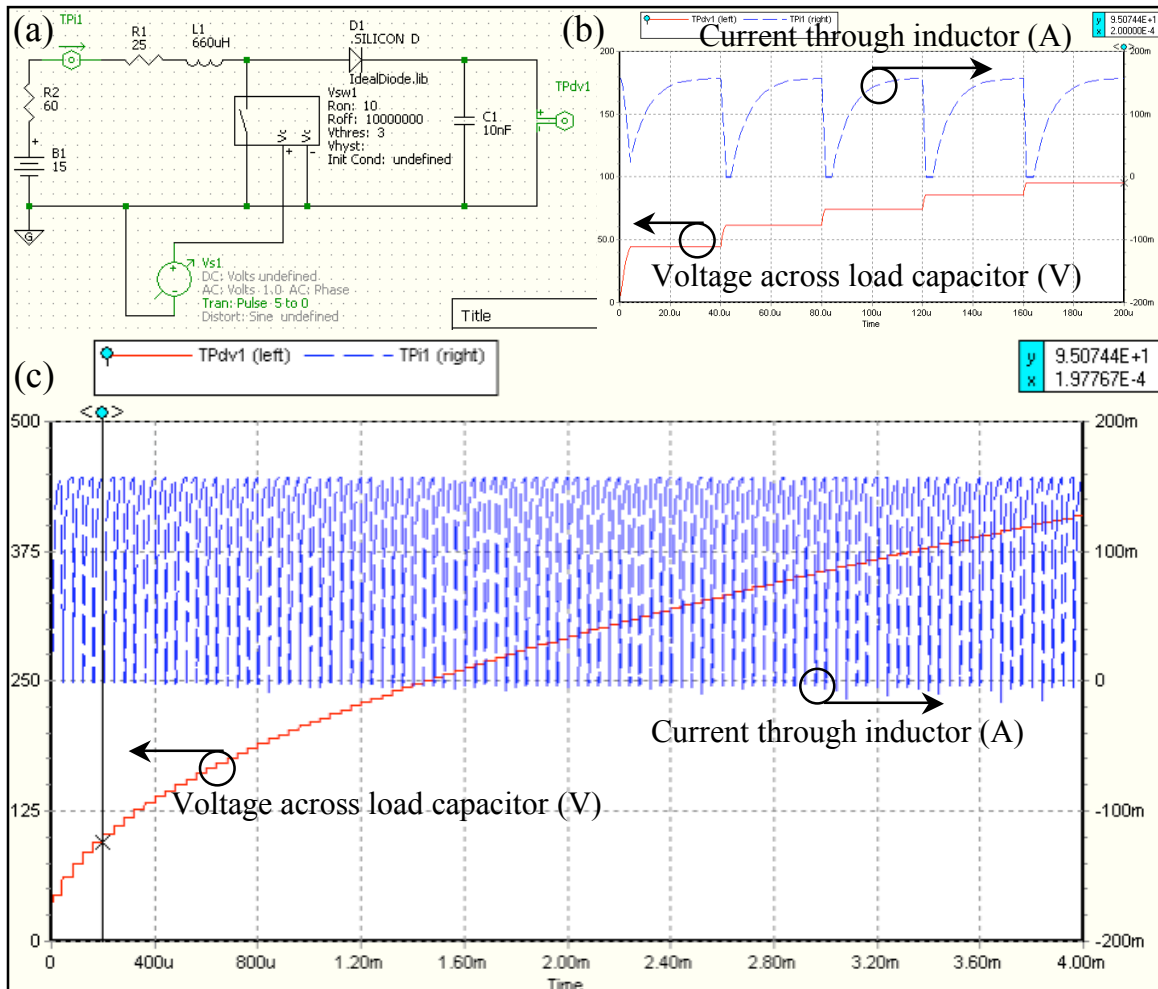


Figure 6.2 (a) A basic boost-converter circuit. Realistic series resistances for available components are included. (b) Simulation result for a few charging cycles. (c) Charging the capacitor to a high DC voltage in a few ms.

6.3.2 AC Amplification Simulations

For our application, we need an AC signal, rather than DC, and we would like to be able to freely choose the frequency. A simple, though inefficient, way to achieve this is shown in Figure 6.3. The main part of the circuit (Figure 6.3a) is the same as in Figure 6.2a, except that a capacitor is used as the DC input power supply, as the real circuit uses (Section 6.3.3). This input capacitor is initially charged to 15 V, and a switch is used to

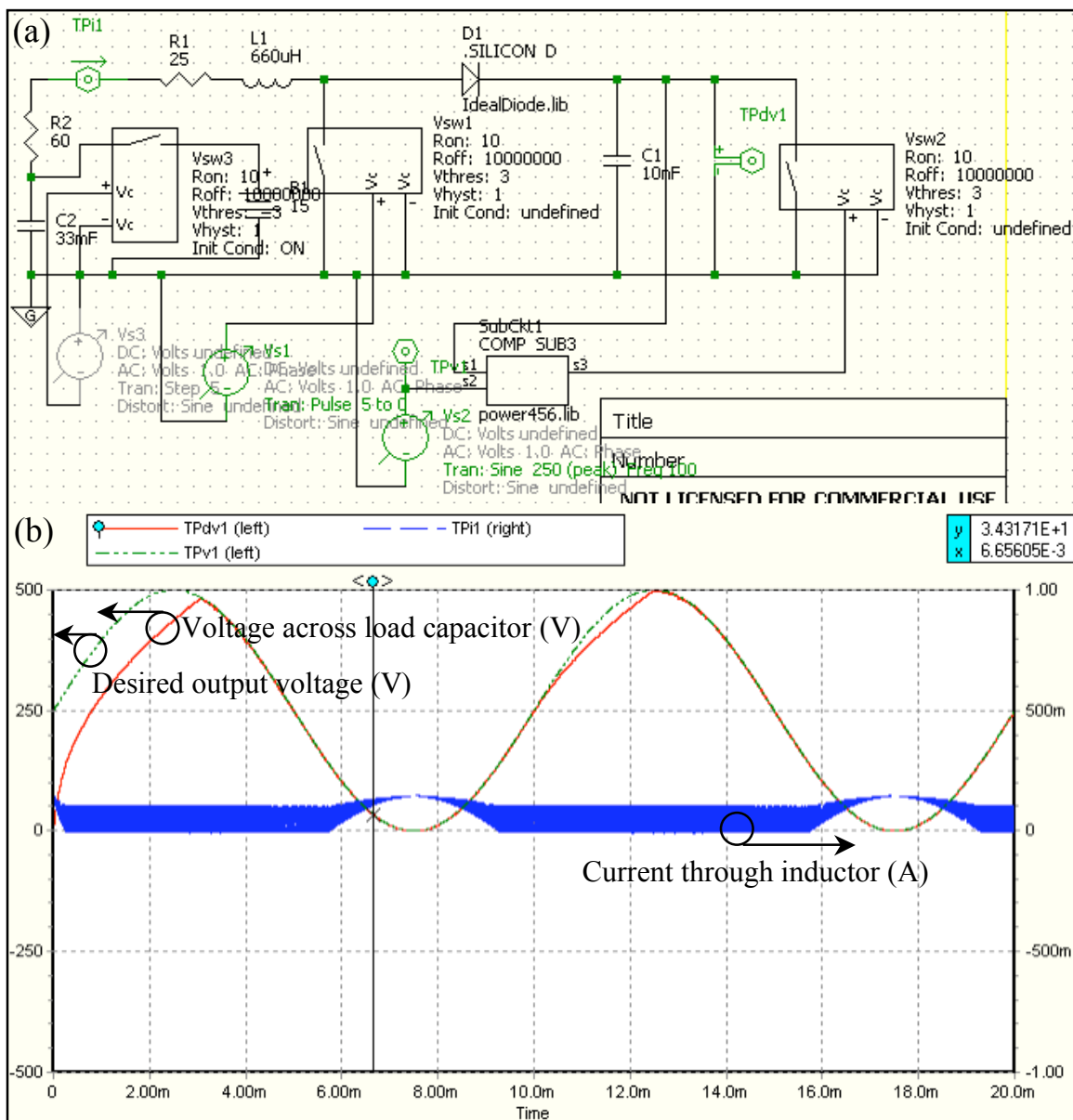


Figure 6.3 (a) A boost-converter circuit with feedback. This model includes a capacitor as the DC input, as would be used in the actual circuit. **(b)** Simulation result when 100 Hz, 0-500 V output signal is attempted.

disconnect this external power supply at the start of the simulation. To achieve an AC output signal, the load capacitor is simply shorted out whenever the voltage across it becomes larger than the desired signal. The simulation result shown in Figure 6.3b indicates that a 0-500 V output should be possible, even up to 100 Hz. The charging

current is less than ~ 100 mA, which is the limit for some of the components used in the actual circuit (Section 6.3.3).

6.3.3 Experimental Circuit Implementation

The actual circuit implementation used is shown in Figure 6.4a. There are two differences from the circuit used in the simulations of Figure 6.3, besides the use of high-voltage MOSFETs as switches: (1) A voltage divider is used to measure the output voltage, v_{out} , so that it can be compared with the low-voltage “desired” signal, $v_{desired}$ (which is 100 times smaller). (2) To avoid requiring a second signal, v_1 , the PWM signal, is simply modulated by the desired waveform, and then passed through an RC filter to produce $v_{desired}$. This is possible because small variations in the duty cycle of v_1 do not have much effect on the boost converter’s amplification. Running at DC (i.e. without the feedback part), this circuit was able to charge a 40 nF capacitor (similar to the capacitance of all four PVDF actuators together) up to ~ 30 times the input voltage (~ 8 V). When feedback is used to short out the PVDF when the voltage is higher than desired, this circuit was able to run up to 100 Hz without losing significant amplitude. An example with a 7 V DC input, attempting to produce a 100 Hz, 0 to 200 V output, is shown in Figure 6.4b. For actual operation on the sheet, the DC input must be provided by an on-board power source. Since the current it needs to supply is rather high at ~ 100 mA, thin-film super capacitors were used rather than batteries. Some flexible supercapacitors (from OptiXtal, for ex.) have an energy density of ~ 4 mJ/mg, which means that 1 gram’s worth of such supercapacitors could in principle power the system for several minutes (i.e. if only ~ 10 mW needs to be supplied, as discussed in Section

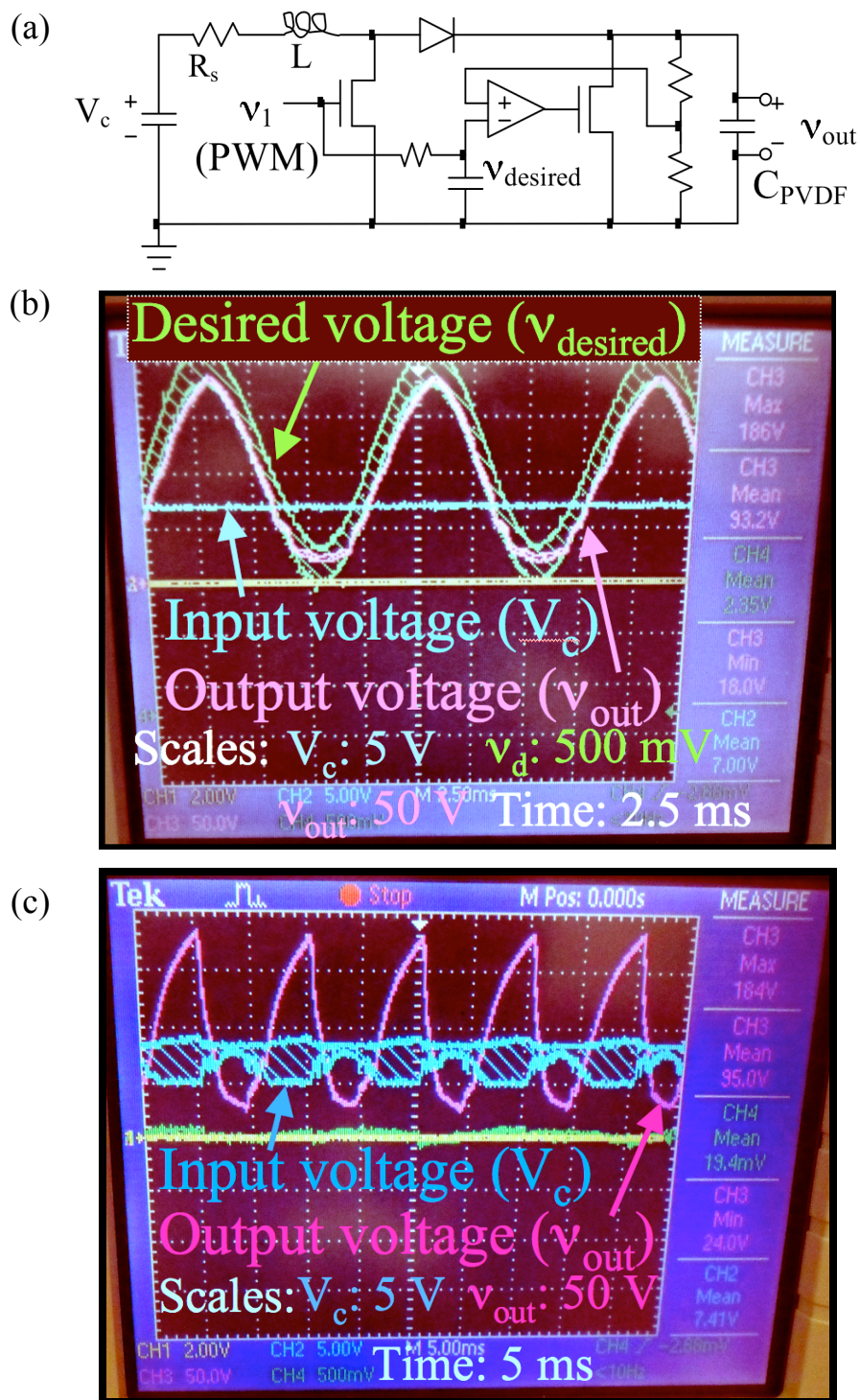


Figure 6.4 (a) Circuit diagram for a boost-converter circuit with feedback. (b) Oscilloscope measurement of the boost-converter in action, with a fixed DC input of 7 V. (c) The input voltage now comes from 4 supercapacitors in series (each initially charged to ~ 2 V).

6.2). These supercapacitors from OptiXtal weigh ~ 80 mg, have a capacitance of ~ 0.2 F, and a series resistance of ~ 10 Ω . Each supercapacitor can be charged to a maximum of ~ 2.7 V – for this measurement, 4 are connected in series and charged to ~ 8 V total. The result is shown in Figure 6.4c – a 100 Hz signal close to 200 V p-p is still achieved, but it is not able to follow the desired sine wave as closely. The input voltage is measured directly across the four supercapacitors, but due to their internal resistance (~ 40 Ω for four) this voltage drops significantly when the current (up to ~ 100 mA) flows. As mentioned above, this circuit wastes power because the PVDF needs to be recharged every cycle (i.e. from zero to its peak-to-peak value). This means that power required would actually be $\sim 0.5 C V^2 f \approx 280$ mW for a 400 V p-p, 100 Hz signal (C is the total capacitance of all four actuators; ~ 35 nF for the 4 cm x 16 cm sheet). Thus, the supercapacitors last for seconds, rather than minutes. Nevertheless, with six supercapacitors for a 15 V DC input, a 100 Hz, 400 V p-p output is expected. The weight of this circuit is broken down as follows: 1 inductor (660 μ H, 26 Ω) = 100 mg, 1 diode = 65 mg, 2 MOSFETs (400 V, ~ 10 Ω at $V_g=5$ V) = 80 mg each, 1 comparator = 6 mg, 3 resistors = ~ 14 mg total, 1 capacitor (22 nF) = 50 mg, and 6 supercapacitors (0.2 F, 2.7 V, ~ 10 Ω) = 80 mg each. The components are connected together by 100 μ m wires only (no substrate is used), so this adds only a few mg. The total weight is thus ~ 395 mg per actuator, plus ~ 480 mg for the supercapacitors (to be shared by all four actuators). Further work is needed to extend the time that this power supply can last, as a few seconds is a bit short, even for demonstration purposes. One way to do this is to simply add a few more supercapacitors – this should increase the maximum output voltage, or alternatively, increase the time until the output drops below an acceptable value.

6.3.4 IR-LED Control Signals

To provide control, the PWM signals are sent using infrared light emitting diode (IR-LED) communication. A comparator circuit produces a digital signal by comparing the signal received by a photodiode to a background level (Figure 6.5a). This level is set by charging a supercapacitor to the necessary voltage, which is ~ 0.2 V in the example shown in Figure 6.5b. The resulting digital signal is thus independent of the distance between the signal source (IR-LED) and the photodiode (at least for distances for which the initial signal can still be detected), and reproduces the original PWM signal sent by the IR-LED (Figure 6.5b). Currently, the signal can be detected from a couple of inches away, but the angle of the LED's beam spread is $\pm 60^\circ$, so collimating optics should enable signal detection from much greater distances. Supercapacitors are used to reverse bias the photodiode and power the comparator – two will be needed to allow outputs of 0-5 V (which is necessary for driving the MOSFET gate in the boost-converter circuit), although currently only 0-2 V has been demonstrated (Figure 6.5b). Four different wavelength emitters and filtered detectors would be used to allow each actuator signal to be distinguished from the others. The weights of the components used for this signal detection circuit are: 1 comparator = 6 mg, 1 photodiode = 43 mg, 1 resistor = 5 mg, and 3 supercapacitors = 80 mg each. The weight of the filters could be minimal, especially if they are coated directly on the photodiodes. This gives a total of ~ 54 mg per actuator, and ~ 240 mg for the supercapacitors (to be shared by all four actuators).

Putting together the boost-converter circuit and the photo detector circuit will require increasing the output voltage of the comparator to 5 V, as mentioned above, and result in a total weight of ~ 450 mg per actuator for the circuitry and ~ 720 mg for the

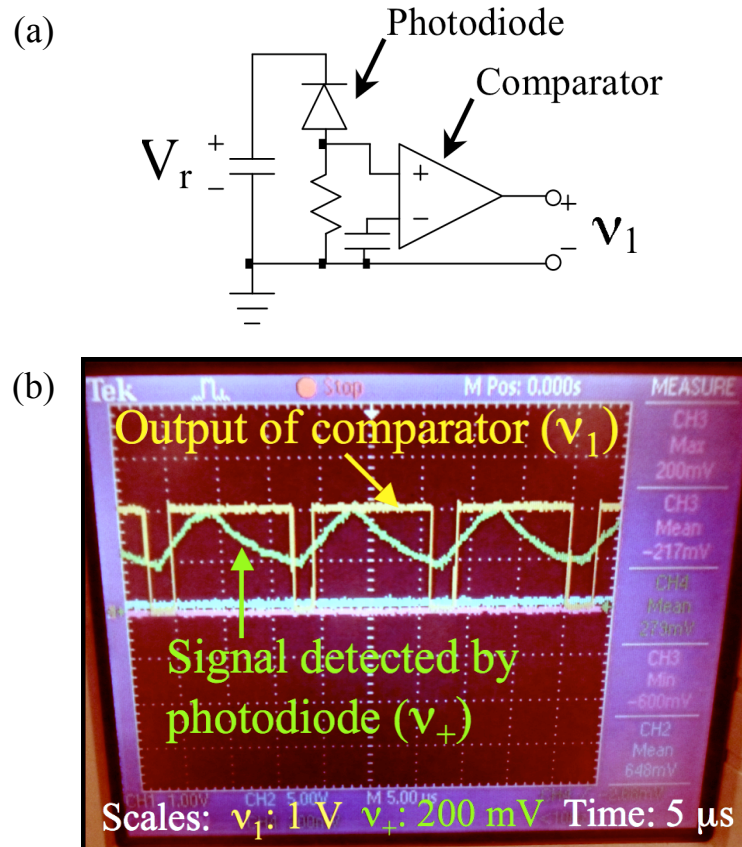


FIGURE 6.5 (a) Circuit diagram for IR-LED signal detection. (b) Oscilloscope measurement of detector in action.

supercapacitor power supplies. Since we have four actuators, this results in ~ 2.5 grams, which is a bit more than the weight of the sheet (~ 1.1 g), but might be just tolerable, depending on what speed can be achieved. Further weight reduction should be feasible by using unpackaged components, as that can be a significant fraction of the weight.

Chapter 7

Practical Considerations and Experiments for Realizing Lift

As discussed in Chapter 2, the predicted lift force for a freely moving sheet at low Reynolds number near a boundary is given by $F_{lift} = \nu \mu_{air} W L^2 / h^2$ (derived from Reference [3]). In the experiments described so far, the sheet was tethered, and thus moved only up to ~ 1 cm/s, which was not sufficient to produce a lift force greater than gravity. As discussed in Section 5.3, a speed of ~ 20 cm/s is expected to be necessary (assuming 500 μm wave amplitude, $W = 4$ cm, and $L = 10$ cm); for $\nu = 1$ cm/s, F_{lift} is at most ~ 0.3 mN (i.e. when $h=A$), which is considerably less than the force of gravity ($mg \approx 6$ mN for a 0.63 g sheet). Hence, we need a way to allow the sheet to reach higher velocities in order to demonstrate lift.

In this chapter, we first discuss how to overcome friction to allow the sheet to start moving, in Section 7.1. Section 7.2 discusses lift with passive test samples as a means to estimate where we need to be with the actual sheet. Section 7.3 discusses the use of a small “cart” to follow the sheet as a potential method to demonstrate lift by allowing the sheet to move freely without requiring on-board power.

7.1 Friction & Static Electricity

7.1.1 Reducing Friction

Without external lift, the sheet is initially at rest on the ground. Hence, in order to start moving, the sheet needs to overcome friction. With a mass of 1.1 g (for all experiments discussed in this chapter, the size of the sheet has been increased to 4 cm x 16 cm), typical coefficients of friction ($\sim 0.2-0.8$) for the sheet result in forces of $\sim 2-8$ mN, considerably greater than our propulsive forces (~ 150 μ N for the tethered, 0.63 g, sheet). Additionally, if it is lying directly on the ground, there is not already a gap beneath the sheet for the air to be pumped through, and it might have difficulty starting even with reduced friction. For this reason, tiny supports were affixed to the under side of the sheet (Figure 7.1). Several kinds of supports have been tested, from Teflon “skis” to glass beads, and are described below. The supports all have heights in the $\sim 300-800$ μ m range, smaller than the expected lift height. To minimize sagging of the sheet between supports, the spacing between supports was made to be 2 cm, resulting in a total of 27 supports for the 4 cm x 16 cm sheet. Affixing the supports to the ground was attempted as well, however, this resulted in a time-varying external force distribution that the present control system was unable to handle. However, even with these supports, we still need to reduce the friction, and one way to do this is by constructing a “launch pad” from low-friction materials, such as Teflon (PTFE).

7.1.2 Effects of Static Electricity and Pressure-Dependence

Care must still be taken to eliminate other effects, such as static electricity and load-dependent friction. For example, Teflon tape can have a very high static charge when

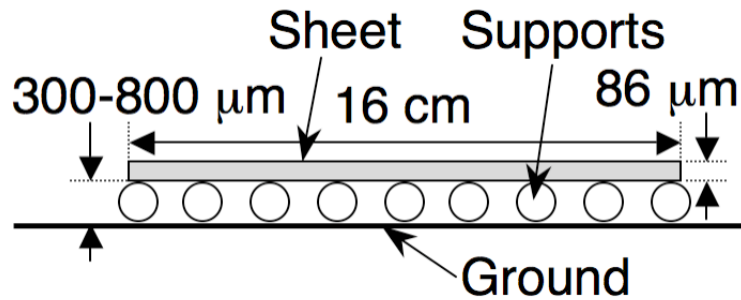


Figure 7.1 Illustration of tiny supports under the sheet.

initially unrolled – so high, in fact, that the sheet was pulled down to the ground between the supports, and stuck to the surface. Measurements of the force required to bend the sheet that much showed that the static attraction force was ~ 100 times the force of gravity on the sheet. However, by spraying the surface with an anti-static spray (ACL Staticide) this attractive force was greatly reduced (i.e. no visible deflection of the sheet). An attractive force more than 10 times that of gravity would be needed before visible deflection of the sheet would occur (determined empirically by placing weights on the sheet until “visible”, or $\sim 50\text{-}100\ \mu\text{m}$, deflection occurred), hence, there may still be a considerable effect (see discussion below). Also, Teflon, in particular, achieves its quoted ~ 0.05 frictional coefficient only at loads above $\sim 10^6\ \text{N/m}^2$, and has higher coefficients at lower loads.

To determine the effect of static electricity and load-dependence, the frictional coefficient was measured with different weights placed on the sheet (Figure 7.2). For the measurements shown in Figure 7.2, the sheet was supported on 27 tiny “skis”, or wedge-shaped pieces ($\sim 800\ \mu\text{m}$ high and $\sim 1\ \text{mm}$ long), made out of Teflon. To measure the coefficient of friction, the piece of plastic on which the sheet rests is tilted until the sheet begins to slide. If no static electricity is present, the coefficient of friction, C_f , can be

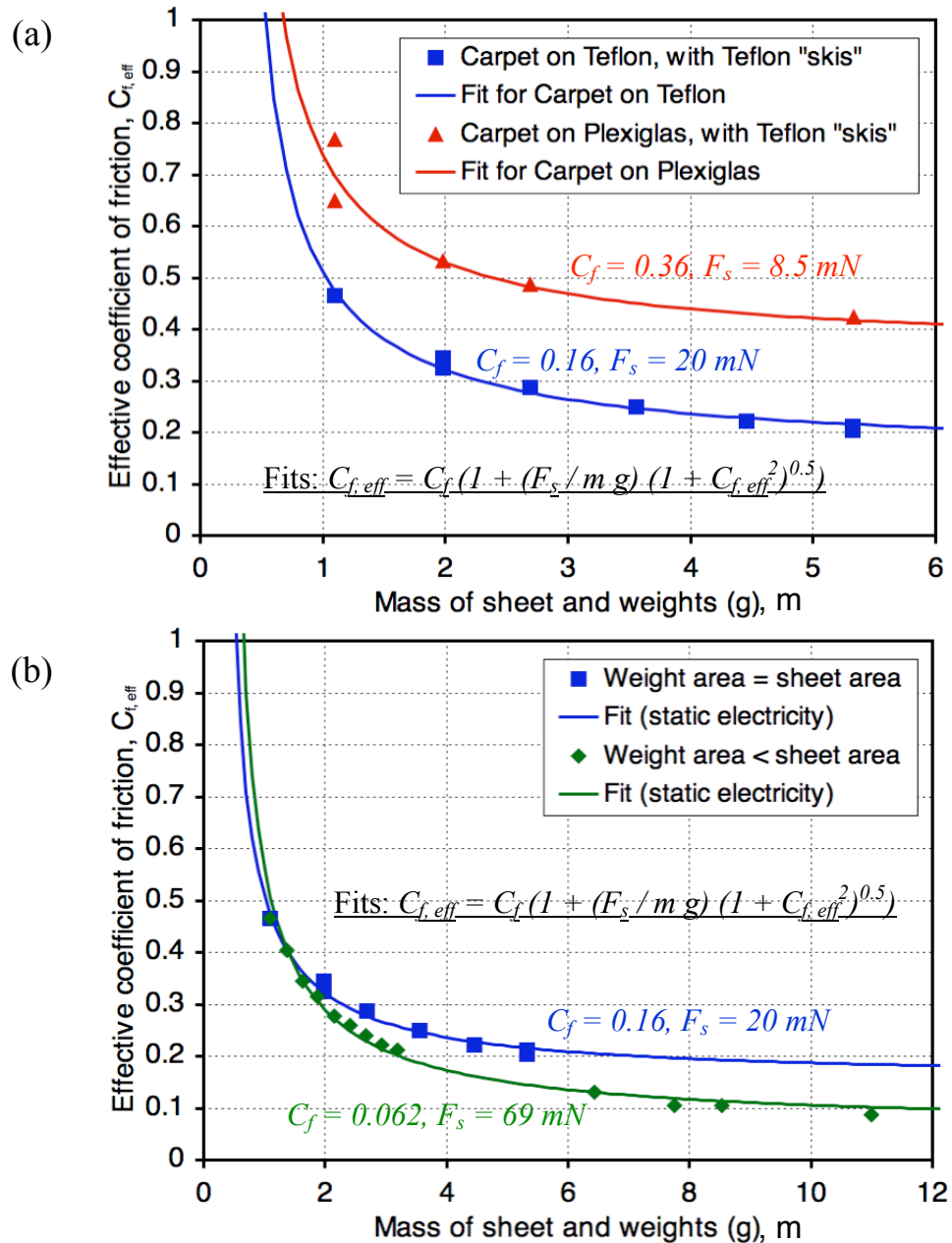


Figure 7.2 (a) The effective coefficient of friction drops with increasing mass, and is smaller on Teflon than on Plexiglas (both treated with anti-static spray), as expected. Note that the 1.1 g data points correspond to the sheet itself, with no additional weight. **(b)** Two sets of data are compared (both on Teflon) – one for which the area of the weights is equal to that of sheet (same as the data shown in part (a)), and the other for which the area of the weights is considerably smaller. All of the fits assume that static electricity is the only cause of the mass-dependence, and are thus not fully accurate, as explained in the text.

found from the relation: $C_f m g \cos \theta_s = m g \sin \theta_s$, or $C_f = \tan \theta_s$, where θ_s is the angle at which the sheet begins to slide. We shall consider this to be the “effective” coefficient of friction, even in the presence of other normal forces, like static electricity. Ideally, we would expect this tilt angle, and thus coefficient of friction, to be independent of the mass of the sheet, however this is not the case, as seen in Figure 7.2. Consider first the effect of static electricity – this will add an additional force that is always normal to the surface, regardless of the tilt angle. Hence, the force balance equation becomes $C_f (m g \cos \theta_s + F_s) = m g \sin \theta_s$, where F_s is the static electricity attractive force (which is proportional to area, but we keep the area fixed as the mass is changed). Plugging in $C_{f, eff} \equiv \tan \theta_s$ gives $C_{f, eff} = C_f (1 + (F_s / m g) (1 + C_{f, eff}^2)^{0.5})$. We can plot this expression as a fit to the data (Figure 7.2a), with C_f and F_s as fitting parameters. Reasonably good agreement is seen, with values of $C_f \approx 0.16$ and $F_s \approx 20$ mN (or about twice the force of gravity on the bare sheet) when the sheet is sliding on Teflon tape, and $C_f \approx 0.36$ and $F_s \approx 8.5$ mN when the sheet is sliding on Plexiglas. On the other hand, to see if pressure-dependence is contributing to the change of $C_{f, eff}$ with mass, we place weights of a smaller area (7.5 cm by 2.5 cm) on the sheet – this produces a greater pressure on the supports under the weights, for the same mass (and the sheet’s area is unchanged, so the static electric force should be unchanged as well). Figure 7.2b shows a comparison between using these smaller-area weights, and weights of the same area as the sheet. These measurements are for the sheet sliding on Teflon tape, with Teflon “skis”. The sample with the smaller-area weights shows a greater reduction of friction as the mass increases, which indicates that pressure-dependence of the frictional coefficient is also present. The area of the smaller weights is $\sim 30\%$ of the sheet’s area, but it sits over only ~ 5 of the 27 supports, so the

pressure on these supports may be up to ~5 times greater than if the same mass weight was spread over the entire sheet. If pressure-dependent friction is the only effect present, and all of the extra weight is carried on the 5 supports, with the remaining 22 supports carrying only the weight of the sheet (which is plausible, considering the flexibility of the sheet), we would expect that the frictional coefficient could be reduced by at most ~20% compared with the bare sheet (i.e. if the friction went to zero for the 5 supports with extra loading). The data in Figure 7.2b, however, show a drop by about a factor of 5. This is a strong indication that both static electricity and pressure-dependent friction are present in these experiments. Further work is needed to verify this – for example, it is possible that when the small-area weights are placed on the sheet, the supports not under the weights somehow lose contact with the ground, which could be another explanation for the large reduction in friction.

7.1.3 Vibration-Induced Friction Reduction and Uphill Propulsion

Although the frictional forces we have shown in Figure 7.2 are still too high, recall that, when the sheet is on, it is vibrating at up to several hundred hertz, and this vibration can actually reduce the friction considerably by reducing the apparent load. This vibration-induced friction reduction increases with the ratio of the speed of vibration (amplitude times frequency) to the speed of the sheet's forward motion. Thus, when the sheet is at rest, the friction is reduced sufficiently for it to begin moving, but as it speeds up, the reduction in friction decreases, and it reaches a steady-state speed. Since the sheet is now moving on the ground, we can determine the propulsive force by having the sheet move uphill: as the incline is increased, gravity provides an increasing backward force.

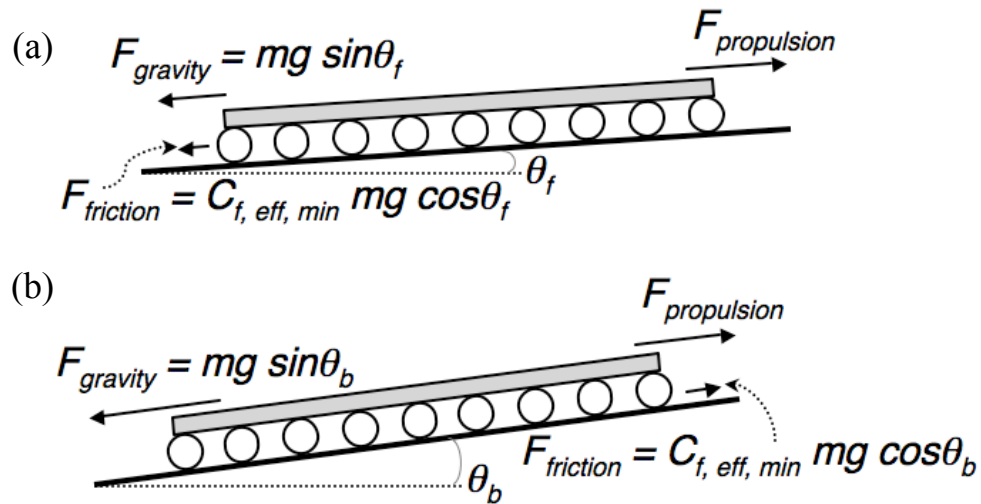


Figure 7.3 Illustration of sliding angle. **(a)** Lateral forces on the sheet when the incline is θ_f , the largest angle at which the sheet moves forward (uphill). That is, for $\theta < \theta_f$, the sheet moves forward. $F_{gravity}$ is the component of the gravitation force in the lateral direction. **(b)** Lateral forces on the sheet when the incline is θ_b , the largest angle at which the sheet is stationary (i.e., for $\theta_f < \theta < \theta_b$, the sheet is stationary, and for $\theta > \theta_b$, the sheet moves backwards).

Eventually, this gravitational force ($m g \sin \theta$), added to the frictional force ($C_{f, eff, min} m g \cos \theta$), will balance the propulsive force, F_p , and the sheet will stop moving forward, at an angle we will call θ_f (i.e. $F_p = m g \sin \theta_f + C_{f, eff, min} m g \cos \theta_f$; Figure 7.3a). If the incline is increased further, the sheet will remain stationary, because although the sum of the gravitational force and the propulsive force is now directed backward (i.e. downhill), it is not yet sufficient to overcome friction (which has switched to being directed forward). At some greater angle, θ_b , it will overcome friction, and the sheet will slide backward down the incline ($m g \sin \theta_b - F_p = C_{f, eff, min} m g \cos \theta_b$; Figure 7.3b). For small angles, the increase in the backward gravitational force is linear; hence, the angle half-way between θ_f and θ_b gives us the propulsive force – more precisely, $F_p - m g \sin \theta_f =$

$C_{f, eff, min} m g \cos \theta_f$ and $m g \sin \theta_b - F_p = C_{f, eff, min} m g \cos \theta_b \Rightarrow F_p = m g (\sin \theta_f \cos \theta_b + \sin \theta_b \cos \theta_f) / (\cos \theta_f + \cos \theta_b)$, where $C_{f, eff, min}$ is the minimum effective coefficient of friction (i.e. at zero sheet velocity, and hence with maximal vibration reduction of the friction). Measurements indicated that $\theta_f \approx 3.7$ degrees and $\theta_b \approx 8.3$ degrees (Figure 7.4a; Teflon “ski” data). This gives $F_p \approx (1.1 \text{ g}) \cdot (9.8 \text{ m/s}^2) \cdot (0.1) \approx 1 \text{ mN}$. This is considerably larger than previously measured propulsive forces, due to the higher frequency (500 Hz) of vibration and slightly longer sheet. This higher propulsive force means that we can tolerate greater friction – the coefficient of friction needs to be less than ~ 0.1 while moving at speeds up to that required for lift (expected to be around 20 cm/s). Also, the minimum effective coefficient of friction is calculated to be $C_{f, eff, min} = (\sin \theta_b - \sin \theta_f) / (\cos \theta_b + \cos \theta_f) \approx 0.04$. The vibration has thus reduced friction by a factor of ~ 12 when the sheet’s velocity is zero. The sheet’s steady-state velocity at 0 degrees was ~ 1.4 cm/s, which indicates that the effective coefficient of friction has been reduced from ~ 0.47 (see Figure 7.2) to $\sim (1 \text{ mN}) / (1.1 \text{ g}) \cdot (9.8 \text{ m/s}^2) \approx 0.09$, or about a factor of 5. Measuring the steady-state velocity versus tilt angle can give us the full relation between vibration-induced friction reduction and sheet velocity, as follows: At a given upward tilt angle, θ , the total force on the sheet (in the direction parallel to its motion) is $F_p - m g \sin \theta - C_{f, eff}(v) m g \cos \theta$. If the velocity reaches a steady state, this total force must be zero; hence, $C_{f, eff}(v) = (F_p - m g \sin \theta) / (m g \cos \theta)$, where the relation between θ and the steady-state velocity is measured experimentally. Note that, if the coefficient of friction did not increase with velocity, the sheet would continue accelerating, rather than reaching steady state (at least until aerodynamic drag dominates or the coefficient of friction of the ground increases – see Section 7.4). Finally, dividing $C_{f, eff}(v)$ by C_f , the coefficient of

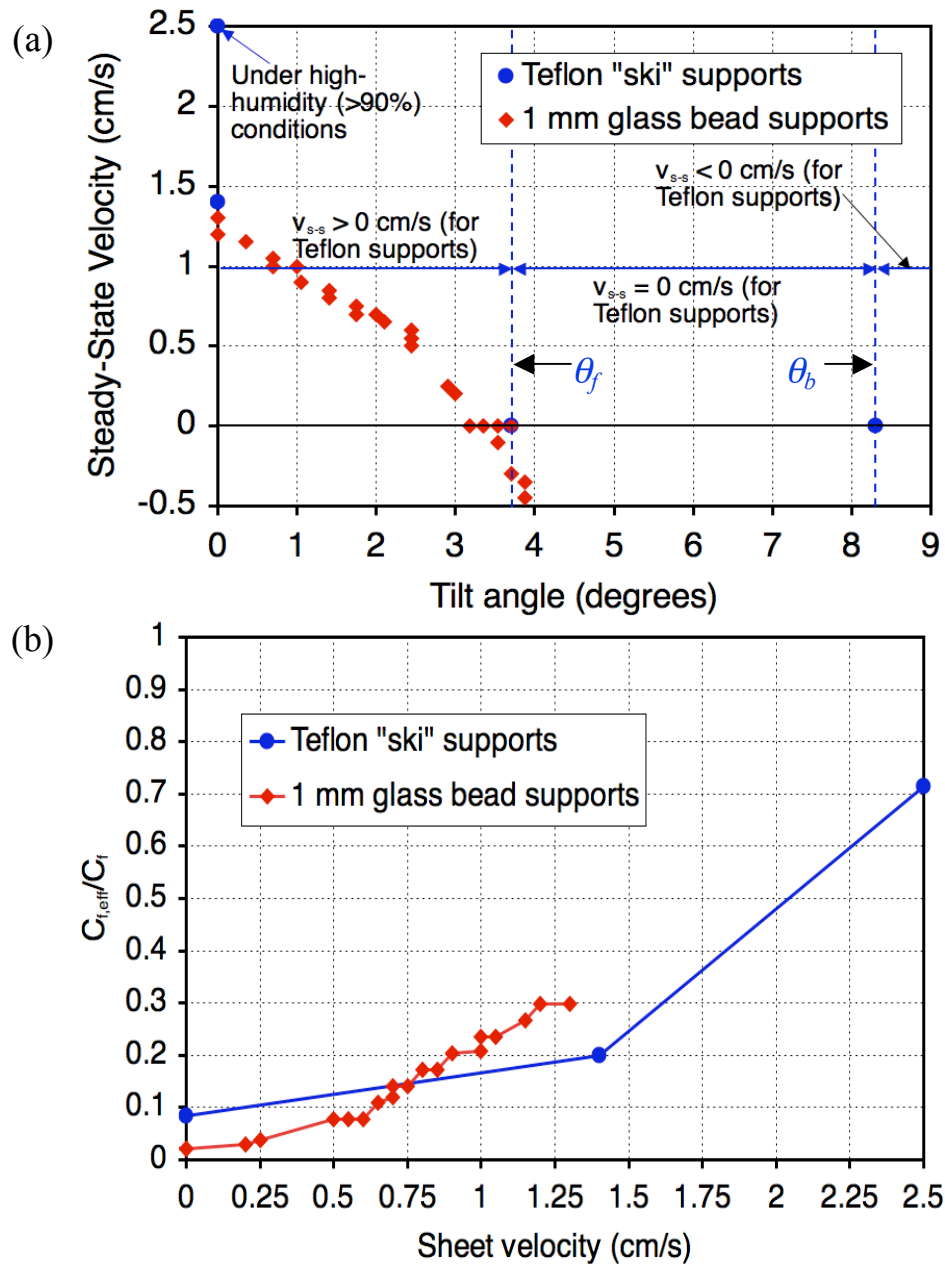


Figure 7.4 (a) The steady-state velocity of the sheet is shown as a function of uphill tilt angle for two samples. One of these had 1 mm glass bead supports (red diamond), and the other had Teflon “ski” supports (blue circles). The data point at 2.5 cm/s (Teflon “skis” sample) was measured under high humidity conditions. **(b)** The effective coefficient of friction under vibration is extracted from the velocity versus tilt angle measurements, as described in the text. It is smallest when the sheet’s velocity is zero, and increases towards its initial value (i.e. when the sheet is not vibrating) as the sheet’s velocity increases.

friction when the sheet is not vibrating, results in a normalized plot of vibration-induced friction reduction as a function of sheet velocity. Figure 7.4b shows the results for the sheet with Teflon “skis” (blue circles; note that the data point at 2.5 cm/s was measured under high humidity conditions, as described in Section 7.1.4), as well as a series of measurements for another sheet (red diamonds). This sheet had a somewhat lower propulsive force (~ 0.63 mN compared to ~ 1 mN), due to some damage to the sheet, and different supports under the sheet (1-mm glass beads instead of Teflon wedges), and C_f was ~ 0.19 . The results are similar between the two sheets, except for a greater friction reduction at very low speeds for the glass beads sample. As expected, the coefficient of friction increases towards its initial (i.e. when the sheet is not vibrating) value as the sheet’s velocity increases towards the speed of vibration (~ 500 Hz * 400 μm = 20 cm/s), although the data indicate that $C_{f, \text{eff}}(v)$ will reach C_f at velocities significantly less than this. Further measurements are needed to fully map out the dependence at higher speeds.

7.1.4 Methods to Reduce Static Electricity

Returning now to static electricity and pressure-dependence, we have established that these effects are creating a larger apparent coefficient of friction than would otherwise be observed, and we therefore need to find ways to eliminate or reduce these effects. This is necessary to allow the sheet to accelerate to the greater speeds required for lift (and the vibration effect may not help us sufficiently at these higher speeds). One method to reduce static electricity was found when it was noticed that $C_{f, \text{eff}}$ appeared to be lower on humid days – sometimes down to ~ 0.3 - 0.32 (compare with the ~ 0.47 reported in Figure 7.2). On one particularly humid occasion (it seemed close to condensing in the lab, due to

a problem with the air-conditioning, although no humidity sensor was available at the time), a value of $C_{f, \text{eff}} \approx 0.13$ was measured. Under these conditions, the steady-state speed of the sheet at zero tilt angle was observed to increase to ~ 2.5 cm/s (Figure 7.4a). Hence, at this speed, the vibration reduced the friction by a factor of only about 1.4 (Figure 7.4b). Video 7.1 of the online supplemental material shows the sheet moving at ~ 2 cm/s under similar conditions. The reasoning behind this humidity effect is that, in conditions of high relative humidity, there will be a slight surface conductivity on nominally insulating materials, allowing dissipation of accumulated static charge. Note that we can't just use a highly conducting surface as the ground, because when the sheet is operating, the high voltages applied to the actuators would create an attractive force between the sheet and the ground (this effect was observed when the sheet was suspended from elastic threads, and led to the use of insulating surfaces). Assuming that the surface is at ~ 0 V (since the voltages applied to the actuators are bipolar), this force would be $\sim 0.5 \epsilon_0 A (V/h)^2 \approx 2.5$ mN, where A is the area of the sheet, $V \approx 300$ V is amplitude of applied voltages, and $h \approx 1$ mm is the gap between the sheet and the ground. Since this is $\sim 25\%$ of the weight of the sheet, it would be a significant effect, especially as it would increase if the sheet moved closer to the ground, so it is preferable to avoid conductive materials for the ground surfaces. To test more precisely the theory that high humidity reduces the frictional coefficient, a small humidifier was connected into the box in which the sheet was being tested. A test sample was used for this measurement – a sheet of transparency about the same area and weight as the actual sheet. Tiny glass beads were used as the supports (see discussion below). At ambient conditions ($\sim 60\%$ humidity), $C_{f, \text{eff}}$ was ~ 0.17 . Increasing the humidity up to $\sim 85\%$ did not result in much change,

however by ~95% humidity, $C_{f, \text{eff}}$ had decreased to as low as ~0.09, which should be low enough to allow the sheet to accelerate even without vibration reduction. Care must be taken with the actual sheet, however, as this level of humidity can cause shorts, particularly around the edges of the sheet where there is only the 28 μm thickness of the PVDF separating several hundred volts. Further work is needed to determine the maximum practical humidity due to this issue.

7.1.5 Methods to Address Pressure-Dependence

Considering now the pressure-dependence of the friction, note that, given the low mass of our sheet, proper design of the tiny supports is necessary to increase the pressure sufficiently. For example, with no supports, the pressure would be only $\sim 1.7 \text{ N/m}^2$. Several designs for the supports have been tested: For the friction measurements described so far, Teflon wedges were used. These wedges were $\sim 1 \text{ mm}$ long, and we estimate the width of the pointed end (which touches the ground) to be $\sim 100 \mu\text{m}$. The pressure should then be $\sim 4100 \text{ N/m}^2$ (recall that around 27 supports are needed to avoid sagging of the sheet between the supports). Three other kinds of support have been tested, and led to similar results: slices cut from a Teflon-coated wire ($\sim 500 \mu\text{m}$ in diameter and $\sim 500 \mu\text{m}$ thick), bent stainless steel wires ($100 \mu\text{m}$ in diameter), and glass beads ($\sim 500 \mu\text{m}$ diameter). The contact area of these supports is tricky to measure, due to the curved surface which contacts the ground, but something in the range of ~ 0.01 to 0.05 mm^2 is plausible. This would result in pressures of $\sim 8,000$ to $40,000 \text{ N/m}^2$. Further measurements are needed to determine this more precisely. All of these supports resulted in $C_{f, \text{eff}} \approx 0.17$ to 0.19 on normal days (humidity ~ 50 - 60%). The lower friction of these

supports compared with the wedges may be due partly to their smoother surface (the wedges were hand-cut), in addition to the somewhat higher pressure. The pressure does have some effect, as can best be seen by changing the number of supports (this way, no other factors change). For example, with 10 bent stainless steel wires, the coefficient of friction was $C_{f, \text{eff}} \approx 0.18$, but with 6, $C_{f, \text{eff}} \approx 0.12$. Ideally, we would like to increase the pressure further, to avoid limiting operation to high-humidity environments, but more work is needed to achieve this.

Once the friction is reduced by these means (reduced support contact area to increase the pressure, and high humidity to reduce the static charge), we expect the sheet to be able to accelerate beyond its current $\sim 1\text{-}2$ cm/s up to ~ 20 cm/s. This should, theoretically, be sufficient to produce lift (see Section 5.3). In addition, however, the sheet needs to be free to move more than a few centimeters, as it is restricted to by the electrical connections. One way to achieve this, providing on-board power, was discussed in Section 6.3, and another approach, having a cart that follows the sheet, is discussed in Section 7.3.

7.2 Lift Testing

Before attempting to measure lift for the actual “flying carpet”, an important test is to determine whether lift can be observed in passive test samples (i.e. no internal propulsion) moving sufficiently fast. Theory predicts that this should occur, regardless of how the sample achieves its speed. To this end, a ramp was constructed so that passive samples could be accelerated by gravity. The ramp was covered with Teflon tape, 30 cm wide and 240 cm long, and treated with an anti-static spray (ACL Staticide). These

experiments were performed at ambient conditions (~60% humidity). A video camera was used to observe several test samples (16 cm x 4 cm transparencies) sliding down this ramp. Figure 7.5 shows two examples when the ramp is tilted at 11°.

For one sample, glass beads of varying diameter were used as supports – from 2 mm at the front end to zero at the back end. This created a forced angle of attack that might enhance lift. From the measurements shown in Figure 7.5 (and in Video 7.2a of the online supplemental material), we see a rapid initial acceleration in the first few hundred milliseconds, after which the acceleration decreases until the velocity reaches ~30 cm/s, when the acceleration increases again. At around 60 cm/s, the sample begins to rotate – i.e. the back starts moving faster than the front. The speed of the front end levels off at ~70 cm/s, while the back end reaches at maximum of ~100 cm/s. This occurs when the sample has rotated nearly 90°. The speed of the back end then drops rapidly, and the sample begins rotating back towards its original orientation. These observations are consistent with the idea that the sample is initially approaching a steady-state velocity of perhaps 30-40 cm/s, due to the fact that Teflon's coefficient of friction increases with speed (note that this effect is very small at speeds below a few cm/s, so it was ignored in the discussions in Section 7.1). Then, at ~30 cm/s, the back end of the sample begins to lift, which reduces the overall friction and allows the sheet to accelerate to a higher speed. We expect the back end to lift first for this sample, because the back end is initially resting on the ground, and the air needs a way to escape (of course, it can escape to the side, but there is still some pressure causing it to lift). We can also see this by noting that the initial “forced” angle of attack ($2h/L$; where h is the average gap between the sheet and the ground, and L is the sheet's length) is greater than that predicted

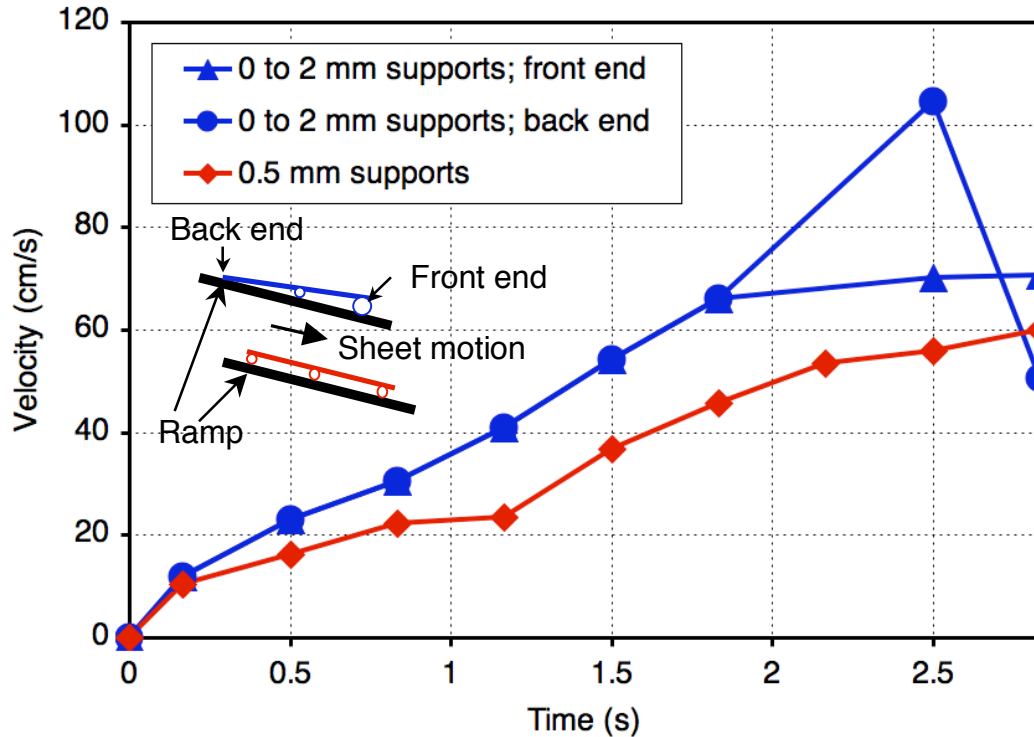


Figure 7.5 Plot of velocity versus time for two passive test samples sliding down an 11° ramp. The sample with 0 to 2 mm supports shows signs of its back end lifting, while the sample with 0.5 mm supports shows signs of its front end lifting, as described in the text. The front and back ends of the 0 to 2 mm sample begin moving at different speeds, while for the 0.5 mm sample, the back and front ends move at the same speed.

theoretically (h/L) for steady-state, and the beads prevent the front end from falling down. However, the back end of the sample is now experiencing greater acceleration than the front end, due to the lack of ground contact friction at the back. Therefore, if the sheet is not moving perfectly straight, it begins to rotate, with the back end reaching considerably higher speeds (up to ~ 1 m/s in this case). This does not last long, however, as once the sheet is moving at an angle, the air is no longer forced under it as effectively, and the back end will no longer lift. Since the back end of this sample rests directly on the ground when no lift is occurring, it then experiences higher friction than the front end (2-mm glass beads), and slows down again.

For the other sample, the supports are all ~ 500 μm glass beads, as might be used for the actual sheet. The measurements in Figure 7.5 (See Video 7.2b of the online supplemental material) show that after an initial acceleration, the speed begins to level off at ~ 25 cm/s , but then accelerates again to a new speed of ~ 60 cm/s . This is consistent with the idea that the sample initially approaches a steady-state speed due to the increasing friction (same as for the other sample), but just barely reaches a high enough speed to cause the front end to lift, reducing the friction so the sample can accelerate further. For this sample, the front end is expected to lift before the back end, because the sheet initially has a smaller angle of attack than the predicted steady-state value (i.e. approximately level; but if any vibration causes the sheet to be even slightly higher in the front, it will tend to tilt more, as described in Chapter 2). And in this case, the beads prevent the back end from dropping. Note that, since the front end is lifting, the instability observed in the other sample does not occur, and the sample's motion is very straight.

Further experiments are needed to fully explore these lift phenomena, such as dependence on the size of the beads and the angle of the ramp (which changes the forward force on the sample), which should also verify that no other effects are occurring. For example, if the angle of the ramp were increased, we would expect the lift transition to occur sooner in time, but at roughly the same speed. Returning to the actual "carpet", the maximum velocity observed so far is ~ 2.5 cm/s , which, as we have seen, is not sufficient to produce lift. It is expected that this could increase to the necessary values if friction and static electricity are reduced sufficiently; alternatively, if the sheet is moving down an incline, as in the test setup described above, we would expect to observe the beginning of lift sooner due to the greater forward force on the sheet.

7.3 Power on Cart

As a potential method to demonstrate lift, a cart was constructed that could be connected to the power supply while following the sheet (Figure 7.6a and Video 7.3 of the online supplemental material). This allows the sheet to move freely without requiring on-board power. To ensure that the electrical connections (conductive threads) from the sheet to the cart provide negligible force on the sheet, the cart must deviate no more than ~1 cm from the sheet's motion. A simple LED –photodiode circuit, along with a graded transparency filter affixed to the sheet, was used to control the motor driving the cart (Figure 7.6b). The opacity of the filter is graded to soften the transition between the on and off states of the motor. This cart is able to move up to ~20-30 cm/s, which should be sufficient to observe lift.

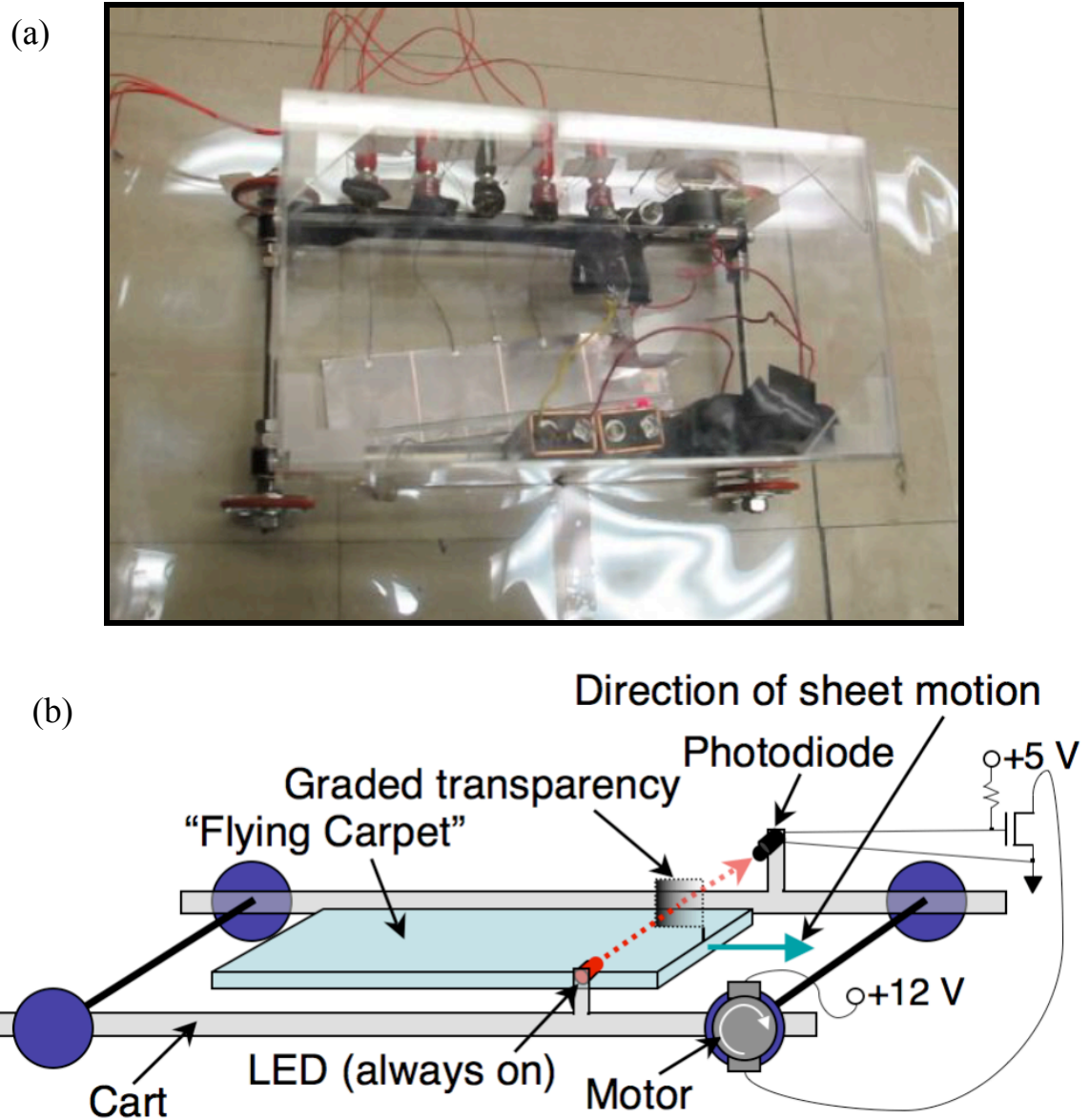


Figure 7.6 (a) Photo of a motorized cart that can follow the sheet to provide power. (b) Schematic of cart-following arrangement.

Chapter 8

Printing of Silicon

Our attempt at on-board power (Section 6.3) for the “flying carpet” involved adding commercially available chips onto the PVDF. It would be desirable to form the electronics directly on the PVDF, which could perhaps be done using a-Si. However, PVDF can only tolerate temperatures below $\sim 60^\circ\text{C}$, and polycrystalline silicon would be preferable for higher performance. Thus, in this chapter, we discuss the formation of silicon thin-films from silicon-nanoparticle suspensions, as preliminary work towards room-temperature fabrication of electronics. A brief overview is provided in Section 8.1, and Section 8.2 introduces the topic by discussing previous related work. In Section 8.3, we explain our experimental methods and results, from considerations guiding our choice of method (8.3.1) to porous silicon formation (8.3.2), silicon nanoparticles (8.3.3), and finally, silicon thin-films (8.3.4). Section 8.4 summarizes our results and discusses several future research directions.

8.1 Abstract

We report the room-temperature formation of smooth and processable silicon thin-films from single-crystal silicon-nanoparticle suspensions [17]. Single-crystal Si-nanoparticles (1 – 4 nm) are produced and suspended in various solvents. Films deposited from the

suspension are mechanically stable and can be patterned and processed upon deposition. Physical compression of the films is presented as a mechanism to reduce porosity and global roughness. These thin-films, ~ 100 nm thick and deposited from a single droplet, contain significant levels of hydrogen, carbon, and oxygen. Resistivities of the as-deposited films are $\sim 7 \cdot 10^7 \Omega \cdot \text{cm}$ – comparable to intrinsic nanocrystalline-Si.

8.2 Introduction

8.2.1 Background/Prior Work

Additive patterned processes, such as ink-jet printing, are very attractive because they avoid the need for photolithography and etching of blanket layers, waste less material, and have the ability to cover large, flexible substrates. However, wet printing of semiconductors is currently limited primarily to solution-processable organic/polymer semiconductors, which have low mobility (typically up to $\sim 0.1 \text{ cm}^2/\text{V}\cdot\text{s}$ [36], with some reports of $\sim 1 \text{ cm}^2/\text{V}\cdot\text{s}$ [26]). For comparison, the mobility of amorphous silicon used currently in AMLCD displays is $\sim 1 \text{ cm}^2/\text{V}\cdot\text{s}$, and that of crystalline silicon as used for VLSI is $\sim 1000 \text{ cm}^2/\text{V}\cdot\text{s}$.

Recent work on printing silicon from nanoparticles has shown much promise [2], [14]. Harting *et al.* [14] report screen-printed films from relatively large nanoparticles (~ 70 nm diameter), and show mobilities up to $\sim 0.5 \text{ cm}^2/\text{V}\cdot\text{s}$ in as-deposited films. The nanoparticles have an internal grain structure and are produced by mechanical milling of 0.01-0.03 $\Omega\cdot\text{cm}$ n-type wafers. However, such large particles would lead to rough films and could preclude thin gate dielectrics. This prior work used gate dielectrics of 5-50 μm . The work of Antoniadis *et al.* [2], on the other hand, still requires heating in the 300-900°

C range. Other methods for printing silicon [35], [13] involve producing printable liquid polysilanes (compounds of Si and H). However, this approach includes the necessity for annealing up to 540° C to produce an a-Si film [35] (with mobilities of only $\sim 10^{-3}$ $\text{cm}^2/\text{V}\cdot\text{s}$), and the need for further laser-crystallization to achieve mobilities of ~ 100 $\text{cm}^2/\text{V}\cdot\text{s}$.

8.2.2 This Work

In this work we seek an approach similar to that of Reference [14], depositing droplets of a suspension of Si-nanoparticles with no post-processing heating steps, but with a goal of smooth and processable thin-films ($<200\text{nm}$) through the use of much smaller (1-4 nm), single crystal Si-nanoparticles. We desire single-crystal particles in order to maximize the grain size for a given nanoparticle size – this could thus lead to films with properties similar to nc-Si (i.e. the potential for higher mobility than amorphous silicon). In addition, we present post-deposition compression as a potential room-temperature alternative to standard annealing.

8.3 Experimental Methods & Results

8.3.1 Choice of Silicon-Nanoparticle Production Method

Before beginning experiments, we must choose a method for producing the silicon nanoparticles. This choice depends on our requirements: As mentioned earlier, we are aiming to form very small (i.e. several nm) particles, to enable production of thin-films (<200 nm). In addition, in order to have any hope of achieving electronic properties better than amorphous silicon, we need the nanoparticles to be single-crystal. Several other

conditions are ease of use, rate of nanoparticle production, and ability to produce “ink” for printing. These requirements together make electrochemical-etching to produce porous silicon, followed by sonication of the porous silicon to create nanoparticles, look like an attractive route. Because such methods involve mechanically crumbling part of a single-crystal wafer, they result in single-crystal particles, and production of nm-scale nanoparticles of silicon has been previously demonstrated [1]. In addition, because the sonication step occurs separately from the etching step, it provides great flexibility in the suspension liquid’s composition and surface tension. Running the sonication step repeatedly in the same suspension vial should easily increase the concentration of nanoparticles (at least until aggregation of the particles begins).

8.3.2 Porous Silicon

We began by forming porous silicon through an electrochemical etching procedure [44] (Figure 8.1). A silicon wafer (p-type, 1-10 Ω -cm) is suspended in a beaker of HF_{49%} (49% in H₂O), and a voltage is applied between the wafer (the anode) and a platinum cathode. Because the reaction is dependent on the presence of holes (in the p-type Si wafer), the etching will be faster in regions of higher hole concentration (and the current density is thus also greater in these regions). This leads to etching in a semi-random manner (depending on the overall current density, small variations in doping, HF concentration, crystal orientation, etc.), resulting in porous silicon. Previous work [44] used a mixture of HF_{49%} and H₂O₂ (30% in H₂O), with H₂O₂: HF_{49%} > 2:1, as this had produced the ‘best’ results (smallest particles, narrowest size distribution, lowest percentage of oxygen-terminated Si-bonds). Adding H₂O₂ has the effect of oxidizing the

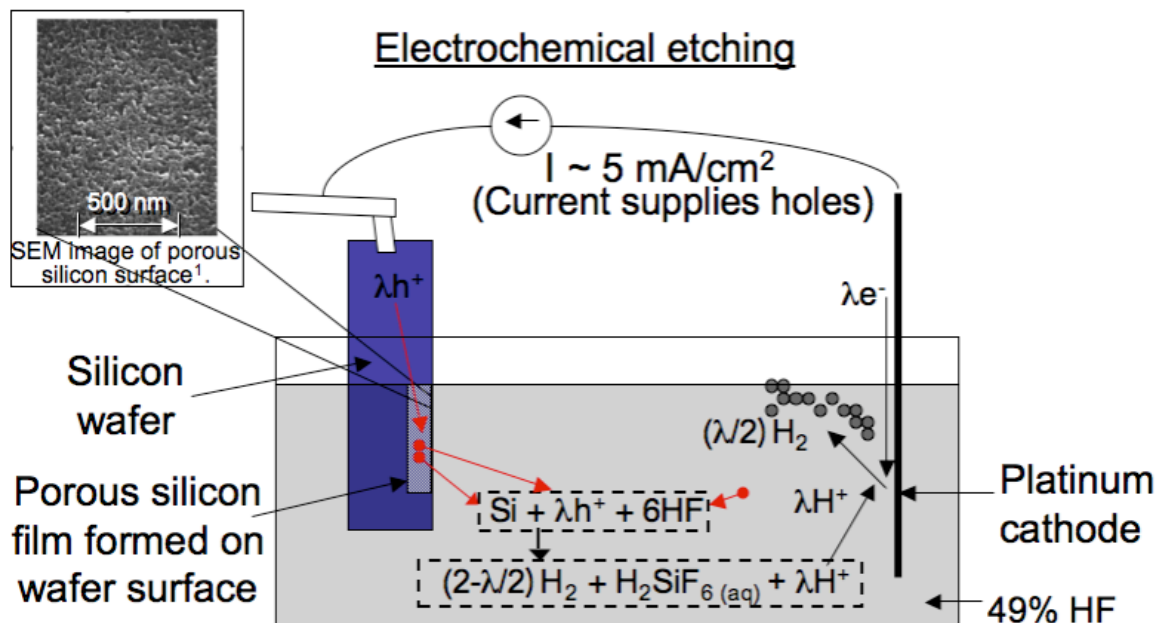


Figure 8.1 Diagram showing experimental arrangement for electrochemical etching of silicon, with relevant reactions. An example of a resultant porous silicon surface from the literature [44] is shown in an SEM image.

silicon, while the HF dissolves this oxide, thus increasing the etching rate. It has been shown that current densities of $\sim 5 \text{ mA/cm}^2$ result in etched silicon structures with a characteristic length scale of a few nanometers [44], so we used similar densities in this work. The etching lasted for ~ 1.5 hours, and went to a depth of $\sim 5\text{-}15 \mu\text{m}$ (as determined from mass lost after etching and ultrasound). To make good electrical contact to the silicon wafer during etching, and improve the reproducibility of results, flat ‘clips’ of area $\sim 4 \text{ cm}^2$ were used to contact the wafer. The silicon wafer was placed perpendicular to the acid surface, with electrical contact made at the exposed end. Because of a resistive voltage drop moving away from the contact, porous silicon with features at the desired scale occurred only in a narrow region ($\sim 1\text{-}5 \text{ mm}$) of the wafer near the acid surface due to the higher current density there. In previous work [1], the area of silicon exposed to the

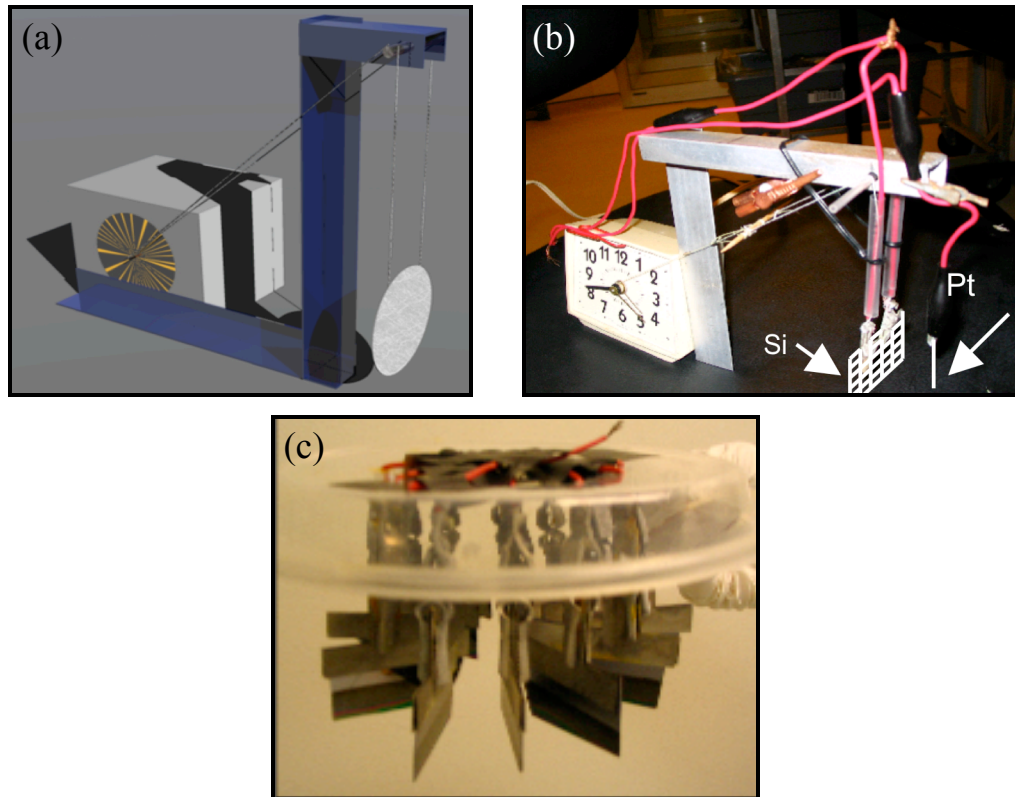


Figure 8.2 (a) Concept for a device that lowers the wafer at a rate of ~ 1.2 mm/hour (which keeps fresh silicon exposed to the acid). (b) Realization of this device using an electric clock, and electrical contact to the wafer via alligator clips. (c) Multi-wafer parallel etching apparatus.

acid was increased by lowering the wafer slowly at a rate of ~ 1 mm/hour. In our initial experiments, we followed this same idea, constructing a simple device to achieve such lowering using an electric clock (Figure 8.2a and 8.2b). However, as this only increased the exposed area by a factor of ~ 2 over the course of the etching, a different apparatus was constructed for high throughput, in which ~ 10 wafers were contacted and etched at once (Figure 8.2c). The photoluminescence (PL) spectra of the porous silicon produced were measured under various production conditions (current: $\sim 0.04 - 4$ mA/cm², voltage: ~ 0 V – 17 V, and HF_{49%} to H₂O₂ ratio: 1:1 – 1:3). The incident light was 254 nm UV. All spectra showed similar forms, with peaks at ~ 650 -750 nm, and FWHM of ~ 150 nm

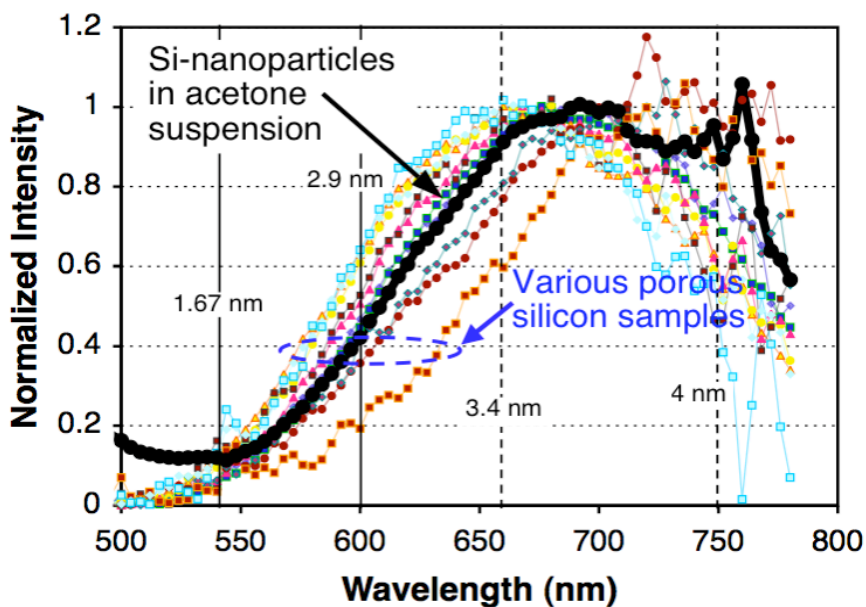


Figure 8.3 Luminescence spectra of porous silicon samples producing under various conditions (current: $\sim 0.04 - 4 \text{ mA/cm}^2$, voltage: $\sim 0 - 17 \text{ V}$, and $\text{HF}_{49\%}$ to H_2O_2 ratio: 1:1 – 1:3), and luminescence of a vial of nanoparticles suspended in acetone (current: $\sim 5 \text{ mA/cm}^2$, voltage: $\sim 15 - 25 \text{ V}$, and $\text{HF}_{49\%}$ to H_2O_2 ratio: 1:3). Lines indicate several particles sizes corresponding to previous PL measurements (solid and dashed lines are from References [5] and [20], respectively).

(Figure 8.3). These results are broadly consistent with past measurements of porous silicon luminescence [6] (peaks in the 500-1000 nm range and FWHM of $\sim 150 \text{ nm}$). Previous measurements [5], [24], [20] predict $\sim 2\text{-}5 \text{ nm}$ features for the observed emission wavelengths, which is in reasonable agreement with the TEM images of the nanoparticles we produced from these structures (Figure 8.4). For reference, we indicate with lines in Figure 8.3 several particles sizes corresponding to measured PL [5], [24], [20] (solid lines are from Reference [5]; dashed lines from [20]).

8.3.3 Silicon Nanoparticles

Single-crystal silicon nanoparticles ranging from 1 nm to 4 nm in diameter were produced as a suspension in acetone or other solvents (such as water) by ultrasonic agitation of the porous silicon wafer in the chosen solvent for ~60 min. Physical vibration crumbles the porous silicon film into nanoparticles [1], which then disperse into the solvent. Acetone was primarily used because it evaporates quickly during the later printing step. Production of nanoparticles is maximal for etching current densities of 2 to 10 mA/cm², and using only HF_{49%}. Under these conditions (and for ~50 cm² of etched wafer), the total mass of silicon consumed by the production process is ~30-70 mg per hour of processing (etching and ultrasound), as determined by weighing the silicon wafer before etching and after the ultrasound. The total mass of nanoparticles produced is ~5-11 mg/h, as determined by weighing printed films. Hence, ~20% of the consumed silicon is retained as nanoparticles. Assuming an average particle diameter of ~2 nm, the nanoparticle production rate is ~5·10¹⁷ particles per hour.

Luminescence measurements and direct TEM imaging were used to determine the size distribution and verify the crystallinity of the particles. A copper grid with carbon film (for TEM) was dipped into a vial of solution, and allowed to dry. TEM images of the nanoparticles show that they are single-crystal, through the presence of lattice fringes [29], and range from 1-4 nm in diameter (Figure 8.4a). The diameters of the particles were measured directly from TEM images (Figure 8.4b) by drawing two circles on each particle – the largest circle that fit inside, and the smallest circle that contained the particle – and taking the average, leading to the size distribution plot shown in Figure 8.4c. Two different TEM grids for the same solution (etching conditions: current ~ 3 – 10

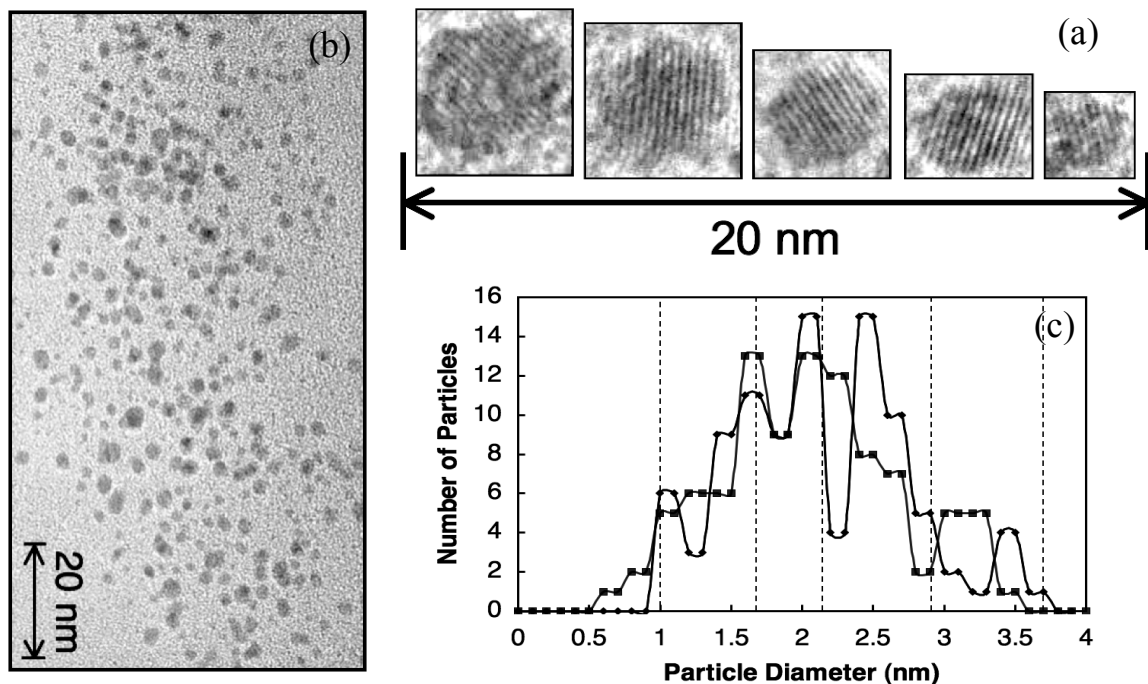


Figure 8.4 (a) High-resolution TEM images of several nanoparticles in the 1-4 nm range. The presence of lattice fringes indicates crystallinity. (b) TEM image showing a large number of Si-nanoparticles on a carbon film. (c) Size distribution plot of the nanoparticles. The two plots are for two different TEM grids, but from the same vial of nanoparticles.

mA/cm², voltage: ~30 – 70 V, and HF_{49%} only) were analyzed. The distributions showed prominent peaks, some which (e.g. 1.7 and 2.1 nm) were observed on both grids. Discrete peaks in nanoparticle size were observed in a similar work [5] - the vertical lines in Figure 8.4c indicate the sizes (1, 1.7, 2.15, 2.9, and 3.7 nm) they measured. There is qualitative agreement between these sizes and the peaks in our data, but we did not perform any rigorous statistical analysis. Under 302 nm excitation, luminescence was observed for some of the vials of nanoparticles (when the etching current was ~3-10mA/cm²), with a spectrum quite similar to that observed for the initial porous silicon

(Figure 8.3). The expected particle sizes ($\sim 2\text{-}5$ nm) for this spectrum are thus similar to those observed with TEM.

8.3.4 Silicon Thin-Films

Si-nanoparticle thin-films were printed using a syringe to deposit droplets of the nanoparticle suspension onto the desired substrate. For thin film creation, using only HF_{49%} in the porous-silicon etching step gives ‘better’ results (smooth, continuous films), perhaps due to a greater volume of nanoparticles produced. Each drop is ~ 3.3 μL in volume, and once evaporated, the resultant film is ~ 4 mm in diameter. It is desirable to deposit the entire film from only one drop of the suspension – we have produced sufficient quantities of the particles to enable such deposition of thin-films on the order of 100 nm thick. The volume concentration of the nanoparticles in the suspension (C_v) is a critical factor in film production (this is estimated by weighing films printed from a known volume of the suspension). Our experiments indicate that if the concentration is too low ($<1/10000$ by volume), only scattered particles or conglomerates of particles will deposit on the substrate (Figure 8.5a), and a continuous film will not form. On the other hand, if the concentration is too high ($>1/2000$), the film will be greater than ~ 300 nm thick, and cracking or peeling will result (Figure 8.5b). Thus far, only films less than $\sim 200\text{-}300$ nm thick have been produced without cracks. Continuous films have successfully been produced for volume fraction concentrations, C_v , of $\sim 1.6 \cdot 10^{-4}$ to $3.8 \cdot 10^{-4}$. These films are continuous over the entire area of the deposited droplet (~ 0.25 cm^2), with little variation in the thickness. Figures 8.5c and d show such a film ~ 150 nm thick produced from a suspension with $C_v \sim 1.8 \cdot 10^{-4}$.

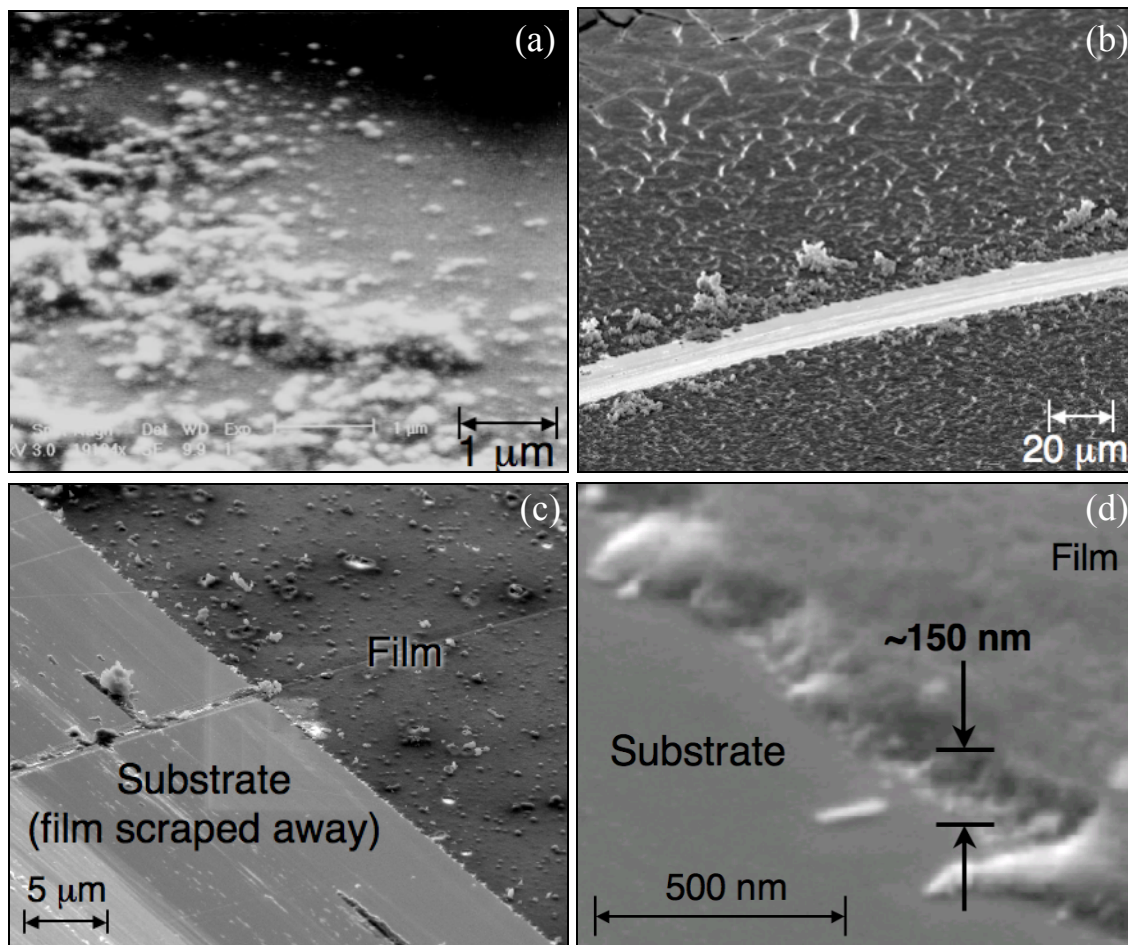


Figure 8.5 (a) SEM image showing result of deposition when the nanoparticle concentration (C_v) is less than $\sim 1/10000$ – no continuous film is formed. (b) When the concentration is greater than $\sim 1/2000$, the resultant film is too thick, and cracking occurs. (c), (d) A continuous film ~ 150 nm thick produced from a suspension with $C_v \sim 1/5600$.

The films (etching conditions: current $\sim 3 - 10$ mA/cm², voltage: $\sim 30 - 70$ V, and HF_{49%} only) were characterized by scanning electron microscopy (SEM) and atomic force microscopy (AFM) to determine thickness and surface roughness, SEM and weighing to determine porosity, and energy dispersive X-ray spectroscopy (EDX) and secondary ion mass spectroscopy (SIMS) to determine composition. Films were deposited on germanium substrates to allow compositional analysis. AFM analysis of the as-deposited films indicate a global roughness of ~ 160 nm RMS (Figure 8.6a), which at

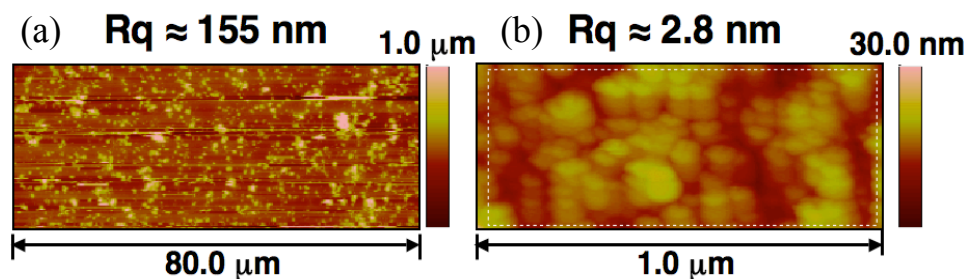


Figure 8.6 AFM images showing (a) global roughness (dominated by surface particles), and (b) local roughness (intrinsic film).

this scale is dominated by anomalous contamination of large particles on the surface. There was no sign of such clusters or large particles in the TEM data, even at low magnification, so we can conclude that their presence in the printed films is due either to clustering of smaller particles that occurred only when sufficient numbers of the nanoparticles were deposited (the TEM grid was just briefly dipped in the solution), or to larger particles or clusters in solution which did not stick to the TEM grid. In any case, the local roughness, between the large particles, of ~ 3 nm RMS (Figure 8.6b) is indicative of the intrinsic film property. SEM images show pores on the scale of ~ 10 - 50 nm (Figure 8.7), which is much larger than the nanoparticle sizes (1-4 nm). By depositing a large number (~ 100) of drops on a substrate, a thick enough film (~ 10 μm) was formed to measure a difference in the weight of the sample due to the deposited film. This, along with a measurement of the volume of the film, allows the porosity to be estimated at $\sim 50\%$ to 90% . As a comparison, the porosity that we would obtain if the film were simply composed of touching spheres would range from 26% for an fcc structure to 48% for a cubic structure.

We demonstrate that this high porosity of the film can be reduced by mechanical compression. Using a hard stamp formed from a silicon wafer, with pressures of ~ 20 - 50

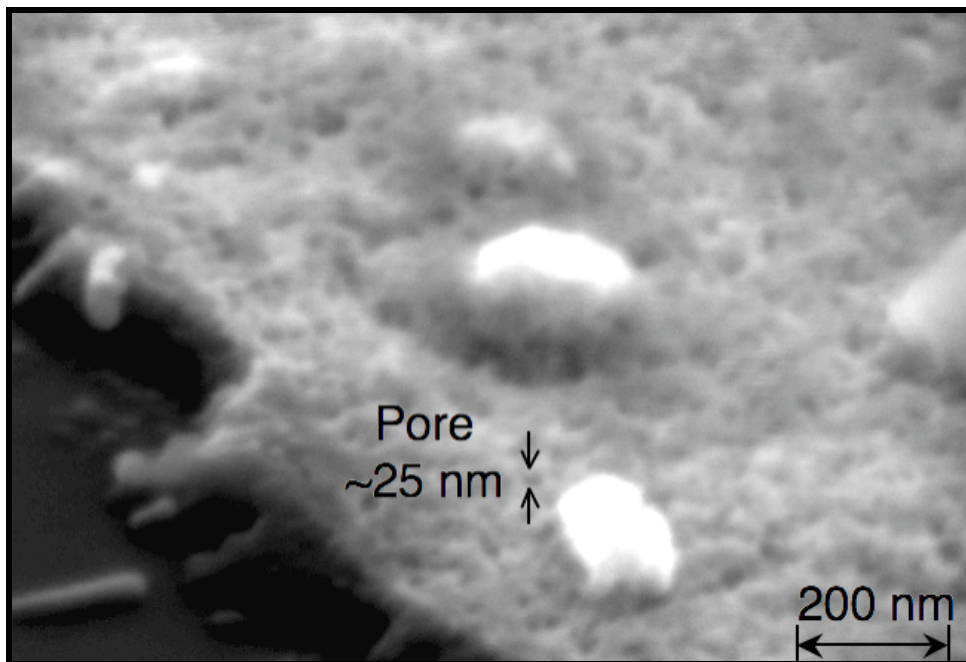


Figure 8.7 SEM image showing large surface particles, and also pores in film, as seen by indentations in the surface. Arrows indicate one such pore.

psi, we have achieved ~50% reduction in the thickness of the film, compared to the as-deposited film (Figure 8.8). In addition, this compression resulted in a reduction of the global surface roughness (Figure 8.8). The inset in Figure 8.8 shows that ‘pores’ seen in the uncompressed region (and in Figure 8.7) are no longer visible in the compressed region. Further, the large particles seen in the as-deposited films were no longer present. After stamping, the stamp was inspected in the SEM, and no transfer of material or particles to the stamp was observed. Hence, we conclude that the larger surface particles/clusters have been compressed into the film or broken up by the compression process.

SIMS (Secondary Ion Mass Spectroscopy) analysis of a ~150-nm film deposited on a germanium substrate (without compression), using acetone as a solvent, confirmed that the deposited film was mostly silicon (Figure 8.9). The carbon concentration was ~10

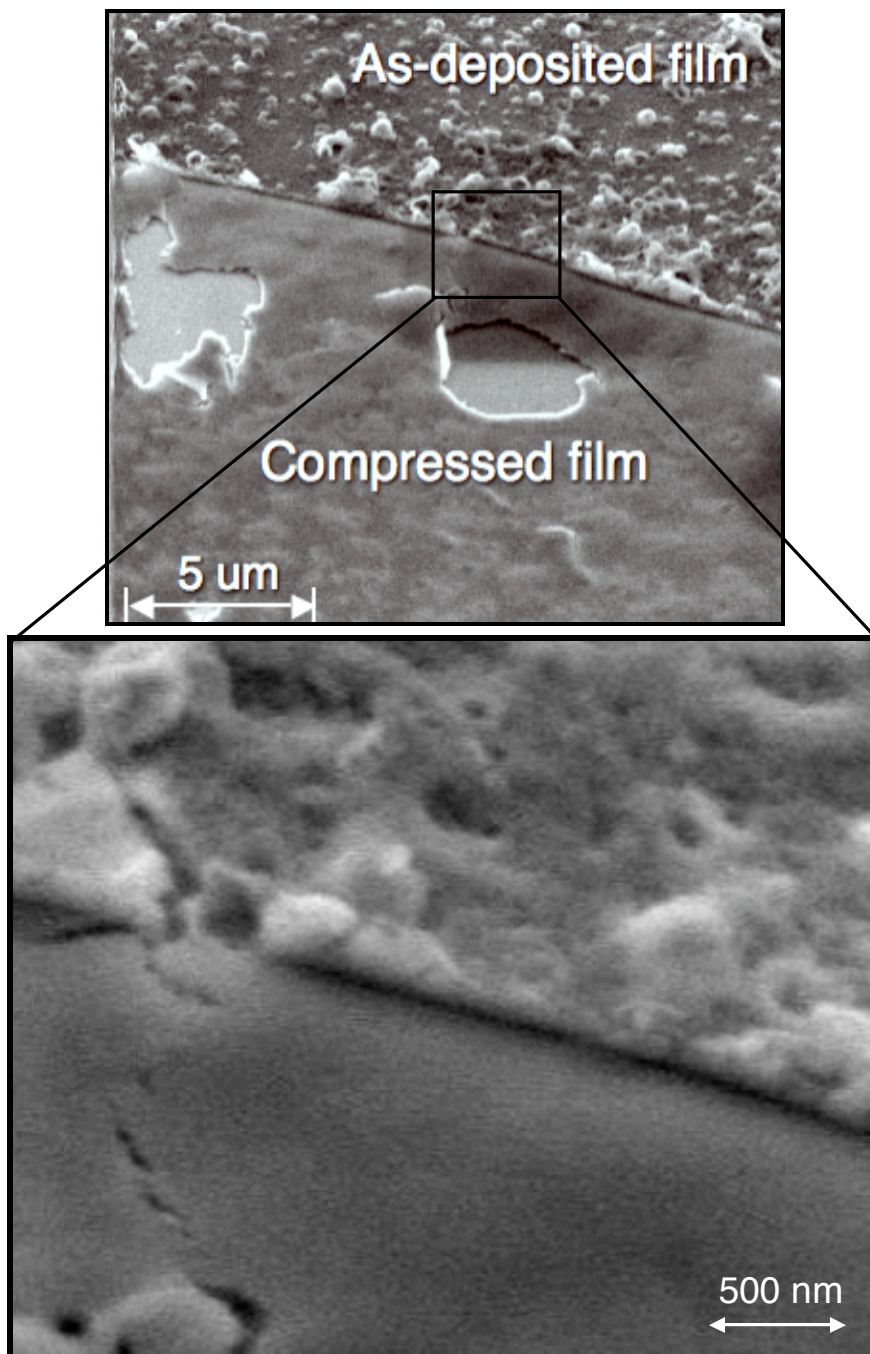


Figure 8.8 SEM image of film compression (~20-50 psi). Inset shows absence of ‘pores’ in compressed area.

atomic % throughout the film, while the oxygen level was ~1 at.% in the bulk of the film. Using water instead of acetone as the solvent did reduce the carbon content to <1 at.%, but detrimentally increased the oxygen content to over 30 at.%. We conclude that the

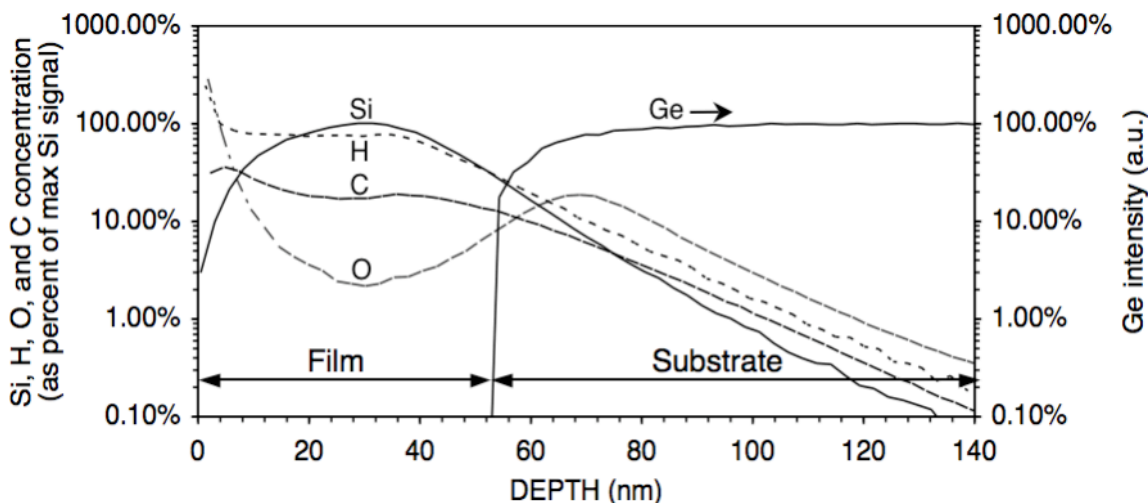


Figure 8.9 SIMS analysis of the film. Si-film is on the left side, germanium substrate on the right.

high carbon content in the acetone-suspension films is due to residual acetone on or between the nanoparticles. The number of hydrogen atoms was nearly the same as that of silicon, which is consistent with the idea that the silicon bonds on the nanoparticles' surfaces are primarily hydrogen-terminated: a 2 nm diameter silicon nanoparticle can be estimated from standard computations to consist of ~ 300 silicon atoms. About ~ 170 of these would be surface atoms, each able to bond ~ 2 hydrogen atoms, on average. For the acetone-prepared films, the number of oxygen atoms in the bulk of the film corresponded to a maximum of 3-6 oxygen atoms per Si-nanoparticle. For the water-prepared films, the 30 at.% oxygen, along with only ~ 3 at.% hydrogen, indicated that the nanoparticles were primarily oxygen-terminated.

To demonstrate chemical and physical stability, films deposited on SiO_2 from the acetone suspensions, even without compression, have been shown to withstand common solvents, photoresist developer, chrome etch, etc. They can be patterned (Figure 8.10) using a typical dry (plasma) silicon etch ($\text{SF}_6/\text{CCl}_2\text{F}_2$: 60/20, 100mT, 100W). The etch

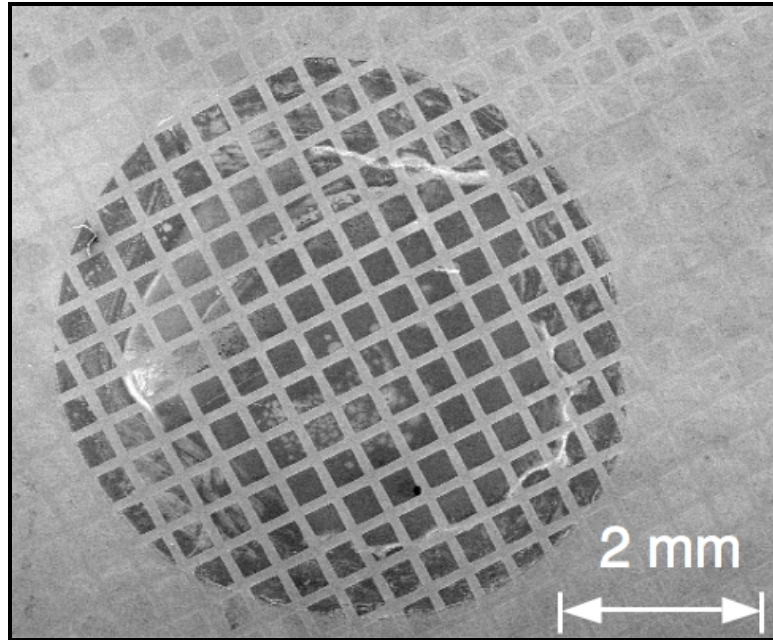


Figure 8.10 SEM image of the film after patterning to demonstrate its chemical and physical stability. Substrate is SiO₂ on Si.

rate was much slower ($\sim 10\text{-}20$ nm/min) than the $\sim 50\text{-}100$ nm/min expected for nc-Si. Possible causes of the slower etch rate include surface oxide (extends ~ 10 nm into the film; Figure 8.9) and relatively high oxygen or carbon content within the bulk of the film. Films formed from the water-suspensions were highly non-uniform in thickness and did not continuously cover the substrate. No process patterning or electrical measurements were thus carried out on these samples. Two terminal electrical measurements indicate that the as-deposited acetone-prepared films have dark resistivities of $\sim 7 \cdot 10^7$ $\Omega \cdot \text{cm}$, comparable to that of intrinsic nanocrystalline silicon [34] produced by thermal decomposition of silane onto SiO₂.

8.4 Summary & Future Directions

8.4.1 Summary

Single-crystal silicon nanoparticles (1 to 4 nm in diameter) have successfully been produced and suspended in various solvents by the sonication of porous crystalline silicon. We have demonstrated a process for creating thin films of these silicon nanoparticles by wet printing. The films are mechanically stable and can be patterned and processed, without any temperature treatment after deposition. Thin films ~ 100 nm thick have been deposited from a single droplet. They are locally smooth, but highly porous. The porosity and global surface roughness can be significantly reduced by mechanical compression. The measured resistivity of the as-deposited films are $\sim 7 \cdot 10^7 \Omega \cdot \text{cm}$, which is comparable to intrinsic nanocrystalline-Si.

8.4.2 Future Work

One of next important steps is determine whether the physical compression improves the electrical properties of the film, as well as having reduced the porosity. Since we have halved the thickness of the film through compression, we would expect the resistivity to at least be halved. However, it remains to be seen whether there is any additional improvement, for example, due to improved connectivity between the silicon nanoparticles.

Another area of investigation is to compare electronic properties of films produced from different suspension liquids (for example, acetone versus water). To test this for the water-suspensions, the surface tension will need to be tuned to allow more uniform film deposition (which has thus far precluded electrical measurements on these films). Other

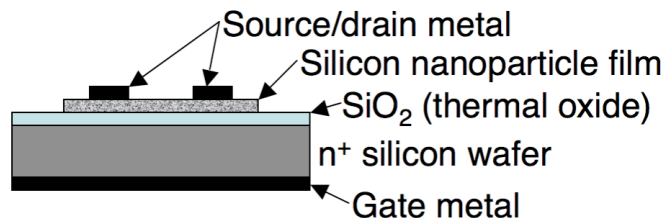


Figure 8.11 TFT test structure.

possibilities include using a liquid polysilane (such as in References [35] and [13]) as the suspension liquid.

Finally, the main goal of the work presented in this chapter is to print thin-film transistors (TFTs), however no gate-modulation has been measured to date (bottom-gate structure; see Figure 8.11). There are several explanations for this, which need to be investigated. One possibility is the composition of the films – the acetone-deposited films contain a significant percentage of carbon, while the water-deposited films contain a great deal of oxygen. Comparisons between these films, and films deposited from yet other suspensions, should shed light on this idea. Another possibility is the roughness of the film, particularly near the gate contact. Physical compression of the film has reduced large-scale roughness, but further investigation is needed to determine if it can enable gate modulation by also reducing local roughness and/or improve connectivity between the nanoparticles.

Chapter 9

PZT Nano-thick Ribbons / Energy Harvesting

In this chapter, we discuss PZT ribbons that can be transferred onto plastic, potentially leading to a more efficient material than the PVDF currently used for the “flying carpet”. We will see that the necessary voltages could theoretically be greatly reduced, which would simplify the power supply circuit design, and larger amplitudes could be possible, which should increase the propulsive forces we can achieve. Section 9.1 gives a brief overview of the process. In Section 9.2, we explain the potential actuation benefits of this material and discuss the structure used in this work. Section 9.3 describes how we characterize the material and present results. Finally, in Section 9.4, we describe future work that is needed to produce a structure capable of achieving the desired actuation improvement.

9.1 Abstract

When annealed at high temperatures, PZT forms the perovskite crystal structure and has much higher piezo-coefficients. However, these temperatures are incompatible with most flexible/stretchable substrates. Hence, this work seeks to combine the beneficial properties of these two regimes by first forming high-quality PZT ribbons (with micrometer scale widths and nanometer scale thicknesses) on MgO wafers, and then

transferring these ribbons onto a flexible substrate. This transferring is achieved by etching the MgO under the ribbons by just the right amount so that the ribbons can be pulled off of the MgO with a sheet of PDMS rubber (via van der Waals forces) [28]. For transfer to other substrates, a thin adhesive layer is used.

9.2 Introduction

9.2.1 Benefits for Actuation

This process has the potential to lead to more efficient actuation than the PVDF used in the “flying carpet”, and to operate at much lower voltages. Part of this advantage is a result of PZT’s higher piezoelectric coefficients (typically, $d_{31} \approx 100\text{-}200$ pm/V for PZT, compared with 23 pm/V for PVDF), and the other part is due to its much greater stiffness ($Y_{PZT} \sim 100$ GPa, compared with ~ 2 GPa for PVDF). To illustrate this advantage, Figure 9.1a compares the predicted curvature of the PVDF bimorph (at 100 V) used for the “flying carpet” with that of a PZT unimorph (at 1/10 the voltage, or 10 V) using a substrate with Young’s modulus equal to that of PVDF ($Y_s = 2$ GPa; the PZT parameters used are $d_{31, PZT} = 150$ pm/V and $Y_{PZT} = 100$ GPa). The inactive layer is assumed to be 30 μm thick. Observe that, for active layer thicknesses above ~ 10 μm , the PZT unimorph is expected to bend as much as the PVDF bimorph, even at one tenth of the voltage. For thinner active layers, the improvement should be even more pronounced. Of course, the thinness of the active layer is limited by the electric field that would cause breakdown (or depolarization, if a bipolar ac voltage is applied) – for PZT, this is in the 100 kV/cm to 1 MV/cm range, limiting the PZT to be thicker than ~ 1 μm when 10 V is applied. For PVDF, the limit is ~ 0.5 to 2 MV/cm, or ~ 2 μm for 100 V. For the PZT, the actual

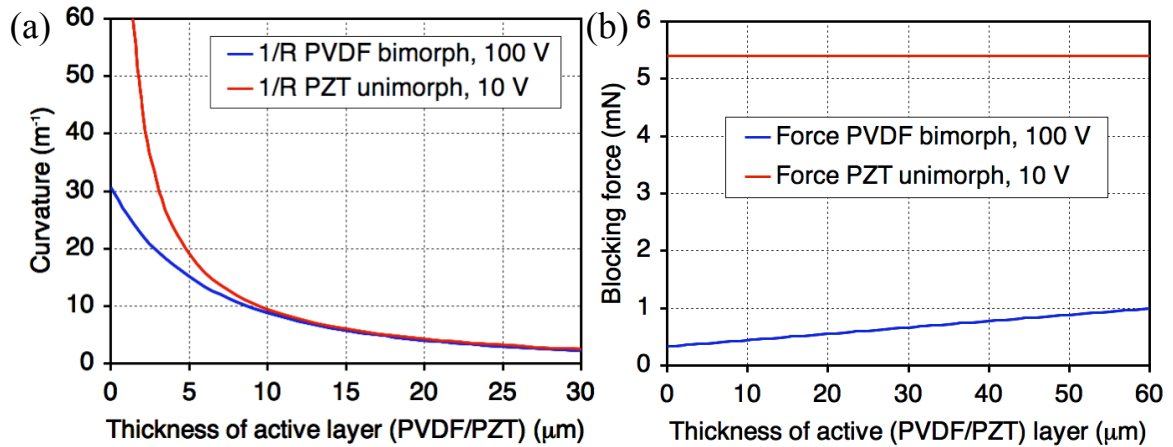


Figure 9.1 Comparison of (a) curvature, and (b) blocking force, between a PVDF bimorph at 100 V, and a PZT unimorph at 10 V.

curvature is also limited by the yield strength: $\sim 0.3\%$ strain for PZT, or $1/R < \sim 200 \text{ m}^{-1}$ (this assumes a $30 \text{ }\mu\text{m}$ inactive layer). PVDF can achieve $\sim 3\%$ strain, so that is not a limiting factor for this structure. In Figure 9.1b, we see that the predicted blocking force also sees a large improvement for the PZT unimorph.

9.2.2 This Work

The structure used in this work does not use metal contacts covering the entire surface area of the PZT, as would be needed to take full advantage of the actuation potential as described above, but rather uses an interdigitated structure (Figure 9.2) for energy harvesting applications, due in part to technical challenges in producing metal contacts covering the bottom and top surfaces of the ribbons (see Section 9.4). Such a structure can produce higher voltages when used for energy harvesting, due to the greater distance between electrodes ($\sim 10\text{-}100 \text{ }\mu\text{m}$, versus the $\sim 1 \text{ }\mu\text{m}$ PZT thickness), but correspondingly requires greater voltages for actuation. Also, while the process used to fabricate the PZT in this work would result in $d_{31} = d_{32}$, the ribbon structure could allow tuning of the $d_{31} /$

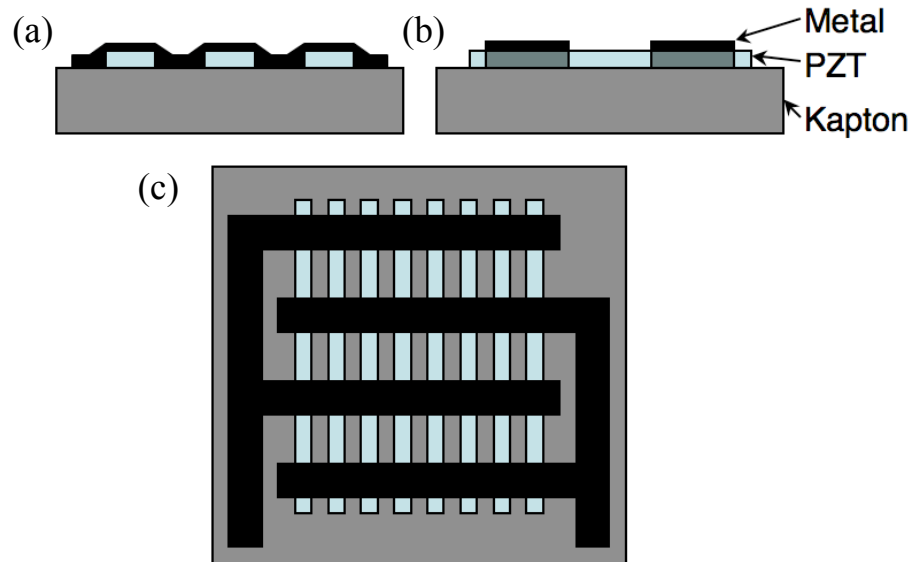


Figure 9.2 Interdigitated structure. **(a)** End view. **(b)** Side view. **(c)** Top view.

d_{32} ratio. This is because the PZT is much stiffer than the substrate it can be transferred to, so the bending parallel to the ribbons would not be affected much by increasing the gap between adjacent ribbons, while the bending perpendicular to the ribbons would drop rapidly.

9.3 Experimental Arrangement & Results

First, the large-scale ($> 1 \text{ mm}^2$) piezoelectric properties of the PZT film were characterized while it was still on the MgO substrate (and before etching the ribbons). The following setup was used to measure d_{31} , one of the piezoelectric coefficients (Figure 9.3, Reference [28]): The MgO wafer is used as the top surface of a small pressure chamber, so that when the pressure in the chamber is increased the wafer will bow outward, and the resulting strain in the PZT film will produce a charge density that is measured to determine d_{31} . A metal layer deposited between the MgO and the PZT film is used as a common back contact, while an array of $\sim 3 \text{ mm}^2$ metal squares are patterned on

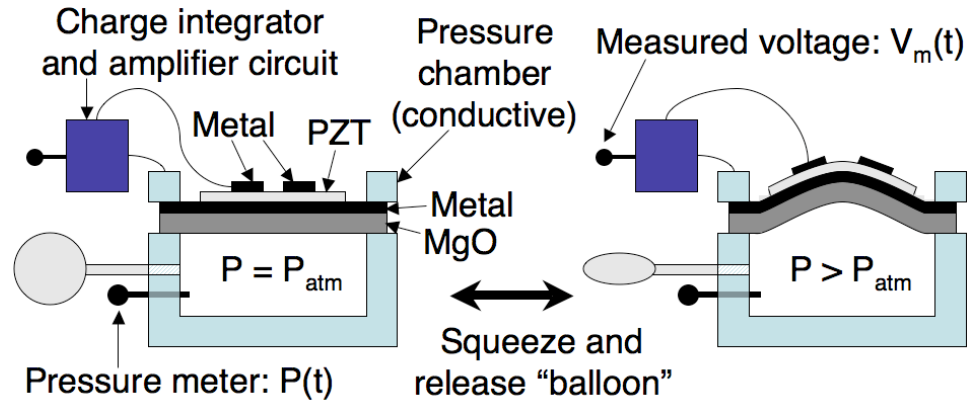


Figure 9.3 Diagram of d_{31} measurement setup: varying the pressure results in a varying charge density.

the top surface of the PZT for the other contact. Platinum was used as the back contact, as its lattice constant is similar to that of MgO, and thus high quality PZT can still be formed on it. The size of the top contacts was chosen to minimize the effect of leakage through the PZT, which became significant for larger contact areas. In addition, the thickness of the PZT was made to be $\sim 3 \mu\text{m}$ for this test structure. The cause of the leakage may be due to pinholes in the PZT film. A charge integrator and amplifier circuit was used to measure d_{31} . This is the same circuit that was used to measure the sensor signals for the “flying carpet”, and was shown in Figure 3.5. The only differences were the different capacitance of PZT versus PVDF and a different gain factor, G , was used, as follows: The measuring circuit results in a signal $V_m = V_{int} (C_{PZT}/C_1) (R_2/R_1)$. When V_m is multiplied by an appropriately chosen software gain of $G = \frac{1}{A_{sensor}} \cdot \frac{R_1 C_1}{R_2} \approx 2.5 \cdot 10^{-4} \text{ F/m}^2$

(for this measurement setup, $C_1 = 50 \text{ nF}$, $R_1 = 10 \text{ k}\Omega$, and $R_2 = 660 \text{ k}\Omega$, and the sensor area is $\sim 3 \text{ mm}^2$), the result, $\sigma_q = V_m \cdot G$, is numerically equal to the local charge density. Since this measuring circuit contains a DC filter (to remove drift from the op-amp), we measured d_{31} by repeatedly squeezing and releasing a small “balloon” to oscillate the

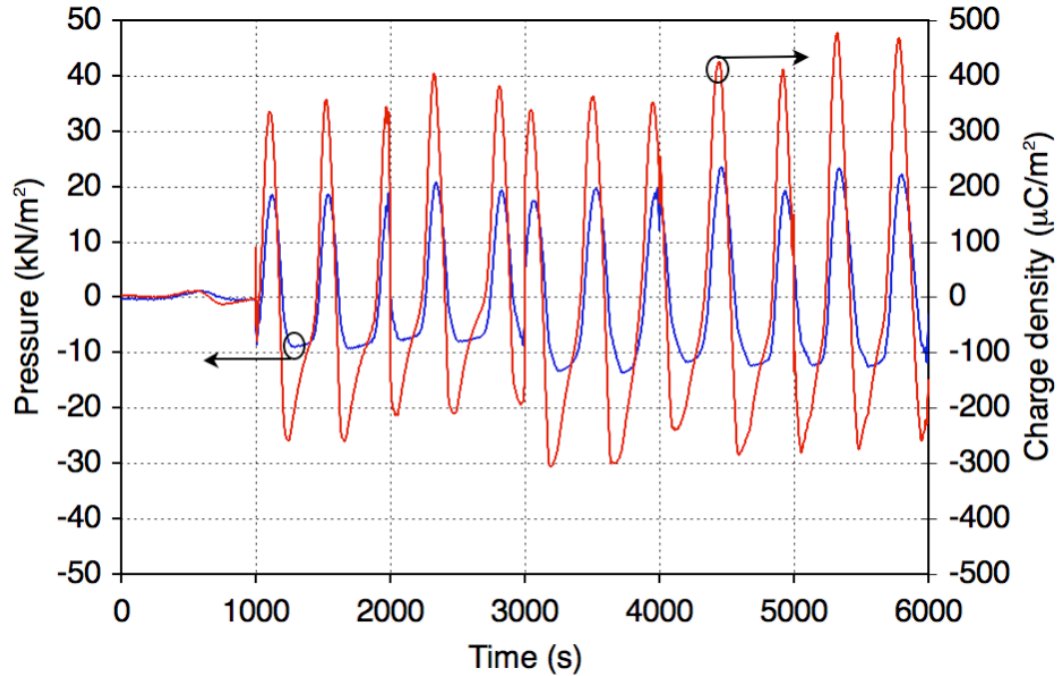


Figure 9.4 Example of d_{31} characterization, showing charge density, σ_q , resulting from a time-varying pressure, P .

pressure in the chamber (Figure 9.3). Figure 9.4 shows an example of such a measurement, plotting the pressure (as determined from a pressure sensor within the chamber) and charge density (calculated from the measuring circuit as described above) versus time. d_{31} is then extracted using the standard equations for charge density, $\sigma_q = d_{31}Y_{PZT}\epsilon$, and strain (for the setup shown in Figure 9.3, near the center of the wafer), $\epsilon \approx ((1-\nu_{MgO}^2)/(1-\nu_{PZT})) * (3Pr^2/4Y_{MgO}t^2)$, where Y is Young's modulus ($Y_{MgO} \approx 250$ GPa, $Y_{PZT} \approx 100$ GPa), ν is Poisson's ratio ($\nu_{MgO} = 0.18$, $\nu_{PZT} = 0.3$), P is the air pressure inside the chamber, $t = 0.5$ mm is the thickness of the wafer, and $r = 19$ mm is the inner radius of the pressure chamber. This results in $d_{31} \approx (\sigma_q/P) * (Y_{MgO}/Y_{PZT}) * ((1-\nu_{PZT})/(1-\nu_{MgO}^2)) * (4t^2/3r^2) \approx 0.0017 * (\sigma_q/P) \approx 34$ pm/V for the measurement shown in Figure 9.2. In addition, polling the sample with an electric field of 100 kV/cm increased d_{31} to ~ 75

pm/V after ~ 5 hours (after which not much change was observed). A plot showing this increase with poling time can be found in Reference [28].

The next step was to etch the PZT film into ribbons and transfer them to PDMS. The transferring was achieved by etching the MgO under the ribbons by just the right amount so that the ribbons could be pulled off of the MgO with a sheet of PDMS rubber, via van der Waals forces. After this process, measurements of the piezoelectric coefficients found them to be similar to the measurements before etching & transfer [28]. The initial objective of this collaboration was for energy harvesting, so an important measurement was the power generated when the material was strained. For these measurements, the PZT ribbons were transferred to Kapton (using a thin layer of adhesive, $\sim 2 \mu\text{m}$ thick), followed by deposition of the interdigitated metal lines (Figure 9.2).

9.4 Summary & Future Directions

In summary, PZT ribbons $\sim 5 \mu\text{m}$ wide and ~ 0.3 to $1 \mu\text{m}$ thick have been transferred onto plastic (over regions exceeding 1 cm^2), while retaining relatively high piezoelectric coefficients. These piezoelectric properties, combined with the expected stiffness of PZT, should enable more efficient actuation than PVDF.

As mentioned in Section 9.2.2, in order for this material to result in superior actuation compared with the PVDF bimorph, we need to apply higher electric fields than the interdigitated structure can easily allow. To address this, we would like to have a metal contact covering the entire top and bottom sides of the PZT ribbons. The advantage of such a structure is indicated in Figure 9.5, which plots the expected curvature for the two structures (for the interdigitated structure, the predicted curvatures for several metal

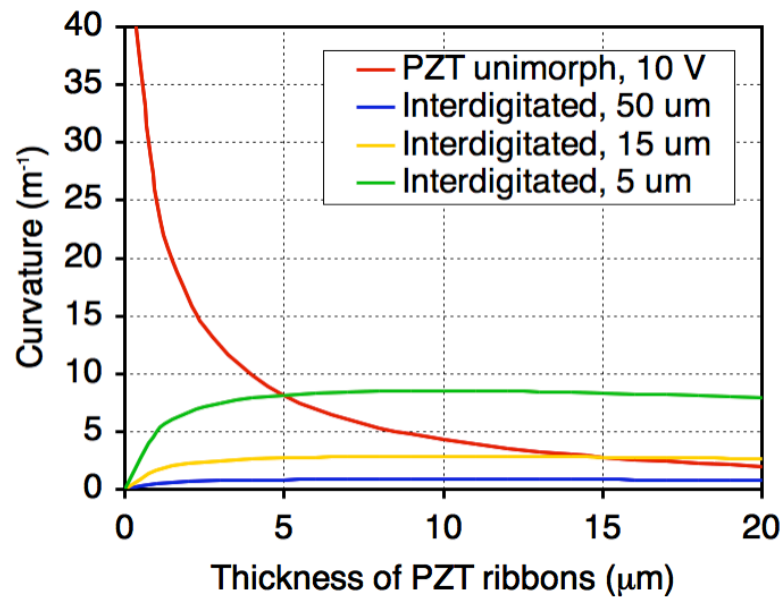


Figure 9.5 Comparison of curvature between a PZT unimorph and interdigitated structures.

line spacings are plotted). For both structures, the PZT ribbons are assumed to have d_{31} of 75 pm/V, are 3 μm thick and occupy 20% of the area they cover (to create unilateral bending, as mentioned in Section 9.2.2. For the interdigitated structures, the effect of the width of the metal lines has been ignored – this would make these structures somewhat worse, as the curvature under the metal lines would be zero. The substrate is assumed to be 30 μm thick and have a Young’s modulus of 2 GPa. As can be seen in Figure 9.5, the standard unimorph structure results in considerably greater curvatures assuming that the electrode spacing is greater than the PZT thickness. With the current process, reducing this spacing below even ~20 μm is more challenging (due to shorts) than producing PZT ribbons a few microns thick. Currently, to avoid leakage, the PZT needed to be ~3 μm thick for a 3 mm² area, but with somewhat thicker films this area could be increased. The PVDF bimorph used currently for the “flying carpet” can achieve ~2 m⁻¹ at 100 V DC

(see Figure 9.1; the PVDF is 28 μm thick), whereas a PZT unimorph structure should achieve this curvature at only 10 V even with $\sim 15 \mu\text{m}$ thick PZT.

Besides avoiding leakage in thin PZT layers, there is another challenge for producing a standard bimorph structure with the PZT ribbons – coating metal on both the top and bottom surfaces of the ribbons, and making contact to each side. If the ribbons are transferred with metal only on their top surface, transferring onto a pre-metallized substrate could form the bottom contact. However, this may not make a good contact, especially since some form of adhesive is needed. A conductive adhesive is one way to surmount this, provided it is sufficiently thin and flexible. On the other hand, assuming that the MgO can be etched under the ribbons without etching the metal layer between the MgO and the PZT, then the process shown in Figure 9.6 could be used to make contacts to the bottom and top metal layers after transfer, as follows: First, deposit metal (probably platinum, due to its lattice matching with MgO) over most of the MgO wafer, but blocking one end (Figure 9.6a). Then grow the PZT layer over the entire wafer and deposit the top metal (more freedom to choose this metal; gold is given as an example) over most of the wafer, except the end opposite to that blocked previously (Figure 9.6b). Next, pattern the ribbons by etching the top metal, PZT, and bottom metal using the same mask. If the ribbons are aligned properly, one end should now have no metal on top, while the other end will have no metal on the bottom (Figure 9.6c). Then proceed as in the standard process [28] – i.e. etching the MgO slightly under the ribbons until they can be removed with either a piece of PDMS or an adhesive-coated plastic. Once the ribbons are transferred to plastic, contact could be made, with conductive paint, to the ends of the ribbons that have metal on the top surface (Figure 9.6d). That might work for contact to

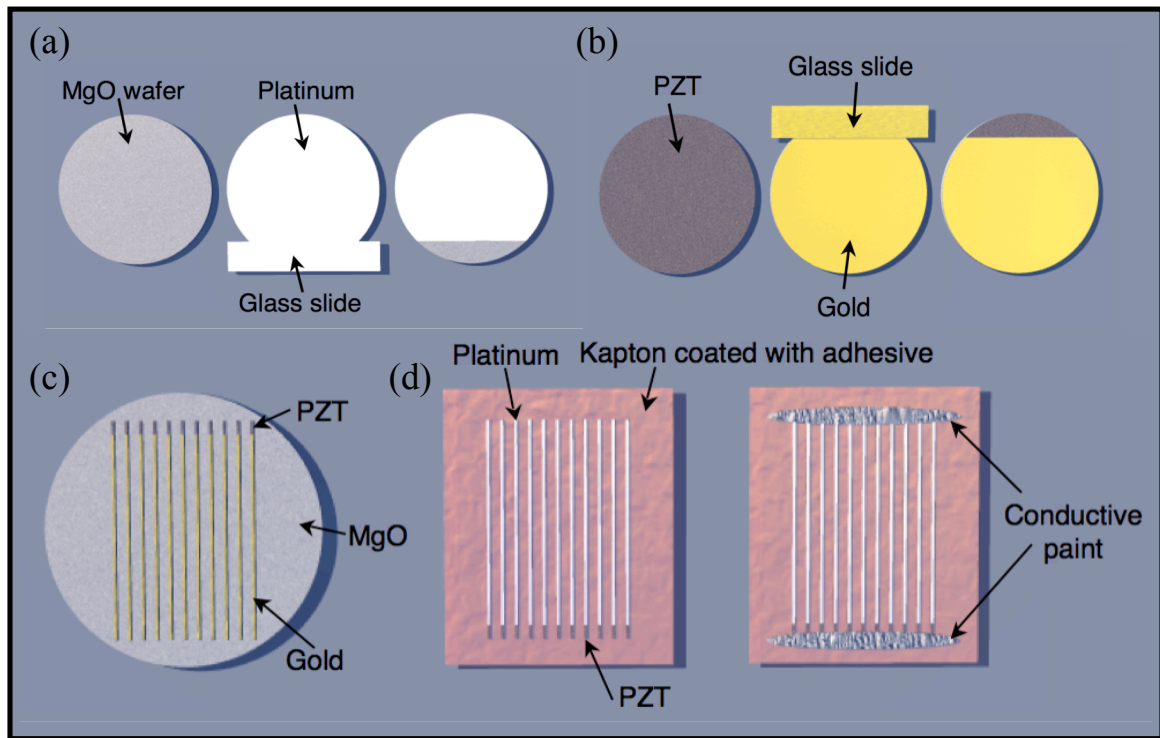


Figure 9.6 Proposed process for contacting PZT ribbons. **(a)** Place a glass slide on one end of an MgO wafer, deposit platinum, and remove slide. **(b)** After PZT growth, place a glass slide on the other end of the wafer, deposit gold, and remove slide. **(c)** Pattern the gold, PZT, and platinum, with the same mask. **(d)** After over-etching of the MgO, transfer ribbons to adhesive-coated Kapton. Separate regions of conductive paint contact the platinum and the gold.

the bottom metal as well, if the paint can penetrate under the ribbons to contact the metal there. Otherwise, a conductive adhesive could be used in that area. This is still potentially preferable to using conductive epoxy over the entire area of ribbons, as it allows greater freedom in choice of adhesive (i.e. it could be stiffer, for example). Additionally, the patterned metal may form a superior bond to the PZT compared with conductive epoxy.

Chapter 10

Summary & Future Directions for the “Flying Carpet”

In this chapter we provide a summary of our work on the “flying carpet” in Section 10.1, and discuss three possible areas for future work – lift in Section 10.2, propulsion in two dimensions in Section 10.3, and removal of the near-ground limitation for traveling-wave based propulsion in Section 10.4.

10.1 Summary

In summary, we have identified theoretical and practical considerations that are used to guide our choice of parameters for the investigation of propulsive forces produced by traveling waves in thin sheets of material and chose the materials and structure necessary to meet these criteria. We then showed how integrated sensors are used to adjust the actuator signals using linear control matrices and feedback, which resulted in near-ideal traveling wave shapes. These traveling waves have been produced with amplitudes up to $\sim 500 \mu\text{m}$, and at 100 Hz we have measured forces exceeding $100 \mu\text{N}$ (resulting in velocities over 1 cm/sec) when the sheet is suspended ~ 1 mm above the ground. The velocity is limited by the tethers that support the sheet and provide power. The aerodynamic propulsive force that we have demonstrated is theoretically sufficient to achieve “flying” of the sheet, provided that it can be freed from its tethers (see Section

5.3). The sheet can propel itself uphill (up to a few degrees), but no lift has been observed so far. Measurements with passive test samples indicate that at least partial lift can begin at $\sim 20\text{-}30$ cm/s. A free sheet needs to start moving from a position resting on the ground, so practical issues such as friction and static electricity have been addressed. This work also demonstrates the advantages, in general, of using integrated sensors to control the dynamic shape of thin plastic sheets deformed by piezoelectric elements. This could be useful for other applications, such as adaptive optics.

Preliminary work has indicated the feasibility of providing on-board power for the sheet, at least for a brief period. In addition, preliminary work was presented on room-temperature “printed” silicon, which would be useful for thin-film electronics on PVDF, due to the low temperature (~ 60 C) at which PVDF begins to lose its piezoelectric properties. Finally, more efficient materials, PZT nanoribbons that can be transferred onto flexible substrates, are being developed, which would allow the applied voltages to be considerably reduced.

10.2 Lift

The next major development needed is the demonstration of lift. As discussed theoretically in Section 5.3, and from the measurements with passive test samples in Section 7.2, we need the sheet to reach speeds of $\sim 20\text{-}30$ cm/s before we would expect to see lift. The main limitation currently is overcoming friction – various methods to address this have been discussed in Chapter 7. Another direction would be to increase the propulsive force by developing a more efficient material that could provide larger amplitude vibration, as discussed in Chapter 9. In addition, the present system bends ~ 3

times less than expected (Section 3.2), so if this could be addressed, perhaps by using a different adhesive, we would also expect to be able to achieve greater propulsive forces.

For purely demonstration purposes, having a cart that follows the sheet, as discussed in Section 7.3, should be sufficient. However, for an actual device, on-board power is needed to allow the sheet to move freely. Preliminary work on this area was discussed in Section 6.3.

10.3 2-D Propulsion

An important step needed in the development of an autonomous or remote-controlled “flying carpet” is the ability to move in two dimensions, rather than just forward and backward. This can be achieved by creating an array of actuators, say 4 by 4 at minimum, rather than the linear array of 4 by 1 currently used. If it is possible to control the orientation of bending in each actuator, it is clear that traveling waves, and thus propulsion, could then be generated in two dimensions. However, even if the bending remains unilateral, it should still be possible to produce waves in different directions. For example, if a traveling wave is produced in each 4 by 1 array, in the same direction, but shifted by a quarter wavelength from one 4 by 1 array to the one next to it, the result could be a wave traveling at a 45-degree angle (Figure 10.1). Currently, the ability to add additional actuators, as would be needed for 2-D propulsion, is limited by the number of external connections that can be managed, practically. Once on-board power is achieved, it will become more straightforward to add additional actuators. However, note that if each actuator has its own voltage signal applied to it, the weight of the necessary circuitry will increase with the number of actuators.

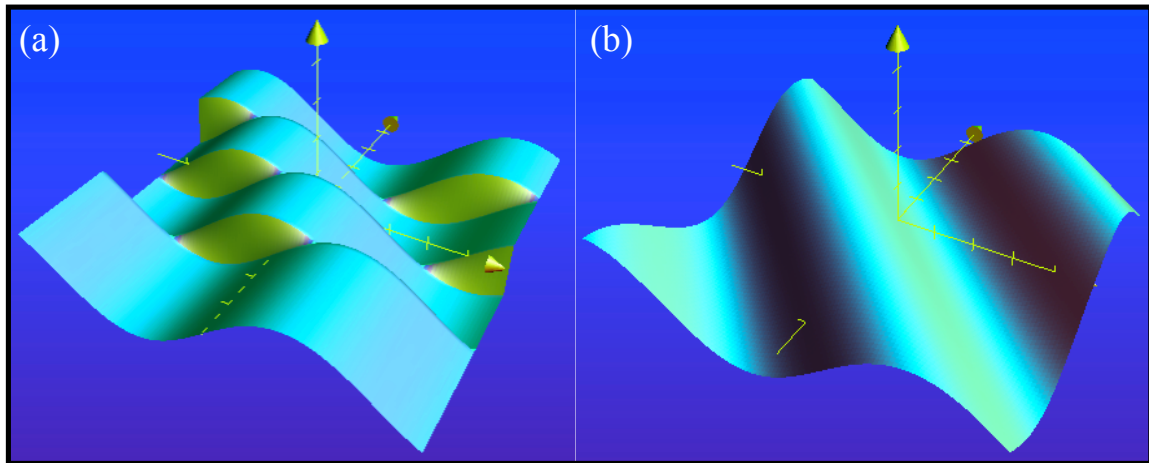


Figure 10.1 Illustration of a 45-degree wave produced from unilateral actuation. **(a)** Bending of the four strips of the sheet, each bent in a shifted sine wave, are not connected. **(b)** The idealized result for a continuous sheet (the more actuators there are, the closer this would be to reality).

10.4 Overcoming Near-Ground Limitations

As a practical device, the current rendition is limited by its need to remain very close to the ground. This is for two reasons: (1) The propulsive force increases rapidly as the gap between the sheet and the ground is decreased. (2) The lift effect is result of the aerodynamics near a boundary, which induces a slight tilt in the sheet. To address the first reason, it has been suggested (e-mail communication on September 30, 2011 from Matthew Riley) that a small gap could be created between two sheets, allowing the air to be pumped effectively between the sheets even when the sheet is not near the ground (Figure 10.2). This would require attaching the two sheets together with some kind of elastics, so they would still be free to vibrate as needed. This should result in propulsion not near the ground, but still no lift. However, it might be feasible to achieve lift by having some portion of the sheet bent upwards to provide an angle of attack, like an airplane wing. Alternatively, one of the sheets could be an inactive, rigid, sheet, which

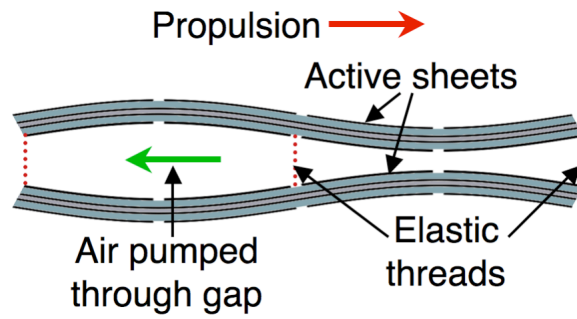


Figure 10.2 Schematic of proposed propulsion mechanism away from the ground.

could be shaped like a wing to induce lift. This could also allow placement of the necessary electronic on this inactive sheet, rather than directly on the PVDF one.

Appendix A

Publications and Presentations Resulting From This Thesis

A.1 Peer-reviewed Publications

- **“Fundamental and Experimental Conditions for the Realization of Traveling-Wave Induced Aerodynamic Propulsive Forces by Piezoelectrically-Deformed Plastic Substrates”**. Noah T. Jafferis and James C. Sturm. Submitted – under consideration.
- **“Formation and Post-Deposition Compression of Smooth and Processable Silicon Thin Films from Nanoparticle Suspensions”**. Noah T. Jafferis and James C. Sturm. *Journal of Applied Physics* 111, 064316 (2012).
- **“Traveling Wave-Induced Aerodynamic Propulsive Forces using Piezoelectrically Deformed Substrates”**. Noah T. Jafferis, Howard A. Stone, and James C. Sturm. *Applied Physics Letters* 99, 114102 (2011).
- **“Piezoelectric Ribbons Printed onto Rubber for Flexible Energy Conversion”**. Yi Qi, Noah T. Jafferis, Kenneth Lyons, Jr., Christine M. Lee, Habib Ahmad, and Michael C. McAlpine. *Nano Letters* 10, 524-528 (2010).

A.2 Conference Presentations

- “Power Analysis and Fundamental and Experimental Conditions for Piezoelectrically-Deformed Plastic Substrates for “Flying Carpet” Propulsion” – Poster. **Materials Research Society (MRS) Spring Meeting**, April 2012. San Francisco, CA, USA.

- “Traveling Wave Induced Aerodynamic Propulsive Force using Active Control of the Dynamic Shape of Piezoelectrically Deformed Plastic Substrates” – Poster. **European Congress and Exhibition on Advanced Materials and Processes (EUROMAT)**, September 2011. Montpellier, France.
- “Traveling Wave-Induced Aerodynamic Propulsive Force using Active Control of the Dynamic Shape of Piezoelectrically-Deformed Plastic Substrates” – Talk. **International Symposium on Integrated Ferroelectrics (ISIF)**, August 2011. Cambridge University, England.
- “Traveling Wave-Induced Aerodynamic Propulsive Force using Active Control of the Dynamic Shape of Piezoelectrically-Deformed Plastic Substrates” – Talk. **Materials Research Society (MRS) Fall Meeting**, December 2010. Boston, MA, USA.
- “Active Control of the Dynamic Shape of Deformable Plastic Substrates” – Poster. **Flexible Electronics & Displays Conference (FlexTech)**, February 2010. Phoenix, AZ, USA.
- “Printing Silicon from Nanoparticle Suspensions” – Talk. **Electronic Materials Conference (EMC)**, June 2009. Penn State, University Park, PA, USA.
- “Printing Silicon from Nanoparticle Suspensions” – Poster. **Flexible Electronics & Displays Conference (FlexTech)**, February 2009. Phoenix, AZ, USA.

Bibliography

- [1] O. Akcikir, J. Therrien, G. Belomoin, N. Barry, J. D. Muller, E. Gratton, and M. Nayfeh, "Detection of luminescent single ultrasmall silicon nanoparticles using fluctuation correlation spectroscopy," *Appl. Phys. Lett.*, vol. 76 (14), pp. 1857-1859, 2000.
- [2] H. Antoniadis, F. Jiang, W. Shan, and Y. Liu, "All screen printed mass produced Silicon Ink selective emitter solar cells," *35th IEEE Photovoltaics Specialists Conference (PVSC)*, pp. 001193 – 001196, 2010.
- [3] M. Argentina, J. Skotheim, L. Mahadevan, "Settling and swimming of flexible fluid lubricated foils," *Phys. Rev. Lett.*, vol. 99, p. 224503, 2007.
- [4] B. Behkam and M. Sitti, "Bacterial flagella-based propulsion and on/off motion control of microscale objects," *Appl. Phys. Lett.*, vol. 90 (2), p. 023902, 2007.
- [5] G. Belomoin, J. Therrien, A. Smith, S. Rao, R. Twesten, S. Chaieb, M. H. Nayfeh, L. Wagner, and L. Mitas, "Observation of a magic discrete family of ultrabright Si nanoparticles," *Appl. Phys. Lett.*, vol. 80 (5), pp. 841-843, 2002.
- [6] L. T. Canham, in *Properties of porous silicon*, L. T. Canham, Editor, ch. 9.1, The Institution of Electrical Engineers, 1997.
- [7] F. Casadei, M. Ruzzene, L. Dozio, and K. A. Cunefare, "Broadband vibration control through periodic arrays of resonant shunts: experimental investigation on plates," *Smart Mater. Struct.*, vol. 19, p. 015002, 2010.
- [8] N. R. Coleman, "Micro-scale flapping wings for the advancement of flying MEMS," Master thesis Air Force Inst. of Tech., ADA497687, 2009.
- [9] F. dell'Isola, M. Porfiri, and S. Vidoli, "Piezo-ElectroMechanical (PEM) structures: passive vibration control using distributed piezoelectric transducers," *C. R. Mecanique*, vol. 331, pp. 69-76, 2003.
- [10] R. Dreyfus, J. Baudry, M. L. Roper, M. Fermigier, H. A. Stone, and J. Bibette, "Microscopic artificial swimmers," *Nature*, vol. 437, pp. 862-865, 2005.

- [11] J. D. Ervin and D. Brei, "Recurve piezoelectric-strain-amplifying actuator architecture," *IEEE/ASME Transactions on Mechatronics*, vol. 3 (4), pp. 293-301, 1998.
- [12] A. W. Feinberg, A. Feigel, S. S. Shevkoplyas, S. Sheehy, G. M. Whitesides, and K. K. Parker, "Muscular thin films for building actuators and powering devices," *Science*, vol. 317, pp. 1366-1370, 2007.
- [13] S. Han, X. Dai, P. Loy, J. Lovaasen, J. Huether, J. M. Hoey, A. Wagner, J. Sandstrom, D. Bunzow, O. F. Swenson, I. S. Akhatov, and D. L. Schulz, "Printed silicon as diode and FET materials – Preliminary results," *Journal of Non-Crystalline Solids*, vol. 354 (19-25), pp. 2623-2626, 2008.
- [14] M. Härting, J. Zhang, D. R. Gamota, and D. T. Britton, "Fully printed silicon field effect transistors", *Appl. Phys. Lett.*, vol. 94 (19), p. 193509, 2009.
- [15] G. L. Huang and C. T. Sun, "The dynamic behavior of a piezoelectric actuator bonded to an anisotropic elastic medium," *International Journal of Solids and Structures*, vol. 43 (5), pp. 1291-1307, 2006.
- [16] N. T. Jafferis, H. A. Stone, and J. C. Sturm, "Traveling wave-induced aerodynamic propulsive forces using piezoelectrically-deformed substrates," *Appl. Phys. Lett.*, vol. 99, p. 114102, 2011.
- [17] N. T. Jafferis and J. C. Sturm, "Formation and post-deposition compression of smooth and processable silicon thin films from nanoparticle suspensions," *J. Appl. Phys.*, vol. 111, p. 064316, 2012.
- [18] B. Kim, M. G. Lee, Y. P. Lee, Y. Kim, and G. Lee, "An earthworm-like micro robot using shape memory alloy actuator", *Sensors and Actuators A*, vol. 125, pp. 429-437, 2006.
- [19] D.-H. Kim, J. Viventi, J. J. Amsden, J. Xiao, L. Vigeland, Y.-S. Kim, J. A. Blanco, B. Panilaitis, E. S. Frechette, D. Contreras, D. L. Kaplan, F. G. Omenetto, Y. Huang, K.-C. Hwang, M. R. Zakin, B. Litt, and J. A. Rogers, "Dissolvable films of silk fibroin for ultrathin, conformal bio-integrated electronics," *Nat. Mater.*, vol. 9 (6), pp. 511-517, 2010.

- [20] G. Ledoux, O. Guillois, D. Porterat, C. Reynaud, F. Huisken, B. Kohn, and V. Paillard, "Photoluminescence properties of silicon nanocrystals as a function of their size," *Phys. Rev. B*, vol. 62 (23), pp. 15942-15951, 2000.
- [21] S. Martel, J.-B. Mathieu, O. Felfoul, A. Chanu, É. Aboussouan, S. Tamaz, P. Pouponneau, G. Beaudoin, G. Soulez, L. H. Yahia, and M. Mankiewicz, "Automatic navigation of an untethered device in the artery of a living animal using a conventional clinical magnetic resonance imaging system," *Appl. Phys. Lett.*, vol. 90 (11), pp. 114105–114107, 2007.
- [22] S. Martel, "Collective methods of propulsion and steering for untethered microscale nanorobots navigating in the human vascular network," *Proc. IMechE, Part C: J. Mechanical Engineering Science*, Vol. 224, pp. 1505-1513, 2010.
- [23] N. Miki and I. Shimoyama, "Analysis of the flight performance of small magnetic rotating wings for use in microrobots," *IEEE International Conference on Robotics & Automation*, pp. 3065-3070, 1998.
- [24] L. Mitas, J. Therrien, R. Twesten, G. Belomoin, and M. H. Nayfeh, "Effect of surface reconstruction on the structural prototypes of ultrasmall ultrabright Si₂₉ nanoparticles," *Appl. Phys. Lett.*, vol. 78 (13), pp. 1918-1920, 2001.
- [25] C. D. Onal, R. J. Wood, and D. Rus, "Towards printable robotics: origami-inspired planar fabrication of three-dimensional mechanisms," *IEEE International Conference on Robotics and Automation*, pp. 4608-4613, 2011.
- [26] S. K. Park, C.-C. Kuo, J. E. Anthony, and T. N. Jackson, "High mobility solution-processed OTFTs," *IEEE Elec. Dev. Meeting*, 2005.
- [27] R. Pelrine, R. Kornbluh, Q. Pei, and J. Joseph, "High-speed electrically actuated elastomers with strain greater than 100%," *Science*, vol. 287, pp. 836-839, 2000.
- [28] Y. Qi, N. T. Jafferis, K. Lyons, Jr., C. M. Lee, H. Ahmad, and M. C. McAlpine, "Piezoelectric ribbons printed onto rubber for flexible energy conversion," *Nano Letters*, vol. 10 (2), pp. 524-528, 2010.
- [29] W. Qin and P. Fraundorf, "Lattice parameters from direct-space images at two tilts," *Ultramicroscopy*, vol. 94 (3-4), pp. 245-262, 2003.

- [30] A. J. Reynolds, "The swimming of minute organisms," *J. Fluid Mech.*, vol. 23 (2), pp. 241-360, 1965.
- [31] K. Ryu, J. Zueger, S. K. Chung, and S. K. Cho, "Underwater propulsion using AC-electrowetting-actuated oscillating bubbles for swimming robots," *IEEE 23rd International Conference on Micro Electro Mechanical Systems (MEMS)*, pp. 160-163, 2010.
- [32] N. Saga and T. Nakamura, "Development of a peristaltic crawling robot using magnetic fluid on the basis of the locomotion mechanism of the earthworm," *Smart Mater. Struct.*, vol. 13, pp. 566-569, 2004.
- [33] K. P. Selverov and H. A. Stone, "Peristaltically driven channel flows with applications toward micromixing," *Phys. Fluids*, vol. 13 (7), pp. 1837-1859, 2001.
- [34] J. Y. W. Seto, "The electrical properties of polycrystalline silicon films," *J. Appl. Phys.*, vol. 46 (12), pp. 5247-5254, 1975.
- [35] T. Shimoda, Y. Matsuki, M. Furusawa, T. Aoki, I. Yudasaka, H. Tanaka, H. Iwasawa, D. Wang, M. Miyasaka, and Y. Takeuchi, "Solution-processed silicon films and transistors," *Nature*, vol. 440, pp. 783-786, 2006.
- [36] H. Sirringhaus, N. Tessler, and R. H. Friend, "Integrated optoelectronic devices based on conjugated polymers," *Science*, vol. 280 (5370), pp. 1741-1744, 1998.
- [37] T. Someya, Y. Kato, T. Sekitani, S. Iba, Y. Noguchi, Y., Murase, H. Kawaguchi, and T. Sakurai, "Conformable, flexible, large-area networks of pressure and thermal sensors with organic transistor active matrixes," *Proc. Natl. Acad. Sci.*, vol. 102 (35), pp. 12321-12325, 2005.
- [38] G. Taylor, "Analysis of the swimming of microscopic organisms," *Proc. R. Soc. London A*, vol. 209, pp. 447-461, 1951.
- [39] G. Taylor, "Film notes for low-Reynolds-number flows," *National Committee for Fluid Mechanics Films*, No. 21617, 1967.
- [40] S. Tuncdemir, S. O. Ural, and K. Uchino, "Meso-scale piezoelectric gripper with high dexterity," *Japanese Journal of Applied Physics*, vol. 48, p. 044501, 2009.

- [41] Q.-M. Wang, X.-H. Du, B. Xu, and L. E. Cross, "Electromechanical coupling and output efficiency of piezoelectric bending actuators," *IEEE Transactions on Ultrasonics, Ferroelectrics, and Frequency Control*, vol. 46, pp. 638-646, 1999.
- [42] R. J. Wood, "The first takeoff of a biologically inspired at-scale robotic insect," *IEEE Transaction on Robotics*, vol. 24 (2), pp. 341-347, 2008.
- [43] R. J. Wood, B. Finio, M. Karpelson, N. O. Pérez-Arancibia, P. Sreetharan, and J. P. Whitney, "Challenges for micro-scale flapping-wing micro air vehicles," *Proc. SPIE*, vol. 8373, pp. 83731J1-9, 2012.
- [44] Z. Yamani, W. H. Thompson, L. AbuHassan, and M. H. Nayfeh, "Ideal anodization of silicon," *Appl. Phys. Lett.*, vol. 70 (25), pp. 3404-3406, 1997.
- [45] Yaopeng Zhou and Thomas Bifano, "Adaptive optics using a MEMS deformable mirror," *Proc. SPIE*, vol. 6018, p. 601817, 2005.